Experimental and Finite Element Study of the Hydroforming Bi-layered Tubular Component

By

Md. Din Islam, B.Eng.

This thesis is submitted to Dublin City University as the fulfilment of the requirement for the award of the degree of

Master of Engineering

Supervisors: Dr. A. G. Olabi, Ph.D.
Prof. M.S.J. Hashmi, Ph.D. D.Sc.

School of Mechanical and Manufacturing Engineering
Dublin City University

August 2005

Declaration

I hereby declare that all work produced in this document is entirely my own work, except where stated, and has not been submitted in whole or in part to any other university.

Signed: _____ Date: 19.09.05

Md. Din Islam

I.D 52175090

Acknowledgements

I would like to express my sincere gratitude to Dr. A. G. Olabi and Professor M. S. J. Hashmi for their guidance, help, time and support throughout the year on helping me to complete this project. I would also like to thank senior technician Mr. Liam Domican for his co-operation carrying out the experiments in the bulge forming machine for this project.

Experimental and Finite Element Study of the Hydroforming Bi-Layered Tubular Components

Md. Din Islam B.Eng.

ABSTRACT

The application of finite element method (FEM) in the area of metal forming and material processing has been increasing rapidly during the recent years. The present study has been carried out on one of the unconventional metal forming processes called hydroforming of a multi-layered tube. The study involved both experimental and simulation work using FEA. Multi- layered tubes have extensive advantages in both domestic and industrial uses. The specimen tube consists of two different layers of materials. The outer tube material is brass and the inner tube material is copper. This project is mainly dedicated to the modelling, simulation and advanced study of one of the unconventional metal forming processes called hydroforming in which extremely high fluid pressure is used to deform the metal into desired shape. Various types of complex industrial products can be made by hydroforming. This process is suitable to produce seamless, lightweight, near net shaped industrial components. There are some complex products, which are easier to produce by hydroforming than by conventional technique.

In this research work the main forming load is hydrostatic pressure applied to the internal surface of the tube, together with an in-plane compressive load applied simultaneously. The blank is placed in a pre-shaped die block and due to the action of simultaneous internal pressure and axial load; it is formed into a complex desired shape. If the internal pressure is too high during the process without sufficient axial load it may cause the tube to burst, on the other hand too large axial load without applying sufficient internal pressure may cause wrinkling of the tube. For these reasons, a number of simulations of the hydroforming process have been carried out for different axial load and internal pressure combinations and optimum conditions have been established for the particular process. This simulated hydroforming of composite material tube and the formed product has been analysed on the basis of forming conditions and the simulated forming conditions have been verified by experiment. The simulations of hydroforming process for X or T branch have been carried by using the commercial finite element package ANSYS.

Contents

Chapter 4 Analytical Modeling and Experimental Procedure

Nomenclature

Symbol	Definition	Dimension
c	Sonic wave propagation velocity	m/s
f	Force	N
l	Element characteristic length	m
t	Time	seconds
v	Element volume	m^3
x	Velocity of specific node	m/s
B	Strain displacement matrix	
C	Global damping matrix	
D	Stress strain matrix	
E	Young modulus	N/m^2
F	Concentrated force	N
H	Displacement interpolation shape matrix	
I	Identity matrix	
K	Global stiffness matrix	
M	Global mass matrix	
R	Load vector matrix	
T	Period	
U	Virtual displacement	m
$\bar{U}$	Displacement in global X direction	m
$\dot{U}$	Nodal point velocity	m/s
$\ddot{U}$	Nodal point accelerations	m/s^2
$\bar{V}$	Displacement in global Y direction	m
$\bar{W}$	Displacement in global Z direction	m

Greek

δ	Stress	N/m^2
υ	Strain	
ρ	Density	Kg/m^3

Subscripts

S	Surface	
V	Volume	m^3

List of Figures

List of Tables

CHAPTER ONE

Introduction

1.1 Objective

The main purpose of this chapter is to review the forming and hydroforming process briefly. Firstly the process of the multi layer forming will be analysed using the finite element analysis process. To undergo this analysis the ANSYS 8.1 computer program will be used. The multi layer material will be analysed in ANSYS for a variety of different conditions. These conditions will include the wall thickness of the materials, different materials and different loading conditions. The results from this analysis were then brought to the workshop were they will be programmed into the hydro bulge forming machine and tested as to whether the two sets of results correspond. Through this analysis work it would be hoped that the multi layer material will deform correctly under the pressures applied to it during simulation and the hydro bulge forming process. It would be hoped that the multi layer material might turn out to be stronger than and not as vulnerable to the loading pressures as a single layer material might be. This could lead to the use of multi layer materials in industrial applications such as fluid transport and plumbing applications where single layer materials are being used today.

1.2 Forming Process

The metal may be converted into a desired useful shape by a forming process; it may be either by a plastic deformation process or metal removal process. Hundreds of processes have been developed for specific metal working application in order to get the desired useful shape. Plastic deformation processes which are designed to reduce an ingot or billet to a standard product of simple shape such as sheet, plate, bar, rod etc are called primary mechanical forming processes. Forming process as that produce parts to final finished shape which could be called secondary mechanical working process, such as sheet metal forming, wire drawing, tube drawing. The deformation zone is concerned

with the distribution of stress, strain, particle velocity, and overall pressure required to perform the operation.

1.3 Hydroforming process

Hydroforming is one of the unconventional metal forming processes which is a widely used industrial process in order to form complex shapes. Compared to other traditional manufacturing methods (such as stamping), hydroforming offers better part quality (tighter tolerances, increased rigidity) with lower manufacturing costs resulting from a reduced number of forming and assembly operations . Moreover, with the advent of new technological capabilities, particularly more complex and improved control systems, hydroforming has become a flexible, reliable, and hence an attractive technology. Today bulge forming is widely used in making tubular parts of different configurations used in automotive and aircraft industries, household appliances, and other applications. Typical parts that are produced in industries using the bulge forming process include T-branches, cross branches, stepped hollow shafts, rear axle casing of cars, bicycle wheel hubs, metal bellows, nozzles etc. Figure 1.1 shows a typical schematic diagram of hydroforming process

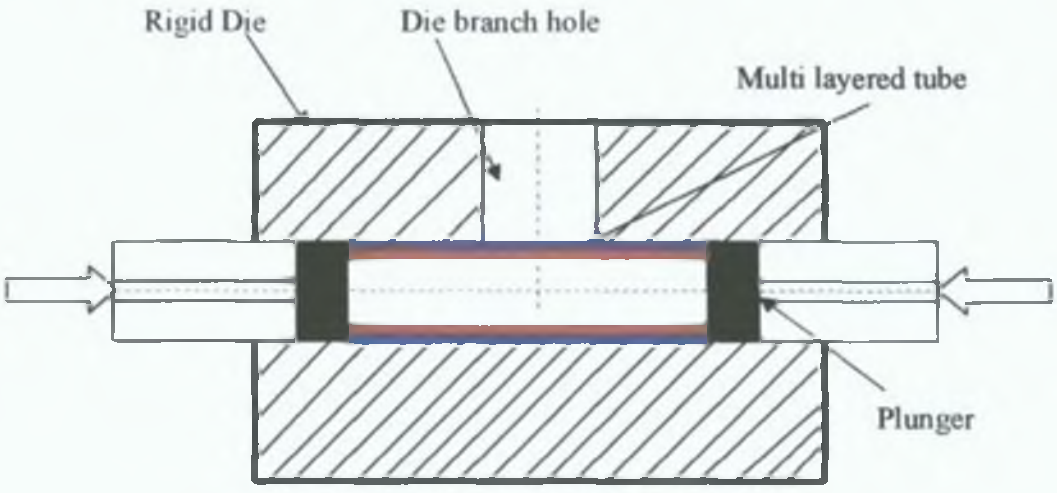

Figure 1.1: Typical Hydroforming process

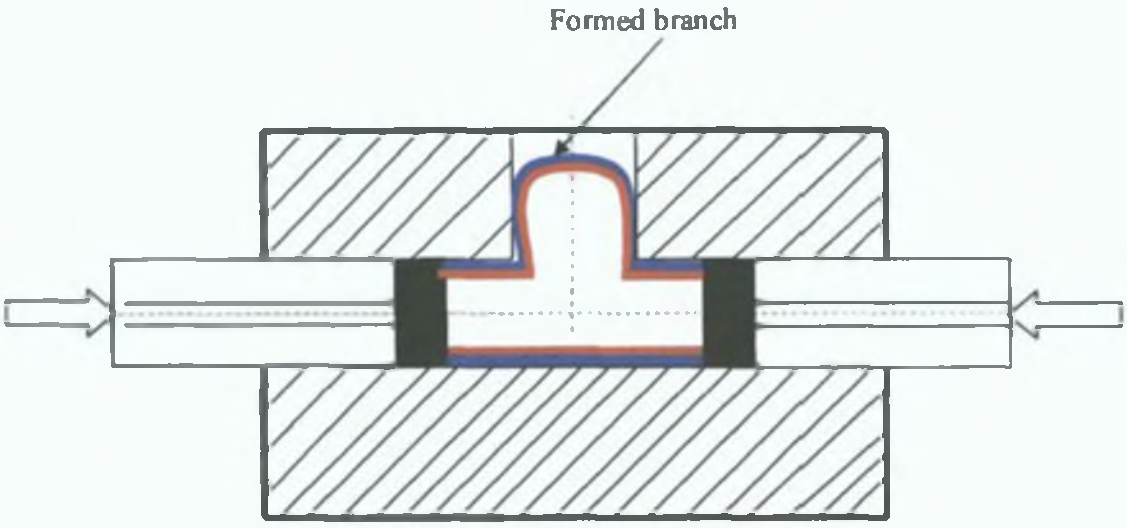

Figure 1.2: Typical T-branch Hydroforming process

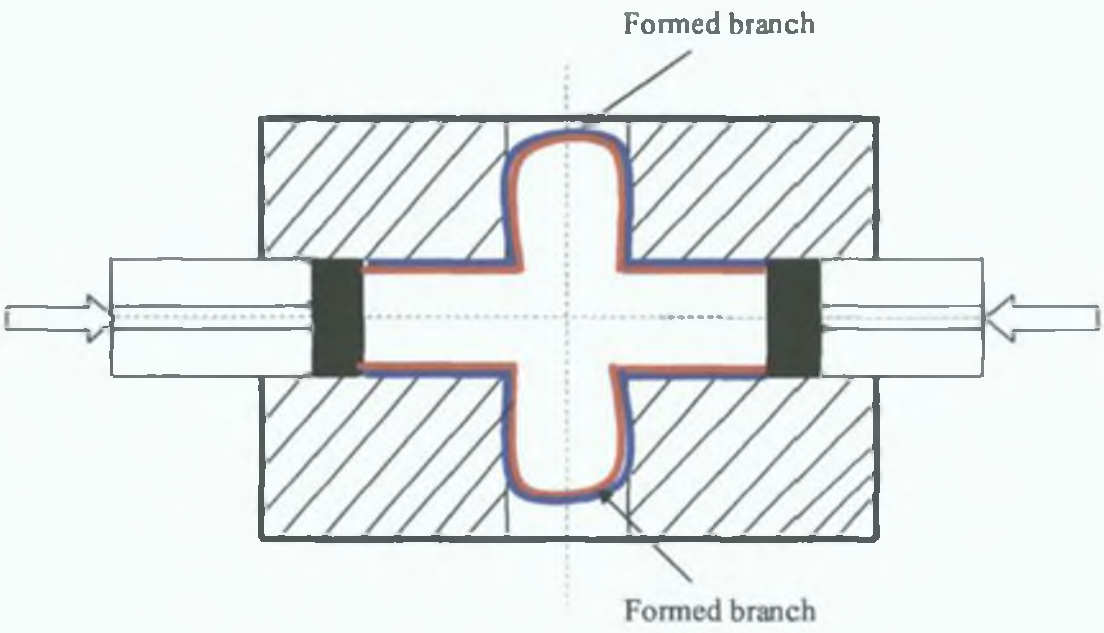

Figure 1.3: Typical X-branch Hydroforming

Figure 1.2 is describing hydroforming of T branch component where as figure 1.3 shows an X branch hydroforming process.

In the hydroforming process the material is biaxially stretched by applying the internal pressure with the help of a hydraulic medium. In advanced hydroforming processes, axial load has been added with the internal pressure to improve formability of the process. There are different arrangements of die-fixture according to the shape of final forming product. In this process one T-section and an X-section of a tubular components have been presented in the above figures at the describe hydroforming process. During the forming action the tube a blank is placed between two die halves and tube ends are held by two plungers. The axial load is applied by the plungers as a punch. There are holes through both plungers and hydraulic fluid is pumped through these holes in order to build up the internal pressure inside the tube blank. The plungers are pushed inward to provide the compressive axial load. Both internal pressure and axial compressive loads are applied simultaneously which results a good forming deformation.

In the hydroforming process there are some modes of forming process defects may appear, if the axial feed is too high in comparison with internal pressure then there is chance of formation of wrinkle and buckling of the tubes. On the other hand if the internal pressure is too high compared to end axial load there would be excess thinning of the tube and resulting in bursting of the tube. Thus bursting, wrinkle and buckling are the main failure criteria for any tube hydroforming process. In order to apply the process successfully an optimum loading condition should be establish to avoid all the instabilities and failure criteria which will enable proper deformation of the product. The hydroforming process is a highly complicated processes to analyse, the theoretical analysis methods for plastic deformation of hydroforming have been limited understanding of the process. Numerical analysis and simulation have the potential to provide a much deeper understanding of the process and hence allow for better design of process equipment and end products.

Multi-layer [50] composite technology is safer for sanitary and drinking water installations. The multi-layer structure offers essential advantages for radiator connections. The compensation of spring back forces makes the installation easy. An economical system which can be installed safely and quickly without soldering, welding or use of adhesives. Absolute oxygen diffusion tightness and corrosion resistance ensure long term function. For radiator connections the heat expansion tendency of a pipe is very important. Particularly for this application where enormous stress occurs during continuous operation, the insignificant heat expansion has positive effects. Regarding industrial applications multi-layer tube is gas tight, flexible and durable making it ideal for compressed air supply lines. It is also resistant against aggressive water and many chemical substances and therefore, suitable for air conditioning and refrigeration systems. Other areas of application include food industry, supply lines, ship building, and aerospace industries. The possibilities are endless.

1.4 Finite Element Methods and Metal forming process

The use of computer aided analysis and design of metal forming has increased considerably in recent years. FEM came of age in the early 1960's with the replacement of analogue with digital computers and the development of first commercial finite element analysis code. At this early stage, the application was confined to the contained elastic –plastic deformation where the plastic strain is of the order of 0.1%. The extension to the large strain regime was achieved in the late 1970's when limited nonlinear solvers were developed and made available. With the continuous development of computers, at present world class implicit and explicit finite element codes and package are available which can be used in the most complicated engineering problems and metal forming process. Analysis of the hydroforming process using finite element codes and some empirical metal forming and plasticity theories have resulted in better understanding of the physical process. Finite element simulation of most of the metal forming process are quite complicated as the process are highly non-linear in nature due to their physical,

geometrical, and friction which effects the process. Explicit finite element codes have much better capabilities to handle such kind of nonlinear behaviour exhibited by the metal forming process. Thus, simulation with explicit finite element analysis codes provides abetter understanding of the process and plastic deformation mechanism over implicit finite element analysis.

1.5 Summary of this chapter

This chapter introduces the hydroforming of multi layered materials. Application of hydroforming has been described briefly. Application of Finite element analysis in case of forming and hydroforming was also introduced.

CHAPTER TWO

Literature Review

2.1 Introduction

The purpose of this chapter is to survey the previous work, similar or related to the topic done by various researchers on tube hydroforming process. There are many experimental, theoretical and simulation studies carried out by different researchers on different aspect of hydroforming process. However very few works have been done by double layered hydroforming process.

2.2 Previous studies

Research on forming and tube hydroforming process has been carrying out in history of metal forming for many years. In early 1939 Grey et al [1] established a tube hydroforming process in order to manufacture seamless metal T and X branches. The setup used allowed control of the internal hydraulic pressure and tube end axial load to avoid rupture of the blank. The process involves placing a tubular blank in between two die halves, which were then clamped together. A compressive load was then applied to provide an axial feed to the tube ends via plunger, which entered through the two die holes. The internal hydroforming was applied via liquid through a drilled hole in one of the plungers. This combination of axial feed and internal pressure pushed the tube wall into the die recess thus forming the component.

M. Koc et al. [2] applied the two dimensional (2D) FEA for the tube hydroforming process. They pointed out that the feasibility of forming a specific part can be predicted by analysing thinning, thickening, strain, and stress distribution on a deform tube.

Mac Donald and Hashmi [3] applied 3-D finite element simulation of bulge forming using a solid bulging medium. In their research the components are formed by restraining the blank in a die halves the desired shape and applying an internal hydro

static pressure to the tube via a liquid and solid medium, a compressive axial load was applied to the ends of the tube in conjunction with the pressure load, then the material has been pushed into the deformation zone, thus preventing excessive thinning of the walls. FE-code LS-DYNA3D was used to simulate this process. Ahmed et al. [4] have analysed three-dimensional finite-element simulation of bulge forming. In their work the tube blank was placed between two dies halves and the tube ends are held by two plungers the tips of which act as a punch. The hydraulic fluid is pumped through the holes in the plunger in order to apply pressure inside the tube. The plungers are pushed inwards to provide the axial compressive load. Due to the pressure and the axial load the branch starts forming. Simultaneous application of these loads helps to obtain large deformation in the process.

Hwang et al [5] carried out finite element analysis of tube hydroforming processes in a rectangular die. The thickness distributions of the formed products, clamping forces, and forming pressure were simulated. A comparison with hydraulic expansion and crushing process had been made. The thickness distributions of the formed products obtained by the crushing processes are uniform compared to the hydraulic expansions test. Zhang et al [6] carried out theoretical analysis and experimental research into the integral hydro-bulge forming of oblate shell". The self-adjusting theory of plastic deformation of polyhedral shells was introduced; the feature of the stress distribution and plastic deformation of the oblate shells was discussed.

Zhng et al [7] presented a numerical simulation of the integral hydro-bulge forming of non-clearance double-layer spherical vessel. The paper shows that during hydro-bulge forming the inner shell is firstly deformed, then the outer shell begins deformation under the contact pressure from inner shell, the two layer shells contact gradually each other, at the end of the process the two layers are completely in contact and are deformed into spherical shapes. The final diameter and its variations, the development of contact situation and the thickness distribution were fully analysed.

Enikeev et al. [8] explained an analysis of the super plastic forming of a thin circular diaphragm. They developed a new engineering model for the super plastic forming of domes, which allows predicting the thickness distribution of the domes. In spite of the simplicity of the model suggested, the theoretical predictions, experimental data and published data were in good agreement. Zhang and et-al. [9] established finite-element analysis of the integral hydro-bulge forming of double-layer gap spherical vessels. Their experimental results showed that the pressurization to only the internal shell can lead to the full deformation of the internal shell and the partial deformation of the external shell. Application of pressure to the interspaces is needed to ensure that the external shell reaches its final forming pressure, so a full deformation of the double layer gap spherical vessel is obtained. Ahmed and Hashmi [10] applied finite-element to analyse the bulge forming by applying pressure and in-plane compressive load. They studied the effect of combined pressure and in-plane compressive load on the sheet-plate by the finite-element method. The contact condition between the die and the sheet-plate is also taken into consideration in the analysis. Further, the analysis is undertaken also for the pressure-only loading case and the results are compared. The analysis shows that the bulge height obtained in the combined loading situation is much higher than that in the pressure-only loading situation.

Kreis et al. [11] worked on manufacturing system for the integrated hydroforming trimming and welding of sheet metal pairs. In their system the manufacturing process of complex hollow bodies made of sheet metal is to shorten the process path. They developed a special tool for hydroforming process that integrates the trimming device.
Lee and et-al. [12] studied micro structural evolution during super plastic bulge forming of Ti-6Al-4V alloy. In their research they found that the grain growth rate of biaxially bulge formed samples was quite different from that of uniaxially deformed specimens and that the grain growth rate was independent of the strain rate imposed at a fixed temperature. They controlled the process successfully by incorporating biaxially deformed materials at different strain rate into the analytical model.

Lee et al. [13] developed a model on the friction caused by lubrication and surface roughness in sheet metal forming. The friction model considering lubricant viscosity and surface roughness is developed for using in the finite element analysis of sheet metal forming processes. Comparison with current friction model, conventional friction model and experimental measurement has proved the validity and accuracy of the friction model. Kima et al. [14] pointed out finite element analysis for bursting failure prediction in bulge forming of a seamed tube. They proposed a method to predict the bursting pressure and fracture initiation in the bulge forming process.

Mac Donald and Hashmi [15] analyzed die behavior during bulge forming operation using the finite element method. The effect of using internal pressure alone and combined internal pressure and axial compressive load were investigated and it was found that the development of stress and the location of maximum stress was dependent on the type of loading used. Chunfeng et al. [16] worked on numerical simulation of the magnetic pressure in tube electromagnetic bulging. They carried out a numerical simulation of the magnetic pressure acting on the work piece during electromagnetic bulge forming by using FEA software ANSYS. Through measuring the magnetic induction intensity between the coil and the work piece the simulative result are proven to be accurate. Morsy et al. [17] established super plastic characteristics of Ti-alloy and Al-alloy sheets by multi-dome forming test. The multi-dome forming experiments were conducted under constant pressure at super plastic temperature of 800°C for Ti-alloy and of 530°C for Al-alloy. The forming by experiment was verified by simulating using the FEA software. The results were also compared with the tensile test. Experimental and analytical results were in good agreement.

Khraisheh et al. [18] established optimum forming paths for Pb-Sn super plastic sheet materials. Results of forming time, achieved amount of deformation, and thinning behavior are reported for different pressure profiles. The results show that forming profiles based on uniaxial models cannot successfully predict the actual forming behavior when the loading path is biaxial. In fact, the one-dimensional strain rate hardening relation, along with von Mises criterions predict failure at a much higher

strain (time) than the actual case. Ninomiya et al. [19] researched high strain rate super plastic bulge forming of SiC particle reinforced 2124 aluminum alloy composite. It was found that the super plastic formability of the composite with 25% volume fraction of SiC particles is better than that with 17% SiC, corresponding to the measured elongation in the tensile test. The limit bulge height of the sheet with the same SiC volume fraction is increased with increasing initial thickness. The higher forming gas pressures, namely the higher forming rate, lead to the uniform thickness distribution of the bulge part. The maximum thickness strain at the top of the bulge and the applied stress calculated from the forming gas pressure in bulge forming could be concerned with the elongation and the flow stress in the tensile test

Zuo et-al. [20] depicted multi-stage forging process using solid modeling of forging tools. They developed CAD/CAE integration system to simulate the industrial multi-stage metal flow process. Lin et-al. [21] explained finite element analysis of elasto-plastic contact problem in metal forming process. Contact is one of the most significance aspects to simulation of solid model in metal forming and material processing where there is metal flow exist. Hutchinson et-al. [22] experimentally established a formability zone for bulge forming during hydroforming technique. They experimentally explained the effect of plunger for different case and different products were analyzed for their bulge height and wall thickness.

Hashmi [23] presented an analysis for the prediction of wall thickness around the circumference of T-branches formed by hydroforming. In another presentation [24] depicted an analytical method to predict height and thickness distribution of both axisymmetric and asymmetric hydroforming components. The analysis was based on the geometry of the formed bulge. Later Hashmi and Crampton compared experimental result with this analytical method and found that the method generally overestimates the thickness of formed products.

Dohmann and Klass [25] explained axisymmetric bulging of tubes with sliding dies. The dies push the tube ends giving the axial compressive forming load without friction between the die and tube. Hydraulic pressure was used as the internal forming load.

Imaninejad et al. [26] established loading path optimization of tube hydroforming process. Their purpose was to produce a part with minimum thickness variation while

keeping the maximum effective stress below the material ultimate stress during the forming process. They concluded that, in an optimized loading path, the majority of the axial feed needs to be provided after the tube material yields under the applied internal pressure.

Woo [27] presented a limited theoretical method for analysing tube bulging under axial compressive load and internal hydraulic pressure. Experimental results showed reasonable agreement with theoretical results. Kandil [28] reported experimental analysis whereby tubes of different material were bulge formed axisymmetrically under hydraulic pressure only. The experimental results were used to derive empirical relationships between pressure, stress and the geometry of the die and tube. Dohman and Hart [29, 30] presented a flexible die system for tube bulging of both axisymmetric and asymmetric products, the die system has adjustable segments which can expand, displace or reduce the tube blank. This process can control the quality of end products. Filho et al. [31] presented a theoretical analysis of bulge forming of a T-branch using an elastomer rod as the bulging medium. Equations were solved using the finite difference method to determine the axial compressive load required for the process. Tirosh et al. [32] described an upper bound analysis of axisymmetric bulging of tubes by combined internal pressure and axial compression, using this formulation they experimentally attempted to determine an optimum loading pattern to give maximum bulging strain without early failure by buckling or necking.

A lot of research has been carried out in attempting to determine the onset of instability in tubes. Mellor [33] presented an analytical solution to determine the strain at instability of thin walled tubes. In this analysis it was assumed that the circumferential to axial stress ratio remains constant and positive throughout the straining process. In a subsequent work Jones and Mellor [34] experimentally showed that the theoretical solution in [33] was in good agreement with experimental results. Felgar [35] analysed instability of pressure vessels subjected to internal pressure and tensile axial load. Both thin and thick walled pressure vessels were examined for constant circumferential and axial stress ratio. When compared with experimental results, it was found that the

theoretical prediction of instability pressure was accurate, but the prediction of instability strain were in gross disagreement with experimental results. Weil [36] theoretically analysed tensile instability of thin walled cylinders of finite length. The analytical results showed that burst pressures increase progressively as the length/ diameter ratio of the cylinders is reduced from infinity to lower values.

Sungtae et al [37] developed analytical models to determine the forming limits of a tube hydroforming process and demonstrated how the loading path and material parameters influence the forming results. Asnafi [38] developed analytical models to show the limits during the free forming and how different materials and process parameters influence the loading path and the forming results.

Manabe et al [39] simulated and studied the factors effecting wall thickness distribution of the hydro formed tube. The results were also validated experimentally. They demonstrated that axial loading and better lubrication condition would improve the thickness distribution. It was shown that the fracture location depends upon the process conditions and materials properties.

Rimkus et al [40] analytically established and designed the load parameter for a successful tube hydroforming process. In their work, it was assumed that the hydroforming pressure and axial force are functions of time. The methodologies were defined to derive the load paths for internal pressure and axial compressive load. [41] In very recently Ray and Mac Donald ascertained the optimal load path for tube hydroforming process using a fuzzy load control algorithm and finite element analysis. This process avoids the failure of the tube due to excessive induced strain during the forming process.

2.3 Summary of the chapter

It is clear that a study of metal and sheet metal forming has been described from early twentieth century in this chapter. Application of finite element analysis in the field of metal forming has been presented. Previous and ongoing research hydro bulge forming has been depicted clearly. Small case of solid bulging and multi layered hydroforming has been presented as well.

CHAPTER THREE

Theoretical Background

3.1 Introduction

The purpose of this chapter is to provide a basic theoretical out line of the numerical methods used to solve the problems as described in later chapters. This chapter is not intended as a text on the finite element method, rather as a description of how the method was utilised here, and hence the reader unfamiliar with the method is referred to the referenced the references section.

3.2 The finite element method

The basic steps in any finite element analysis are discretization, Determination of element behaviour, transformation of element behaviour to Global Axis, assembly of global element equation, application of boundary condition, solution for nodal unknown and calculation of element results.

Discretization

The problem domain is divided into a number of regularly shaped sub domains called finite elements. Each element contained a number of nodal points which have known co-ordinates relative to the global problem co-ordinate system. The shape of the element is defined in terms of the coordinates of these nodal points or interpolation or shape functions.

Determination of Element Behaviour

An interpolation function is assumed for the variation of the unknown across each element. For each element, coefficient matrices that describe the response characteristics of the element are determined. In the case of stress analysis this matrix corresponds to the element stiffness matrix.

Transformation of Element Behaviour to Global Axis

The element stiffness matrices naturally lie parallel to the element local coordinate system. In order to solve the entire problem these matrices have to be transformed to align with the global coordinate system.

Assemble of Global Element Equations

The transformed stiffness matrix for each element is now combined in order to determine the stiffness matrix for the entire problem domain. This forms a matrix equation defining the behaviour of the entire solution domain.

Application of Boundary Conditions

In order for the problem to be solved some of the nodal unknowns must be restrained and will not be arbitrary in value.

Solution for nodal unknowns

The primary nodal unknowns are determined by solving a set of linear algebraic equations. In most problems the number of equations to be solved is very large thus special solution techniques are employed. After solution the value of the dependant variable is at each node is known.

Element Resultants

Using the nodal values and interpolation functions secondary or derived quantities such as stress and strain are determined.

3.3 General theory of a finite element Equilibrium

There are numerous methods of solving the finite element solutions; among those the principle of virtual displacement is one of them. The principle states that for any compatible small virtual displacement due to infinitesimal external forces the internal virtual work on the body is equal to the external virtual work acting upon the body. The internal virtual work is equal to the actual stress going through the virtual strain. The actual force going through the virtual displacement gives the external work. In

order to express the general finite element theory we consider the equilibrium of a three dimensional body which located in the fixed co-ordinate system X, Y, Z.

The body is subjected to externally applied body force f^B (force per unit volume) and concentrated load F^i (where i. denotes the point of load application), surface traction f^s, resulting in virtual displacement U, virtual stress σ and virtual strain ε,

So the principle can be stated as

$$\int_V \{\bar{\varepsilon}\}^T \{\sigma\} dv = \int_V \{\bar{U}\}^T \{f^B\} dv + \int_S \{\bar{U}\} \{f^S\} dS + \int_i \{\bar{U}\}^T F^i \qquad (1)$$

Where:

$$\{\bar{\varepsilon}\}^T = \begin{bmatrix} \bar{\varepsilon}_{xx} & \bar{\varepsilon}_{yy} & \bar{\varepsilon}_{zz} & \bar{\gamma}_{xx} & \bar{\gamma}_{yy} & \bar{\gamma}_{zz} \end{bmatrix}$$

$$\{\sigma\}^T = \begin{bmatrix} \sigma_{xx} & \sigma_{yy} & \sigma_{zz} & \sigma_{xy} & \sigma_{yz} & \sigma_{zx} \end{bmatrix}$$

$\{\bar{U}\}^T = \begin{bmatrix} \bar{U} & \bar{V} & \bar{W} \end{bmatrix}$ and $\bar{U}$, $\bar{V}$ and $\bar{W}$ are displacements in global directions

$\{f^B\}^T = \begin{bmatrix} f_x^B & f_y^B & f_z^B \end{bmatrix}$ where superscript B indicates body

$\{f^S\}^T = \begin{bmatrix} f_x^S & f_y^S & f_z^S \end{bmatrix}$ where superscript S indicates surface

$\{F^i\}^T = \begin{bmatrix} F_x^i & F_y^i & F_z^i \end{bmatrix}$ where superscript i indicates points

As the problem domain is approximated by an assembly of finite elements which are interconnected at nodal points on the element boundaries, the displacements measured within each element are assumed to be a function of the displacements at the nodal points. Thus for element m,

$$u^{(m)}(X,Y,Z) = H^{(m)}(X,Y,Z)\hat{U} \qquad (2)$$

Where $H^{(m)}$ is the displacement interpolation matrix or shape function for element m and $\hat{U}$ is a vector of the three global displacement components U_i, V_i and W_i at all nodal points.

Using this assumption, equilibrium equations that correspond to the nodal point displacements of the assembly of finite elements can be constructed from equation (1) and (2)

$$\sum_{m}\int_{V(m)}\varepsilon^{(m)T}\sigma^{(m)}dV^{(m)}=\sum_{m}\int_{V(m)}\bar{U}^{(m)T}f^{B(m)}dV^{(m)}+\sum_{m}\int_{S(m)}U^{\bar{S}(m)T}f^{S(m)}dS^{(m)}+\sum_{m}\bar{U}^{iT}F^{i}\ldots(3)$$

From the assumption on displacements in equation-(2) the corresponding element strains can be determined as:

$$\varepsilon^{(m)}(X,Y,Z)=B^{(m)}(X,Y,Z)\hat{U} \tag{4}$$

Where $B^{(m)}$ is the strain-displacement matrix for element m. The rows of $B^{(m)}$ are obtained by appropriately differentiating and combining rows of matrix $H^{(m)}$.

The stress within a finite element are related to the element strains and initial stresses by

$$\sigma^{(m)}=D^{(m)}\varepsilon^{(m)}+\sigma^{I(m)} \tag{5}$$

Where $D^{(m)}$ is a matrix which relates stress to strain in element m and $\sigma^{I(m)}$ is the element initial stresses, $D^{(m)}$ is essentially a matrix which contains the materials behaviour of the element and may be isotropic or anisotropic and may vary from element to element. Using equation(2), (4) and (5) we can rewrite equation- (3) as:

$$U^{T}\left[\sum_{m}\int_{V(m)}B^{(m)T}D^{(m)}B^{m}dV^{(m)}\right]\hat{U}=\hat{U}^{T}\left[\begin{array}{l}\left\{\sum_{m}\int_{V(m)}H^{(m)T}f^{B(m)}dV^{(m)}\right\}+\\ \left\{\sum_{m}\int_{S(m)}H^{S(m)T}f^{S(m)}dS^{(m)}\right\}-\\ \left\{\sum_{m}\int_{V(m)}B^{(m)T}\sigma^{I(m)}dV^{(m)}\right\}+F\end{array}\right] \tag{6}$$

Where $H^{S(m)}$ is the surface displacement interpolation matrix for element m, and is obtained from the volume displacement interpolation matrix, $H^{(m)}$ in equation (2) by

substituting the element surface coordinates. F is a vector of the externally applied forces to the nodes of the finite element assembly. It may be noted that in equation (6) the nodal point displacement vector, $\hat{U}$ is outside the summation sign as it is independent of the element considered.

In order to obtain the equations for the unknown nodal point displacements from equation (6), the virtual displacement theorem is utilised by imposing unite virtual displacements in turn at all displacement components. This results in $\hat{U}^T = I$ (where I is the identity matrix) and by denoting $\hat{U}$ by U, the equilibrium equation of the element assemblage corresponding to the nodal point displacements is:

$$KU = R \tag{7}$$

The matrix K is the global stiffness matrix and is given by :

$$K = \sum_{m} \int_{V(m)} B^{(m)T} D^{(m)} B^{(m)} dV^{(m)} \tag{8}$$

The load vector $R = R_B + R_S - R_I + R_C$, where R_B is the effect of element body forces:

$$R_B = \sum_{m} \int_{V(m)} H^{(m)T} f^{B(m)} dV^{(m)} \tag{9}$$

R_S is the effect of element surface forces and is given by:

$$R_S = \sum_{m} \int_{S(m)} H^{S(m)T} f^{S(m)} dS^{(m)} \tag{10}$$

R_I is the effect of element initial stresses and is given by:

$$R_I = \sum_{m} \int_{V(m)} B^{(m)T} \sigma^{I(m)} dV^{(m)} \tag{11}$$

And R_C=F (i.e. the concentrated forces)

Equation (7) is a statement of the static equilibrium of the finite element mesh. In equilibrium considerations, applied forces may vary with time, in which case the displacements may also vary with time. In such a case equation (7) is a statement of equilibrium for specific point in time. If in reality the loads are applied rapidly, inertia forces must be considered and dynamic problem must be solved. Using D' Alembert's principle, the element inertia forces may be included as part of the body forces. In such a case equation (9) becomes:

$$R_B = \sum_m \int_{V(m)} H^{(m)T} \left[f^{B(m)} - \rho^{(m)} H^{(m)} \ddot{U} \right] dV^{(m)} \tag{12}$$

Where $f^{B(m)}$ no longer includes inertial forces, $\ddot{U}$ gives nodal point accelerations and $\rho^{(m)}$ is the mass density of element m. In this case the equilibrium equations are:

$$M\ddot{U} + KU = R \tag{13}$$

Where K is the global stiffness matrix, M is the global mass matrix and R and U is time dependant. The global mass matrix is given by:

$$M = \sum_m \int_{V(m)} \rho^{(m)} H^{(m)T} H^{(m)} dV^{(m)} \tag{14}$$

However , in a dynamic analysis some energy is dissipated during vibration, which in vibration analysis is usually taken account of by introducing velocity dependant damping force. Introducing the damping forces as additional contributions to the body forces changes equation (12) as follows:

$$R_B = \sum_m \int_{V(m)} H^{(m)T} \left[f^{B(m)} - \rho^{(m)} H^{(m)} \ddot{U} - K^{(m)} H^{(m)} \dot{U} \right] dV^{(m)} \tag{15}$$

Where $\dot{U}$ is a vector of the nodal point velocities and $K^{(m)}$ is the damping property parameter of element m. in this case the equilibrium equations become:

$$M\ddot{U} + C\dot{U} + KU = R \tag{16}$$

Where C is the global damping matrix and can be written as:

$$C = \sum_m \int_{V(m)} K^{(m)} H^{(m)T} dV^{(m)} \tag{17}$$

3.4 Non Linearity

In the above formulation it was assumed that the displacements of the finite element assembly are small, that the material is linearly elastic and that the boundary conditions remain unchanged during the application of loads. These assumptions have entered the equilibrium equation in the following manner:

The fact is that all integrations have been performed over the original volume of the finite elements implies that displacements must be small. This effects the stiffness matrix K, and the load vector, R.

The strain displacement matrix B of each element was assumed to be constant and independent of element displacements.

The assumption of a linear elastic material is implied in the use of a constant stress-strain matrix, D.

The unchanged boundary conditions are implied by keeping constant constraint relations for the complete response.

These observations point to the different types of non-linearity that may arise in a finite element analysis [48]

1. Material non linearity.
2. Non linearity due to large displacements, large rotations, but small strains.
3. Non linearity due to large displacements, large rotations and large strains.
4. Non linearity due to large displacements, large rotations, small strains.
5. Contact non linearity.

3.5 Solution methodology

There are a number of solutions techniques available for use with the finite element method. Since the analysis of this work is primarily concerned with non linearity, this section will focus on solution methodology for non linear problems. The basic step in a general non linear analysis is to determine the state of equilibrium of the body corresponding to the applied loads. Assuming that the external loads are described as a function of time, the equilibrium condition of the finite element assembly can be written as:

$${}^{t}R - {}^{t}F = 0 \tag{18}$$

Where ${}^{t}R$ gives the externally applied nodal point forces at time t and the vector ${}^{t}F$ lists the nodal point forces corresponding to the element stresses, where:

$${}^{t}R = {}^{t}R_B + {}^{t}R_S + {}^{t}R_C \tag{19}$$

$${}^{t}F = \sum_{m} \int_{{}^{t}V(m)} {}^{t}B^{(m)T} \, {}^{t}\sigma^{(m)t} \, dV^{(m)} \tag{20}$$

It may be noted that in a dynamic analysis the vector ${}^{t}R$ would also include the inertial and damping forces.

Equation (18) must express the equilibrium of the system in the current defined geometry by taking account of all non Linearities and must be satisfied throughout the complete history of load application. The solution process is carried out using a step by step incremental analysis. The basic approach in an incremental solution is to assume that the solution for the discrete time t is known and that the solution for a discrete time $t + \nabla t$ equation-(18) can be written as:

$${}^{t+\nabla t}R - {}^{t+\nabla t}F = 0 \tag{21}$$

Since the solution at time t is known it can be written that

$${}^{t+\nabla t}F = {}^{t}F + F \tag{22}$$

Where F is increment of nodal point forces corresponding to the increment of element displacements and stresses from time t to time $t + \nabla t$. This vector can be approximated using a tangent stiffness matrix ${}^{t}K$ which corresponds to the geometric and material condition at time t.

$$F \cong {}^{t}KU \tag{23}$$

Where U is the vector of incremental nodal point displacements. By combining equations (21), (22) and (23) we get:

$${}^{t}KU = {}^{t+\nabla t}R - {}^{t}F \tag{24}$$

By solving this equation for U and approximation to the displacements at time $t+\nabla t$ can be calculated:

$${}^{t+\nabla t}U = {}^{t}U + U \tag{25}$$

Having evaluated an approximation to the displacements corresponding to time $t+\nabla t$ an approximation for stresses and corresponding nodal point forces at time $t+\nabla t$ can be obtained. However, because of the approximation expressed in equation-24, such a solution may be subject to significant errors and may be unstable. In practice it is frequently necessary to iterate until equation 21 is satisfied to sufficient accuracy.

Different solution procedures exist for the solution of equation 24 n. in this work the explicit time integration method was used and will be briefly outlined. The most common explicit time integration operator used in non linear dynamic analysis is the central difference operator. The equilibrium of the finite element assembly is considered at time t in order to calculate the displacements at time $t+\nabla t$. Solution is sought for each time step for the equilibrium equation neglecting the effect of damping which may be expressed as

$$M\,{}^{t}\ddot{U} = {}^{t}R + {}^{t}F \tag{26}$$

Where the nodal point force vector F is evaluated on the basis of the methods used to formulate the material and geometric non linearity's. This involves the choice of element type, the kinematics description and the kinetic description, all of which are problem dependant. The solution for the nodal point displacements at time $t+\nabla t$ is obtained using the central difference approximation for the acceleration as follows:

$$\ddot{U} = \frac{1}{\nabla t^{2}}\left\{{}^{t-\nabla t}U - 2\,{}^{t}U + {}^{t+\nabla t}U\right\} \tag{27}$$

Combining this with (26) gives:

$$\frac{M}{\nabla t^2}\left\{{}^{t+\nabla t}U\right\} = {}^{t}U - {}^{t}F - \frac{M}{\nabla t^2}\left\{{}^{t-\nabla t}U - 2{}^{t}U\right\} \tag{28}$$

Thus, if ${}^{t-\nabla t}U$ and ${}^{t}U$ are known then ${}^{t+\nabla t}U$ can be determined from equation (28). A disadvantage in the use of this method is that for stability, the time step size ∇t must be smaller than a critical time step size ∇t_{CR} which is equal to T_n / π, where T_n is the smallest period in the finite element assembly.

3.6 Summary of the chapter

It can be summarised that a procedure of finite element analysis has been described in this chapter. A chronological step by step of the solving method has been presented. The theorem relation to mechanics in or order to analyze finite element simulation has been described elaborately. A brief description of nonlinearities was presented.

CHAPTER FOUR

Analytical Modeling and Experimental Procedure

4.1 Introduction

This chapter presents the analytical modelling procedure and experimental results of multilayered tube forming of T and X branches by using finite element software ANSYS. A step by step procedure of the modelling has been discussed. The simulation was carried out by ANSYS implicit and explicit finite element codes. An experimental procedure and the results of the experiments have been presented in this chapter. A photographic view of the bulge forming machine has been included.

4.2 Modelling

4.2.1 Solid 3-D structural modelling

Modelling and idealisation of the problem is the most important step in the case of finite element simulation. During metal forming analysis good modelling of deformed body is of most important in order to achieve an accurate solution. In this work 3-D models have been built up by ANSYS pre-processor with structural solid brick elements for analysing the process with ANSYS implicit and explicit finite element codes. The basic steps to build and analyse a model using ANSYS are:

- Create the model geometry
- Define the element types and real constants
- Specify material properties
- Mesh the model
- Define contact surfaces
- Apply boundary condition
- Solution

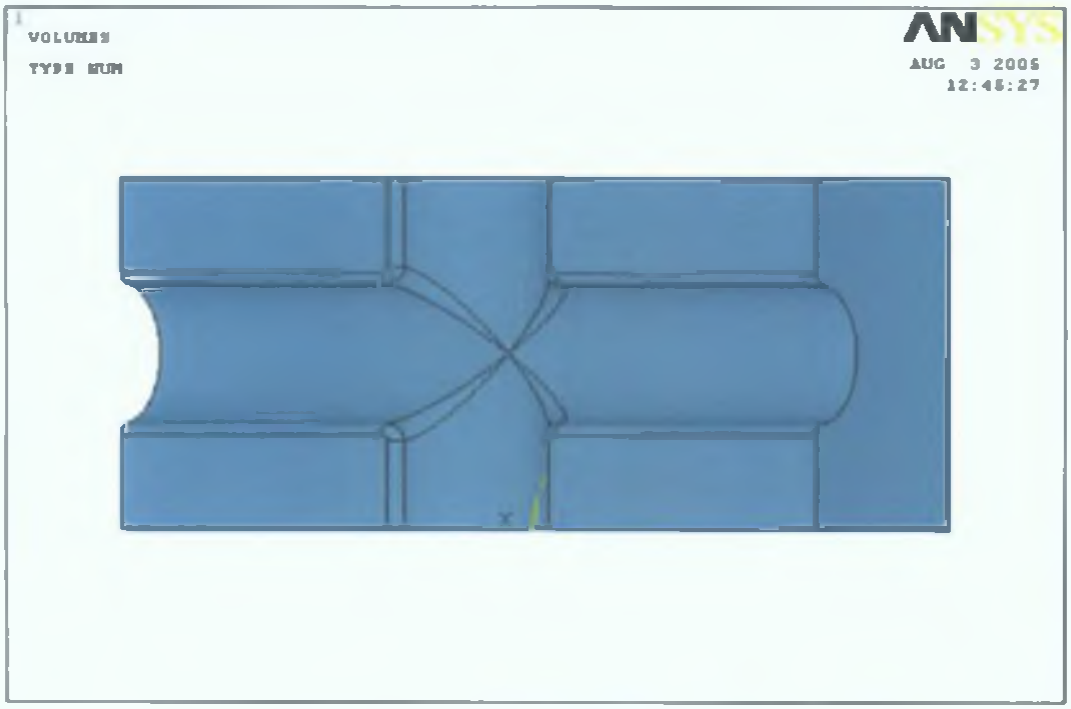

Figure 4.1.: Pre-shaped die half of an X branch solid model

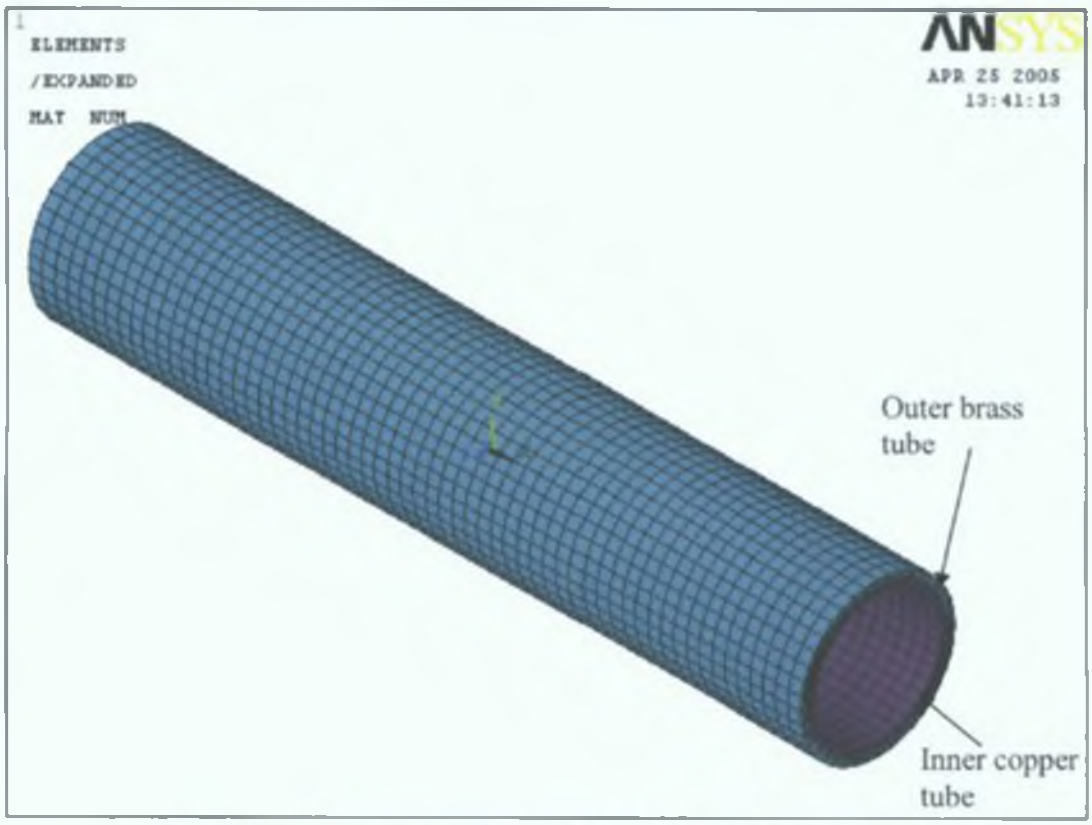

Figure 4.2.: Finite element Modelled of a Bi-layered tube

The solid model consists of the die body of pre-shaped formed product, and the multi-layered tube. Figure 4.1 and 4.2 present pre-shaped die half and multi-layered FE model respectively. Since it was considered that during the deformation the die would not be deformed, so the die surface would be considered as rigid model. The materials of the outer and inner tubes are brass and copper respectively. The dimension of the brass and copper tube are 24 mm and 22mm OD and 22mm and 20.2 mm ID respectively. The length of the tubes is 120 mm. The copper tube was inserted into the brass tube with loose fit. After applying internal pressure at the surface of the inner tube, it will expand and then it will be tight fit. The model has been created in this research as solid volume by using ANSYS pre-processor. In this work the element was defined as a solid -8 nodes 185 brick element.

4.2.2 Mesh- Modelling

The tubes were modelled using solid brick elements and the die was assumed to be rigid. In this project a mapped mesh has been created for both brass and copper tubes. In order to build a fine mesh the tube was divided by using the mesh tool and line set. Volume meshing command was applied for both tubes. The die surfaces have been defined as rigid target surfaces for the contact analysis.

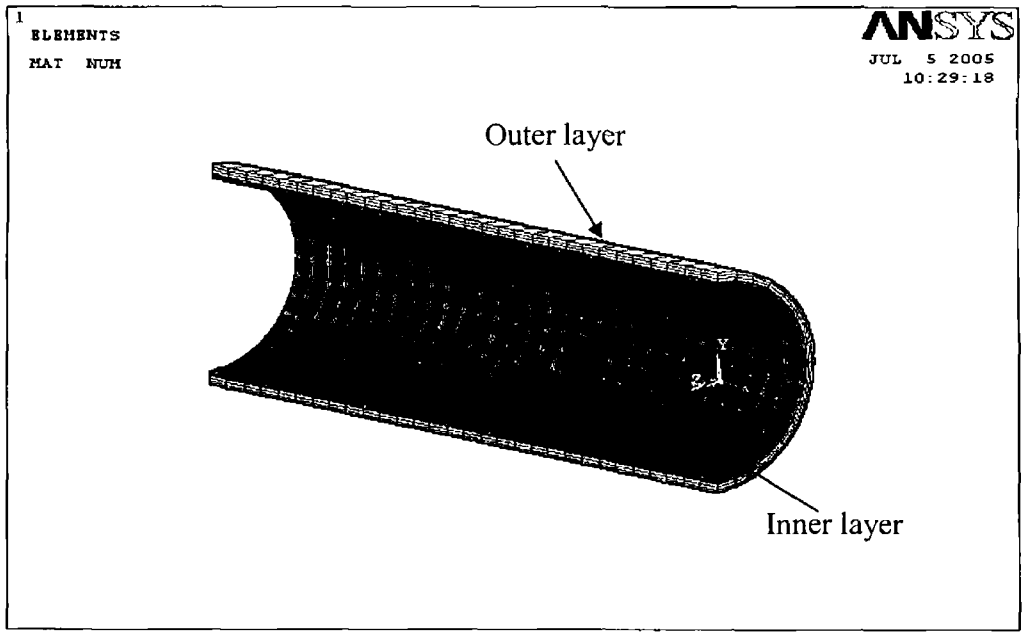

Figure 4.3.: Mapped mesh of the quarter FEA model

4.2.3 Contact Modeling

Contact problems are highly nonlinear and require significant computer resources to resolve. In contact analysis, two points should be considered, first the contact and secondly the target. In ANSYS simulation, it is possible to solve both implicit and explicit contact analysis. The model consists of both rigid-to-flexible and flexible-to-flexible. Since we assumed that the die surfaces are rigid and only the tube will be deformed, so rigid-to-flexible contact element 174 has been created between die surface and the external surface of the brass tube. Contacted surfaces between the tubes are modeled as flexible-to-flexible contact pair. This is one of the common types of contact pair at which both the surface would be deformed.

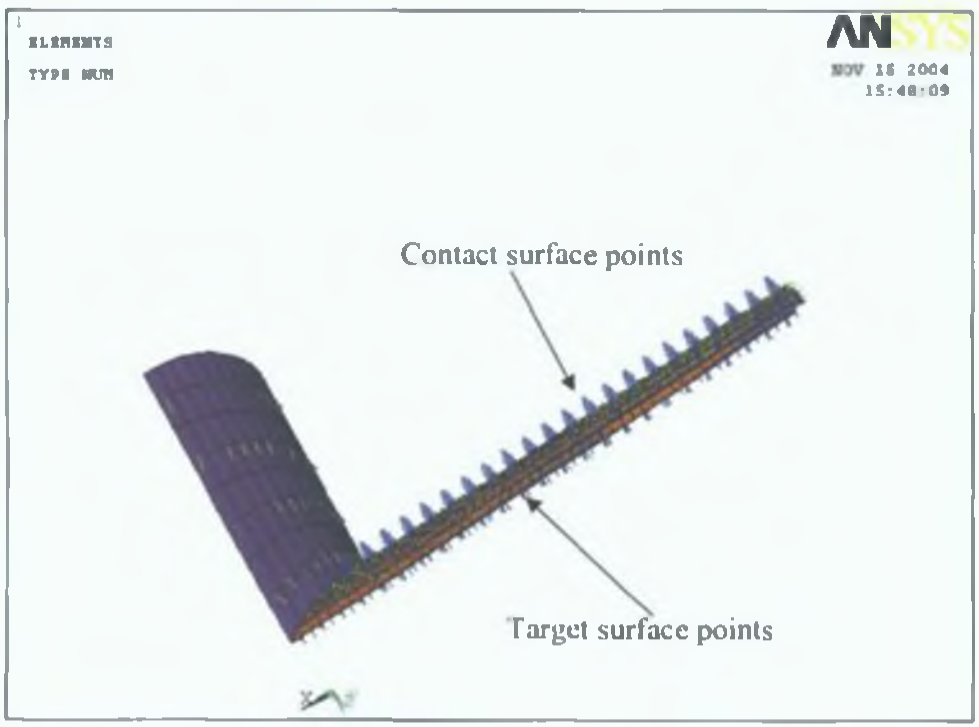

Figure 4.4.: Rigid to flexible surface-to-surface contact pair

In this research both types of contact pair has been analyzed. Figure 4.4 shows the rigid to flexible surface-to-surface created contact pair. In order to create this type of contact element, the rigid die surfaces should be left unmeshed during the meshing operation and these surfaces would be meshed by the system automatically by creating the contact

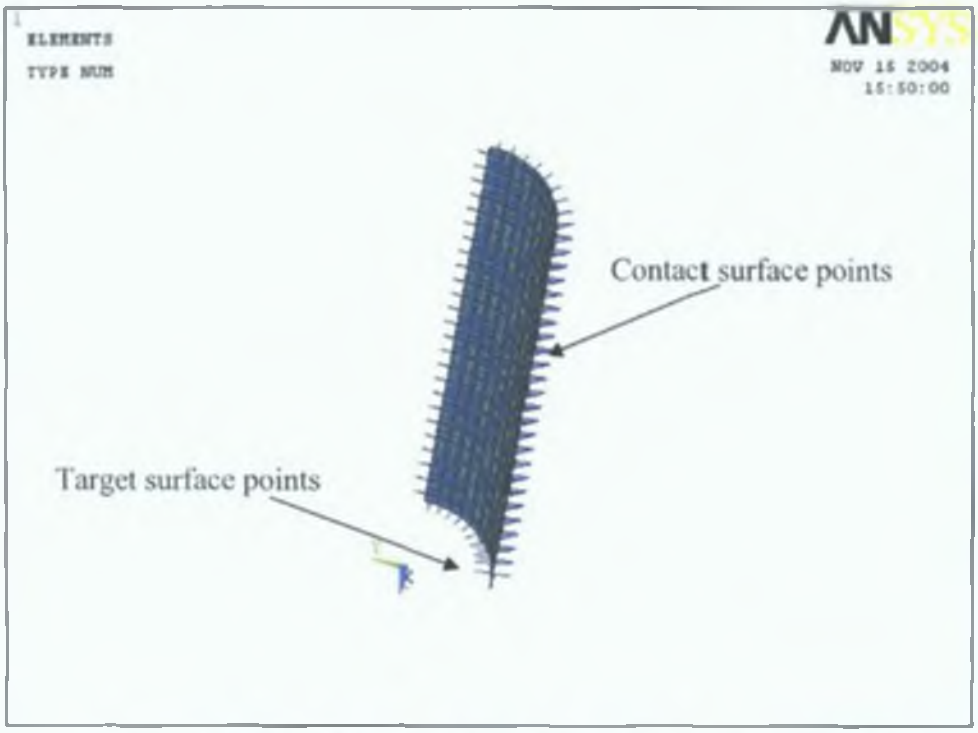

Figure 4.5.: Flexible to flexible surface-to- surface contact pair

elements. An elastic coulomb friction law was assumed and the value of the coefficient of friction was assigned as 0.15. The second contact pair has been created between the inner and outer tubes contacted surfaces. In this case the inner surface of the outer tube has been considered as target surface and outer surface of the inner tube was assumed as contact surface. During the simulation both surfaces would be deformed simultaneously. A sticky friction law has been assumed and the maximum value of the coefficient of friction has been applied which is 0.577. Figure 4.5 presents the flexible to flexible surface-to-surface contact element.

4.3 Boundary Conditions

Boundary condition is the most significant step in finite element simulation. In this simulation the pressure and the end axial feed were applied. The load functions were defined as nonlinear functions with respect to simulation time. The pressure was applied on the inner surfaces of the internal copper tube and the axial displacement was applied at the tubes end areas. The die was constrained in all degrees of freedom as assumed that it

would not be deformed. As the die surfaces have been assumed to be rigid. The tubes ends were allowed to move only towards the axial direction.

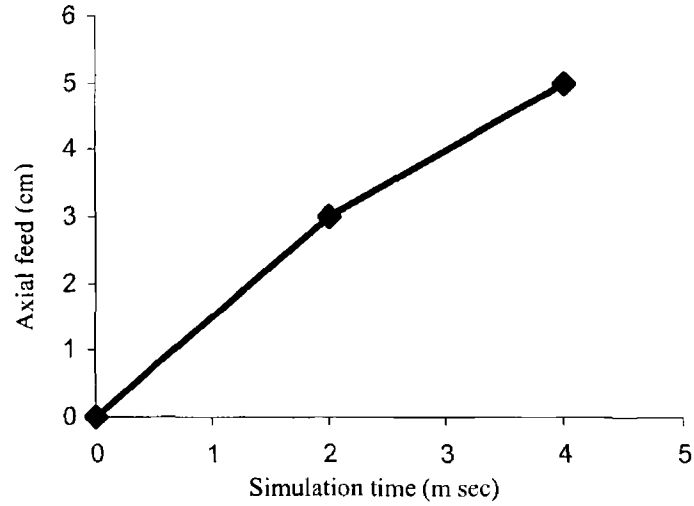

Figure 4.6.: Non-linear axial load pattern

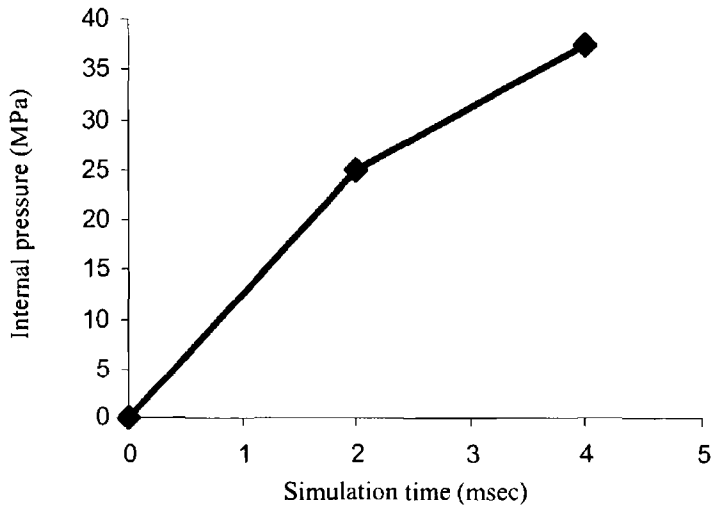

Figure 4.7.: Non-linear internal pressure load pattern

Experimentally the axial feed was applied by end punch but in the simulated model the axial feed was applied as displacement along the positive X direction in the global co-

ordinate system. As a results of the constraints tubes end nodes would not be able to move along the normal direction of the circumference of the blank rather than X direction. Figure 4.6 is depicting the non linear axial load pattern. It can be seen that it has been defined by two regimes. Figure 4.7 is describing the internal pressure function. Both loads function have been defined using ANSYS pre-processor loading table parameters in two regimes.

4.4 Material Model

The bi-layered tube model has been built with solid brick, 8-node 185 elements and the die has been assumed to be rigid surface. An elasto-plastic (bilinear isotropic hardening) nonlinear material property was used with the following material properties. The outer tube was commercial brass and the inner tube was copper. The interface between the die and the outer layered of the blank was modelled using the rigid to flexible surface-to-surface contact element and the friction co-efficient was assumed 0.15 considering that the material can flow smoothly during deformation of hydroforming process. Table 4.1 describes the material composition of brass tube and the mechanical properties [49] and Table 4.2 shows the material properties of internal copper tube. Some of the properties have been supplied by the material supplier company and other properties have been taken form the reference mentioned according to the chemical composition. Figure 4.8 and 4.9 show the material models used for external tube material brass and internal tube material copper respectively.

Table 4.1, Materials Properties of Brass

Chemical compositions of Brass.	Cu = 62-64% Fe = 0.1% Pb = 0.1% Zn = 36.5-37.5% Al = 0.03 % Ni = 0.3% Mn = 0.05% Sn = 0.1%
Ultimate Tensile Strength	540 MPa
Tensile Yield Strength	170 MPa
Breaking strain	0.4
Young's Modulus	105 GPa
Poisson's Ratio	0.34
Tangent Modulus	720 MPa
Density	8.44 g/cc

Table 4.2, Materials Properties of Copper

Chemical composition of Copper	Cu = 99.5% Fe = 0.01% Pb = 0.01% Other = 0.48 %
Ultimate Tensile Strength	470 MPa
Tensile Yield Strength	365 MPa
Failure strain	0.20
Young's Modulus	105 GPa
Poisson's Ratio	0.34
Tangent Modulus	552 MPa
Density	8.81 gm/cc

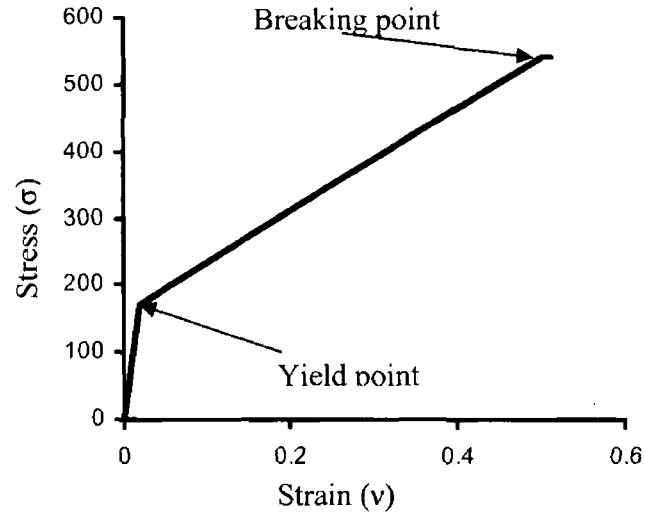

Figure 4.8.: Material model used for brass tube

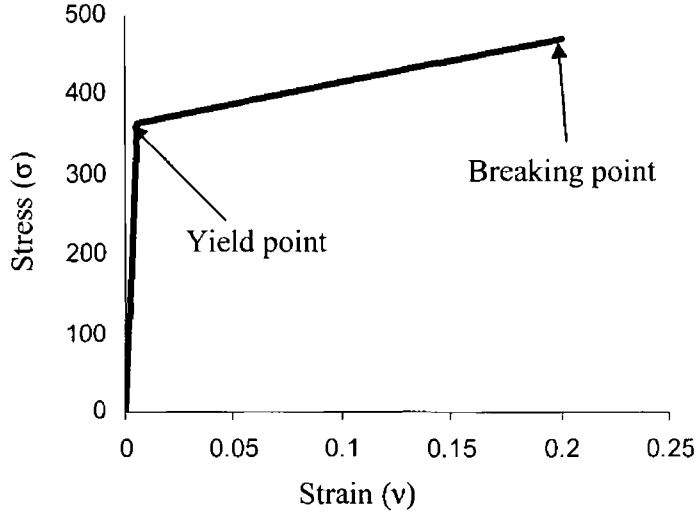

Figure 4.9.: Material model used for copper tube

4.5 Solution

The tube model was created as a volume by the ANSYS pre-processor; the elements were defined as solid brick 8 node 185 elements. The die surfaces were assumed to be rigid for the simulation purpose assuming that during the deformation the metal would flow along the surface without any deformation on the die. The tubes volume were mapped meshed uniformly using the line division by the mesh tool. The line division has been used in order to perform fine mesh. The die surfaces were left unmeshed in order to define the rigid target surface to create rigid to flexible contact pair. An elastic coulomb friction law was assumed a friction co-efficient has been assigned as 0.15 where the material can flow smoothly during the simulation without experiencing any reaction force due to the surfaces roughness. The directions of normal for both target and contact surfaces were checked properly, the normals of the tube contact surface elements points towards the rigid die surface and the normals of the rigid die contact elements towards the outer layered tube contact surface element during the course of simulation. To reduce the simulation time the penalty stiffness factor, penetration depth tolerances and the number of element in the tube were selected reasonably.

Elasto-plastic bilinear isotropic hardening material properties were used with the properties presented in table 4.1 and table 4.2 for both the internal and external tubes respectively. In order to avoid failure due to bursting the maximum equivalent von-Mises stress was limited to the average ultimate strength of the materials. The thickness of the external tube was 1mm and the internal tube thickness was 0.9 mm, total thickness was 1.9 mm. The length of the tube blank was 120 mm.

4.5.1 T branch hydro forming

In order to reduce processing time and measuring constraints, symmetry has been utilized to give a quarter model for analysis using appropriate boundary conditions. Figure 4.10 presents quarter symmetry of the FEA model for this analysis. Simulations have been carried out by applying both internal pressure and the axial load simultaneously. Both

load patterns were chosen as non-linear, where the solution has been solved for non-linear conditions. The loads have been applied

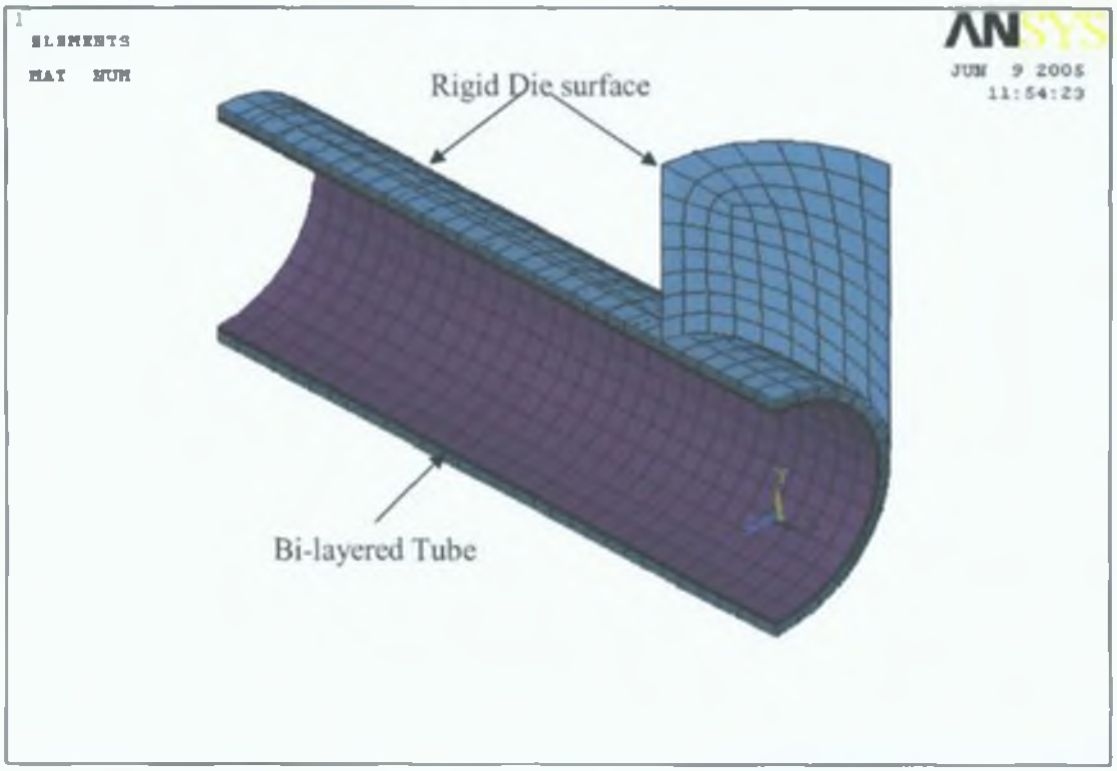

Figure 4.10.: Quarter symmetry of a T branch FEA model

with respect to time at two different regimes, first regime's limit is 0 to 2 msec and last regime's limit was 2 to 4 msec. The pressure load was applied as surface load on the inner surface of the internal tube. Maximum pressure load was limited to 37.5 MPa due to the maximum pressure capacity of the hydro bulge forming machine was 37.5 MPa. The axial feed was applied at the edges of the tubes surfaces and the direction of the axial load was checked properly to the positive X direction in the global co-ordinate system. The maximum value of the axial feed was limited to 5 mm for each symmetry solution.
Figures 4.11 and 4.12 present the loading pattern applied in the simulation. These loads patterns have been selected according to the load pattern of the hydro bulge

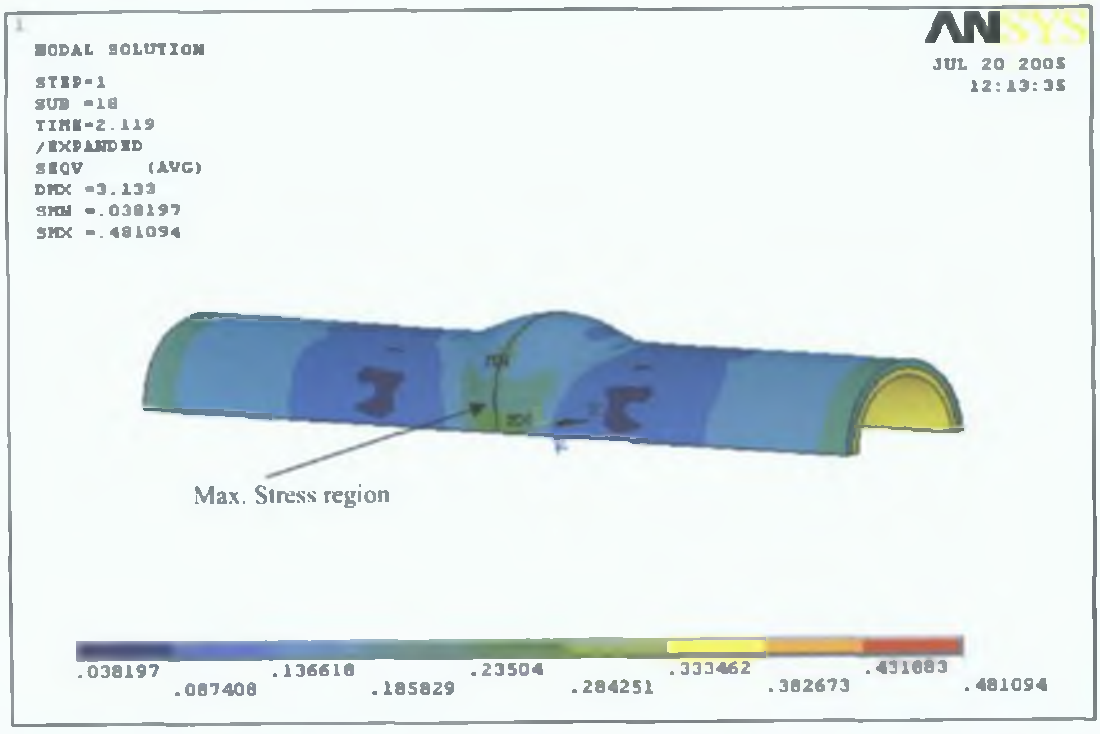

Figure 4.11.: Von Mises stress distribution over the simulated T-branch in hydroforming process with 10 mm Axial feed and 37.5 MPa internal pressure

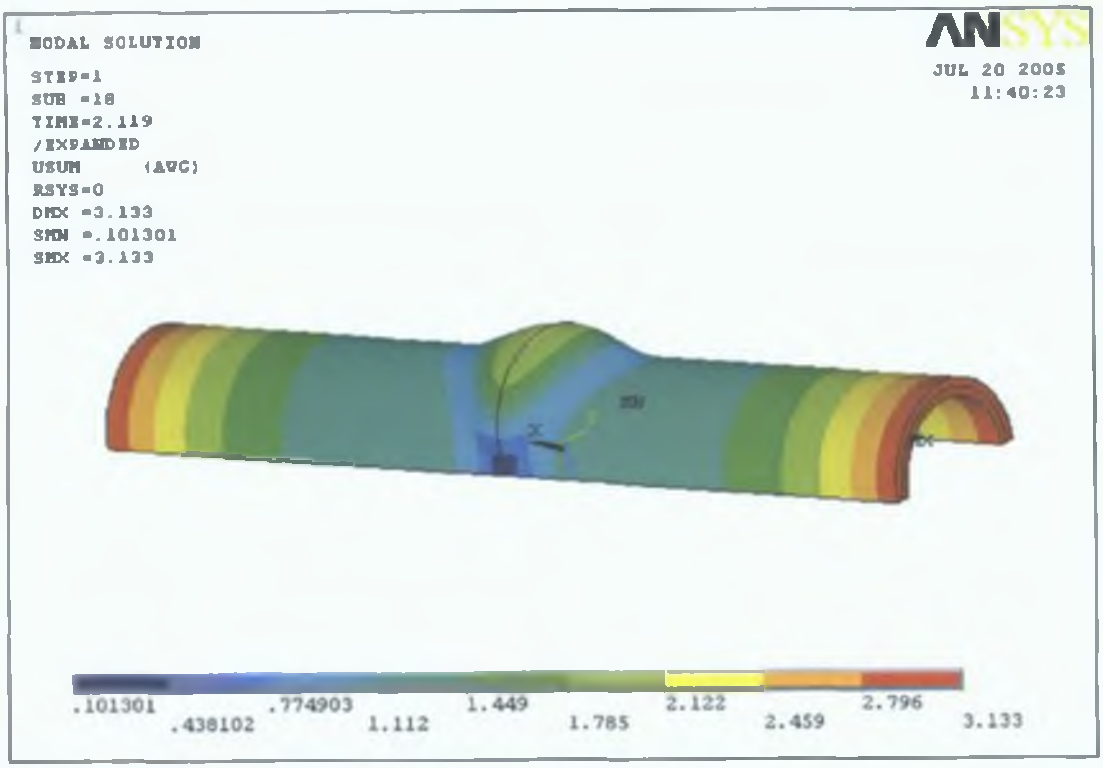

Figure 4.12.: Maximum T branch height formed in hydroforming process with 10 mm axial feed and 37.5 MPa internal pressure

forming machine [45]. The solution has been controlled by defining the large static displacement, saving all the readings of the sub steps in the result file. The result file was used to analyze the time history post processing. The total solution was completed by 4 mseconds. The maximum stress developed in the simulated tube is 481 MPa which is well below the ultimate stress of the external tube materials. It has been observed that the maximum stress generally developed in the external tube region, for this reason it is the main concern to observe the stress state of the outer layered tube during hydroforming of multi-layered tube. It has been observed that after a time of 2.119 msecond the stress developed in the bi-layered tube exceeds the ultimate stress of the material. It is assumed that after this time the material failed theoretically and all the solutions have been ignored. Figure 4.11 shows the Von Mises stress distribution of the simulated tube. It is clear from the figure that maximum stress has been developed in the bottom region of the formed T branch. The stress over the top area of the branch was distributed very uniformly which signifies a good condition of the formed products. Figure 4.12 depicts the formed branch of this simulation at a time of 2.119 msecond and it is clear from the figure that the maximum T branch height is about 3.133 mm; it is a bit less than the expected deformation. This was due to the very high thickness of the total tube compared to the amount of load (internal pressure and axial feed). It can be stated that according to the thickness materials, proper loading condition is one of the important factors in carrying out the simulation properly. Figure 4.13 presents distribution of different stresses over the top central node in the external tube for this simulation. It can be noticed from the figure that hoop stress is dominant over the simulation time which is more convenient for the forming conditions. Also the radial stress is compressive during the solution steps. Hoop stress was steady within elastic limit and increased merely linear up to the end of the solution. Figure 4.14 describes the stresses distribution over the top central node of the internal tube of the T branch. It is clear that equivalent stress increases at a constant rate over the simulation time and it is higher than the external tube.

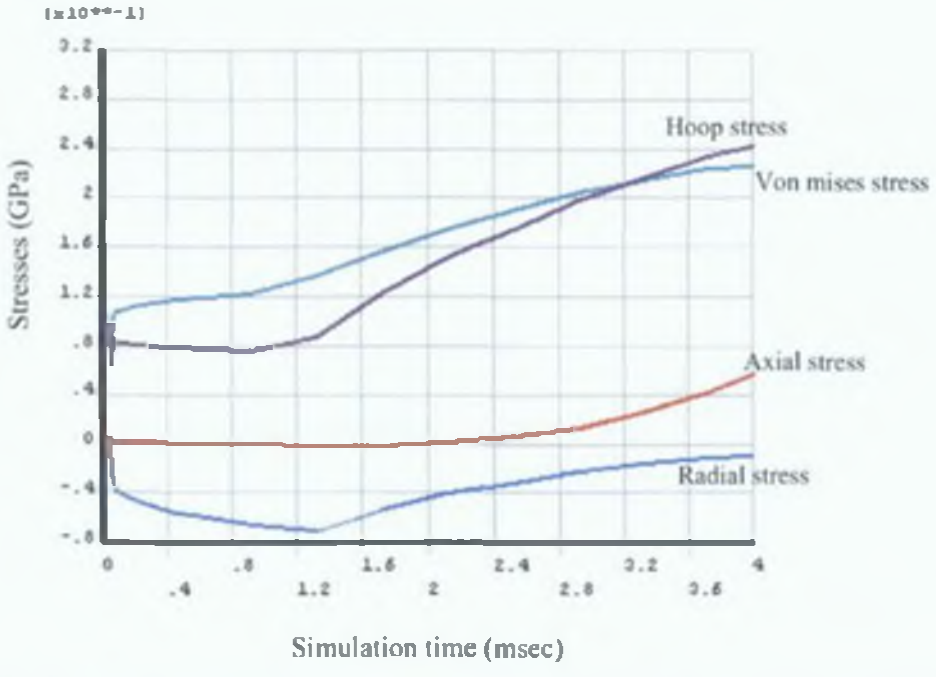

Figure 4.13.: Stresses distribution over a top central node of the simulated T branch in hydroforming process by 10 mm axial feed and 37.5 MPa internal pressure

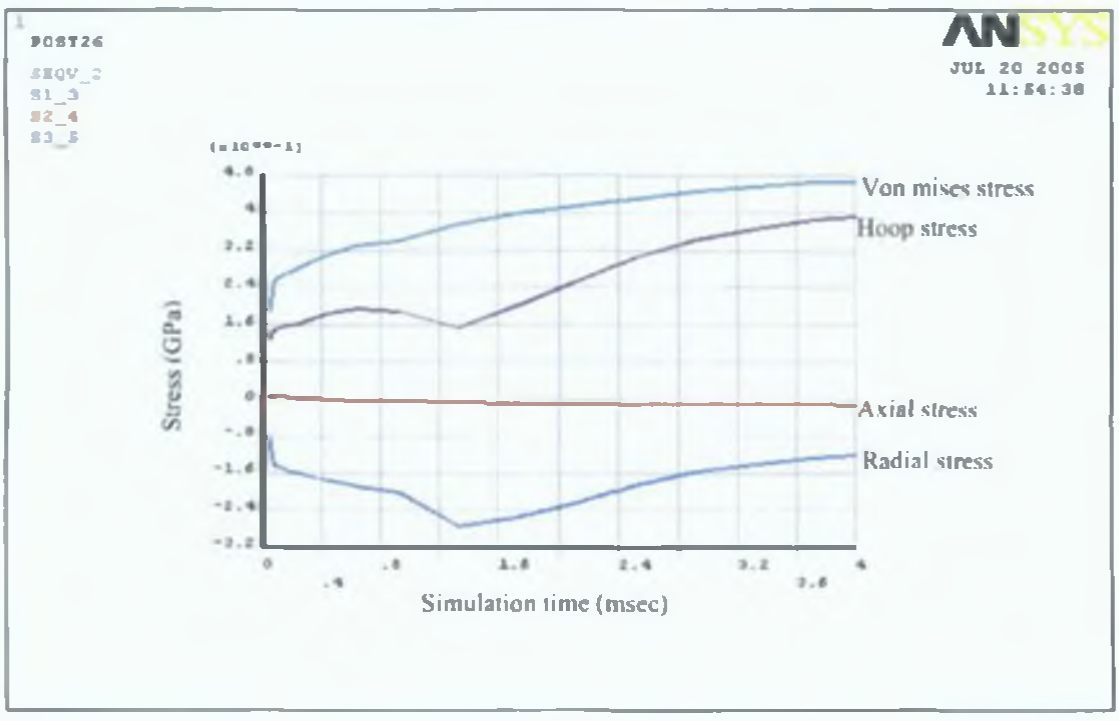

Figure 4.14. : Development of stresses over the top central node for internal tube of the simulated T- branch by 10 mm axial feed and 37.5 MPa internal pressure

4.5.2 X branch hydro forming

Simulation has been carried out for the same dimension of an X branch model as has previously carried out for T branch. Loading condition and boundary constraints have been kept unchanged. Taking symmetry advantage one eight of the model has been simulated. Figure 4.15 presents the one eighth of the X branch FEA model. The total solution completed by 4 msec in 19 sub steps. After a time of 2.6 msec in 13 sub steps, the maximum equivalent von mises stress was 493 MPa. After this time the von mises stress in the X branch exceeds the ultimate stresses of the materials. It was assumed that after this time the materials would fail so all results after this time have been ignored. Figure 4.16 depicts the deformed tube at 2.6 msec and 13 sub steps into X branch products. It is noticeable that maximum branch height is 3.61 mm which is greater than the previous T branch forming. Research reveals that for the same conditions applied on both T and X branch hydroforming, deformation is greater in X branch products than in T branch products. This was due to stretching the materials bi-axially in case of X branch.

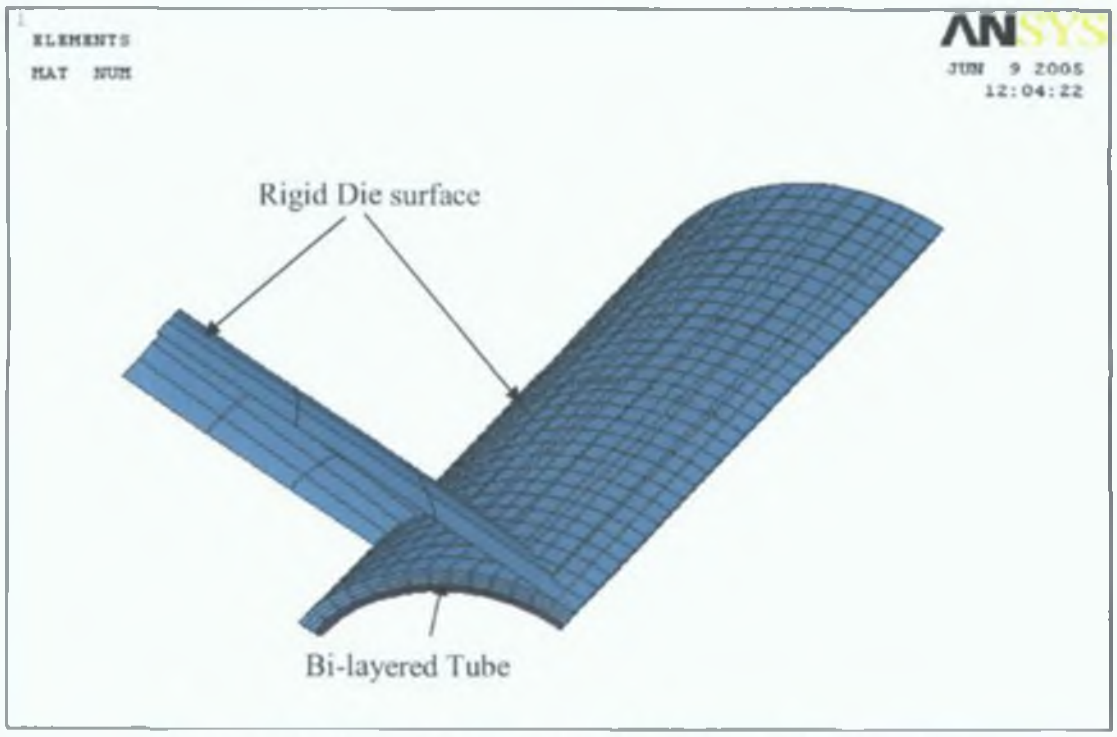

Figure 4.15.: One eight symmetry of the X branch FEA model

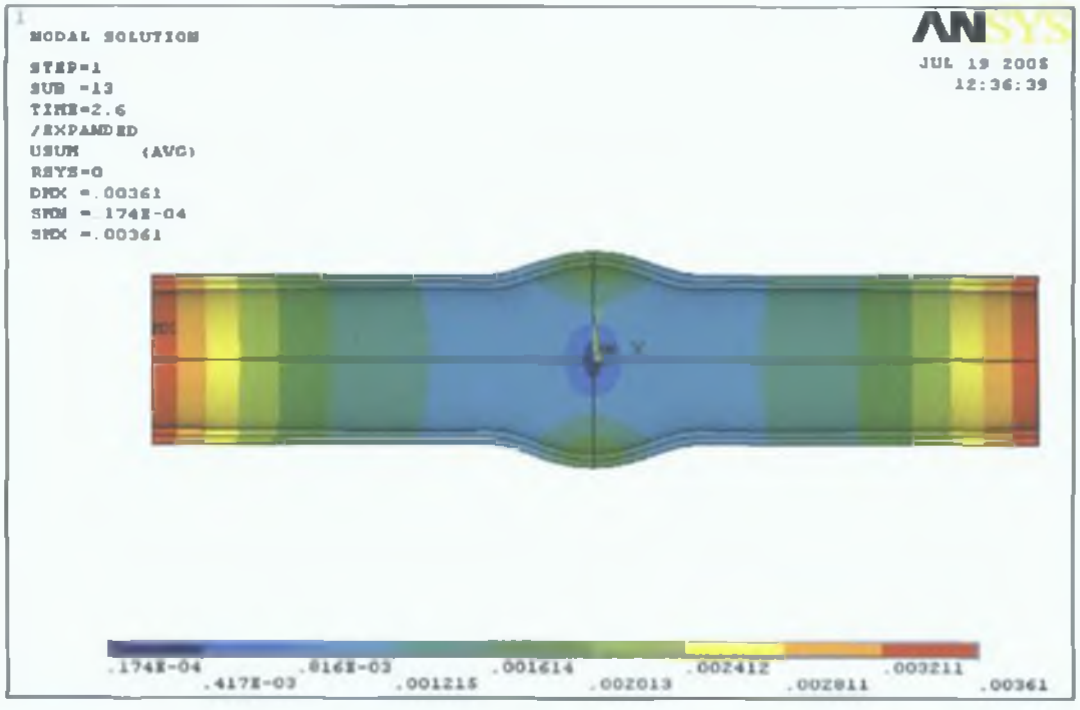

Figure 4.16.: Maximum developed branch height by hydroforming process for 10 mm Axial feed and 37.5 MPa internal pressures, X-branch forming

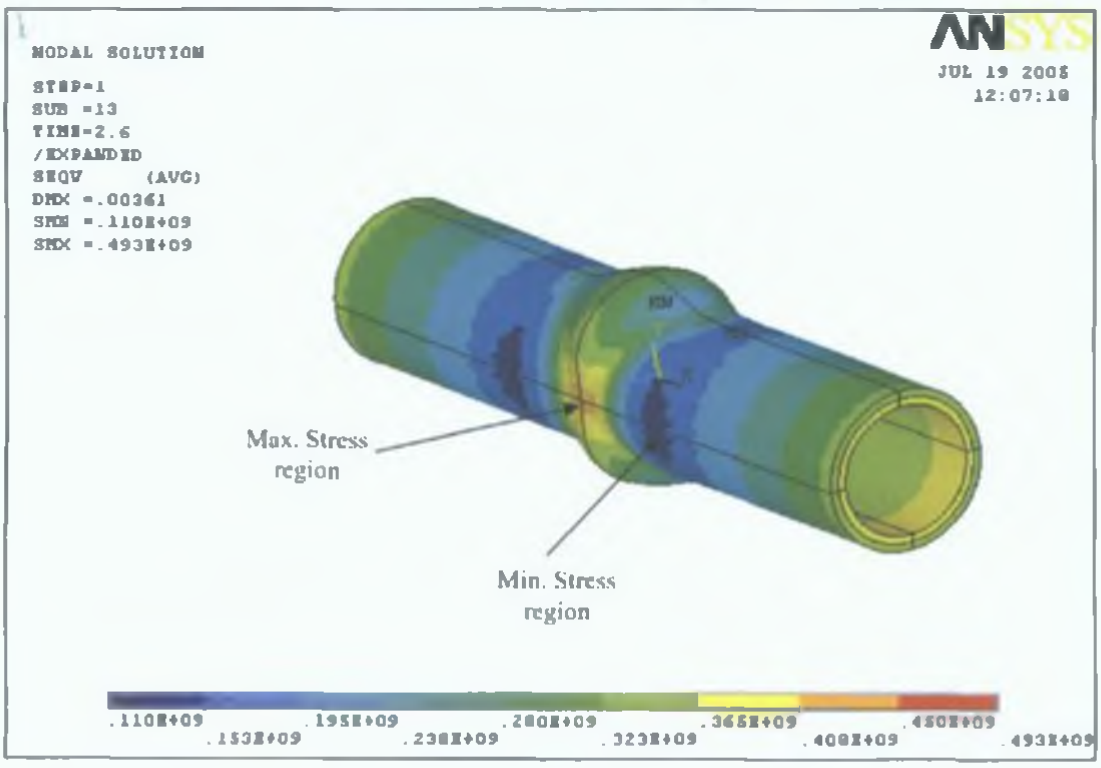

Figure 4.16.: Von Mises stress distribution over the simulated X-branch by hydro forming process for 10 mm Axial feed and 37.5 MPa internal pressure

In the case of the X branch, the internal pressure acts on both sides towards the branch hole of the die, while in the case of T branch it acts on one side, other side is neutralised by the reaction force of the die surface which results in less branch height. Figure 4.16 is depicting von mises stress distribution over the simulated X branch. It is noticeable that the maximum stress region is around the bottom of the formed branch which has located at the same region as it was in the T branch simulation. Stress was distributed uniformly over the top area of the branch. Figure 4.17 shows the stresses distribution over the top central node of the branch. From this figure it can be stated that the equivalent stress is well below the ultimate stress over the total simulation time. Elastic region in X branch is shorter than in T branch simulation. It can be noticed that after a time of 0.8 msecond, the central region has started to deform and the deformation has increased up to the end of the solutions. Figure 4.18 describes stress distribution over the top central node of the internal tube. It can be noticed that the von mises stress was higher than other type of stresses but its value was well below the materials ultimate stress.

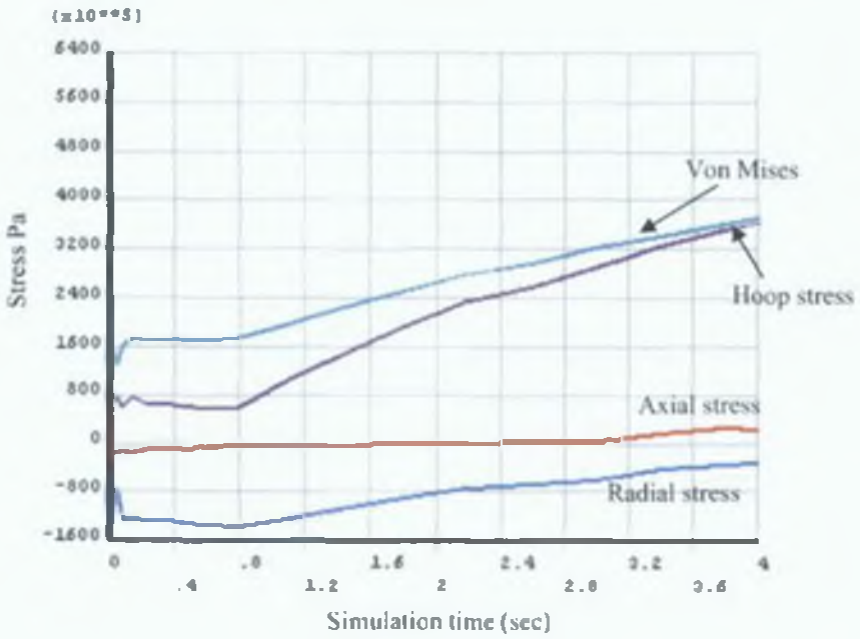

Figure 4.17.: Development of stresses over the top central node for outer layered tube of the simulated X branch by 10 mm axial feed and 37.5 MPa internal pressure

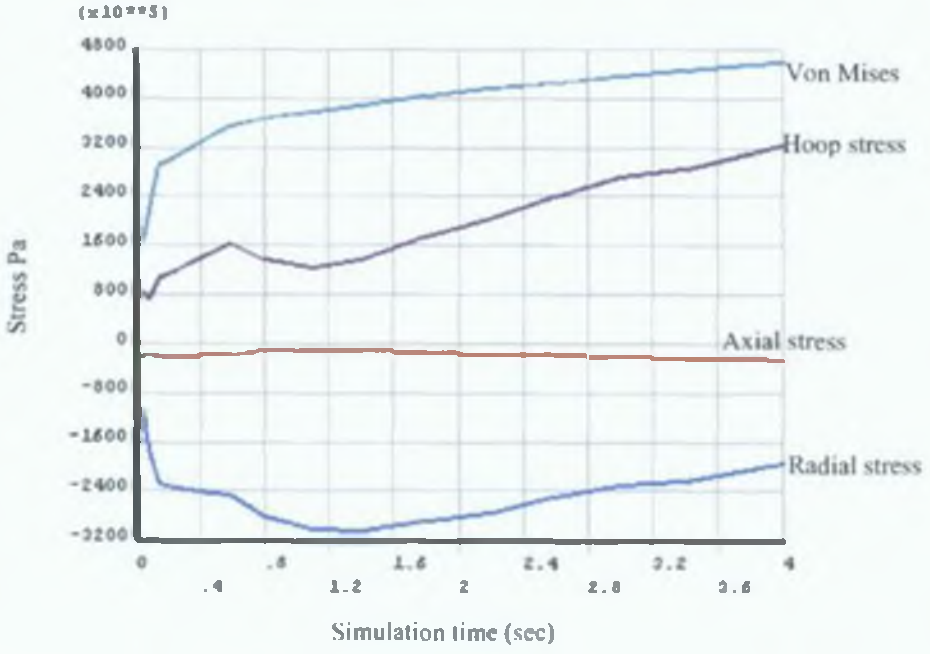

Figure 4.18.: Development of stresses over the top central node for internal tube of the simulated X branch by 10 mm axial feed and 37.5 MPa internal pressure

4.6 Failure Analysis

The main purpose of the hydroforming process simulation is to get the maximum formed branch for a certain loading conditions. In order to get the maximum forming height the load path should be in a controlled manner. The main failure types of the hydroforming process which involves both axial feed and internal pressure are wrinkling, buckling or bursting. Due to an excessive axial feed in comparison to the internal pressure the tube would fail by buckling or wrinkling. Alternatively, if the pressure is too high with respect to axial feed there would be a chance of bursting the tube. Thus the forming load has to be adjusted properly in order to obtain a successful formed component with the hydroforming process.

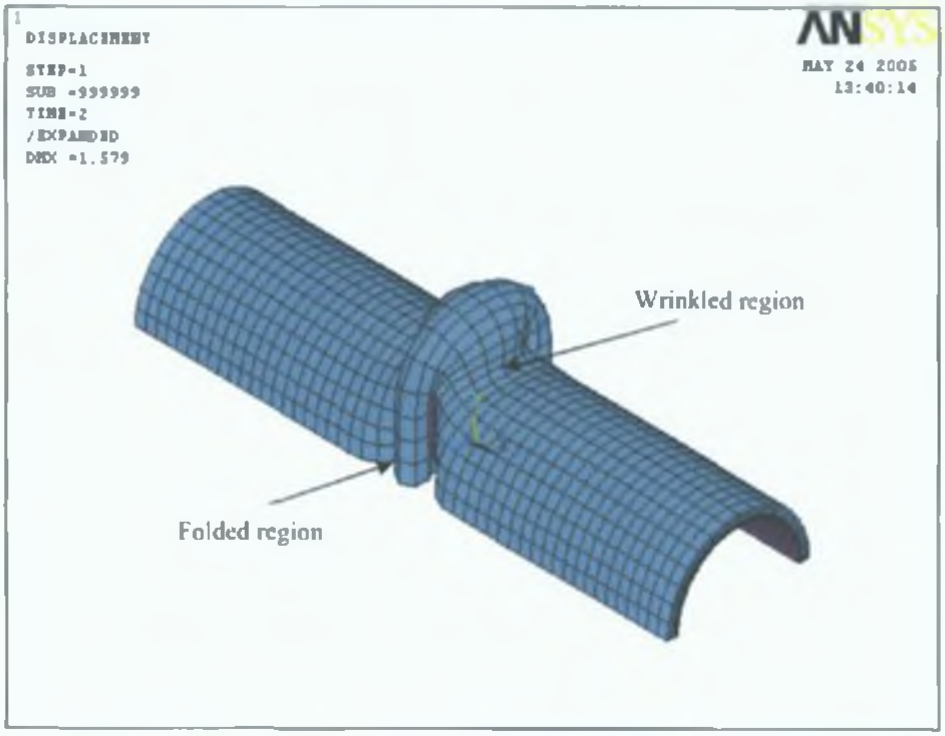

Figure 4.19.: Wrinkling and folding failure occurred due to excess axial feed during hydroforming process

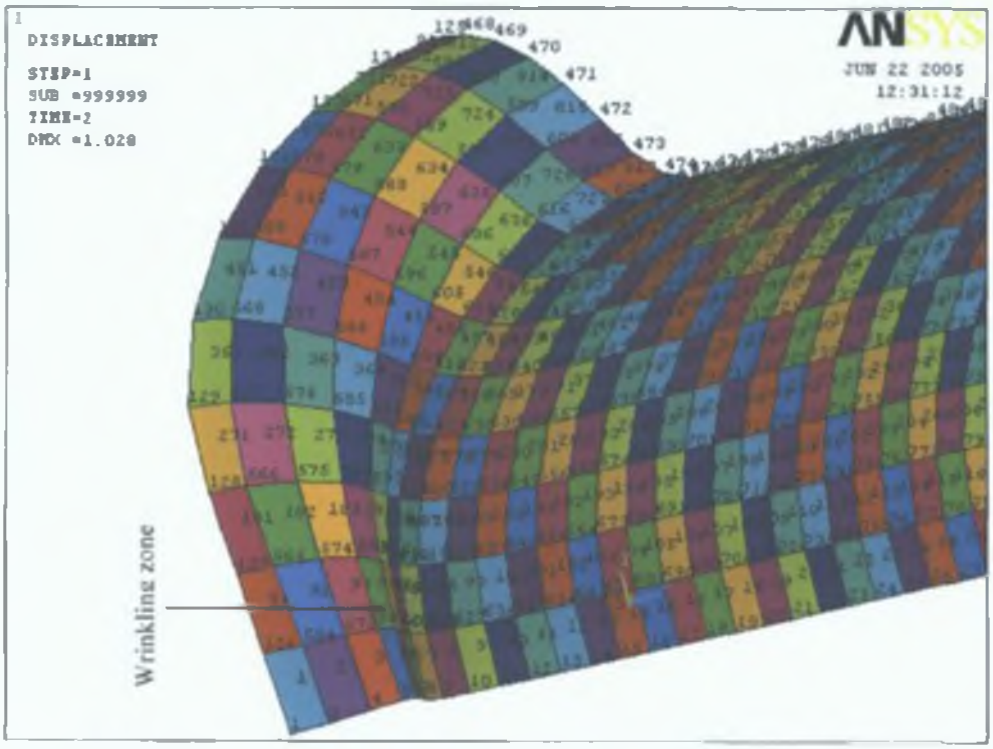

Figure 4.20.: wrinkle formed in finite element model with element number

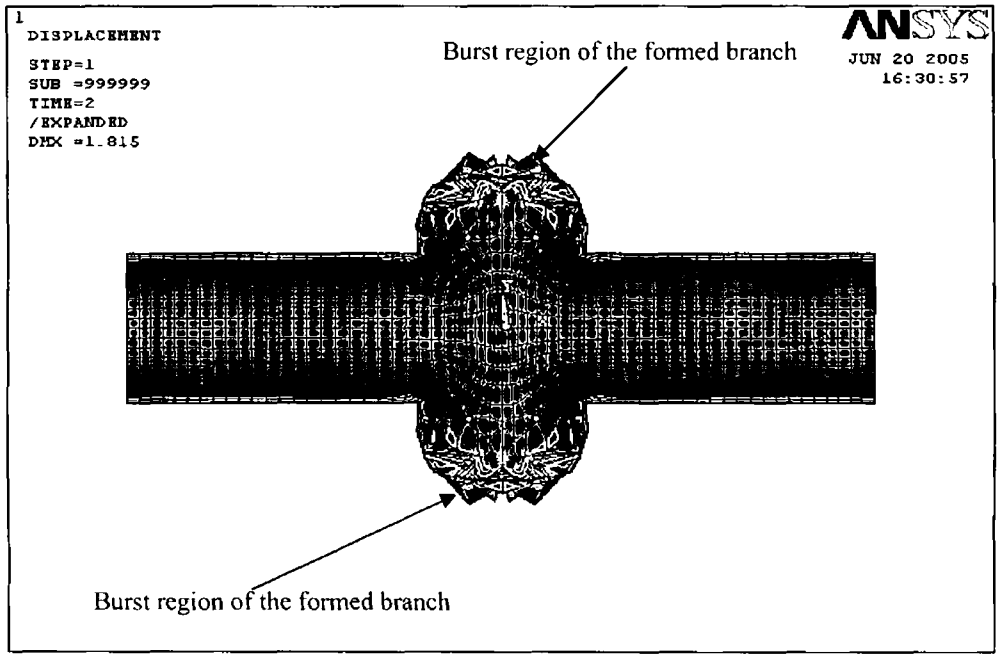

Figure 4.21.: Bursting failure due to excessive internal pressure during X branch hydroforming process

Simulation which is depicted in figure 4.19 has been carried out by applying an internal pressure of 37.5 MPa and an axial feed of 40 mm. The axial feed was in excessive compared to the internal pressure; as a result the tube was folded and wrinkled. If the wrinkle occurs on the tube it would result with a buckling as it can be seen in the figure 4.20 and the element subjected to wrinkle would be strained differently on the outer and inner surfaces respectively. As mentioned [43] the velocity of the element in the normal direction can also be used to assess whether the wrinkle is desired or not, that is when the material is already in contact with the die, or whether the wrinkle is with unstable folding due to excess axial feed or due to low hydroforming pressure. Because of the instability, a region of unstable folding or wrinkling has a much higher normal velocity than the free forming region due to the internal pressure. In a hydroforming process which involves end axial feed and internal pressure, it is desired that the end axial feed over the process time should be as high as possible to allow more material to be fed into the forming zone, thereby decreasing the chance of failure due to excess wall thinning or bursting. This excess material pushed into the deforming zone helps in maintaining wall thickness near

the highly strained area within the desired limits. The value of actual axial feeding in the process is limited by the occurrence of wrinkles or buckling. On the other hand excess material pushed into the forming zone may result into either buckling or excess wall thickening in certain zone. Failure as demonstrated in figure 4.21 is busting due to excess of the internal pressure in comparison to the axial feed. This simulation has been carried out for 10 mm axial feed and 150 MPa internal pressure. Top central area of the simulated branch became thinning due to excess of the internal pressure, at the end hoop stress rose to beyond the ultimate stress which has resulted with the burst of the tube.

4.7 Experimental procedure

4.7.1 The Hydroforming Machine

The hydro bulge forming machine in DCU is capable of producing a maximum internal hydrostatic pressure of 41.7 MPa. This value was obtained through previous tests carried out on the machine on copper specimens. The machine can produce a maximum axial force on a tube of 150Bar because of the limited capacity of the motor and intensifier of internal pressure. This force will be represented as an axial displacement on ANSYS. An image of the hydro bulge forming machine used in DCU can be examined in figure 4.22. The hydro bulge forming machine is programmed using a lab view program. The process of automation and procedure of collecting data by Lab View has not been discussed in this research work. This method of operating the machine allows the user to input more controlled loading patterns into the hydro bulge forming machine. The operation of the hydro bulge forming machine is discussed in chapter1.Three different tests were carried out on the multi-layer material using the hydroforming machine. All the experimental tests were carried out with a maximum internal pressure of 37.5 MPa.

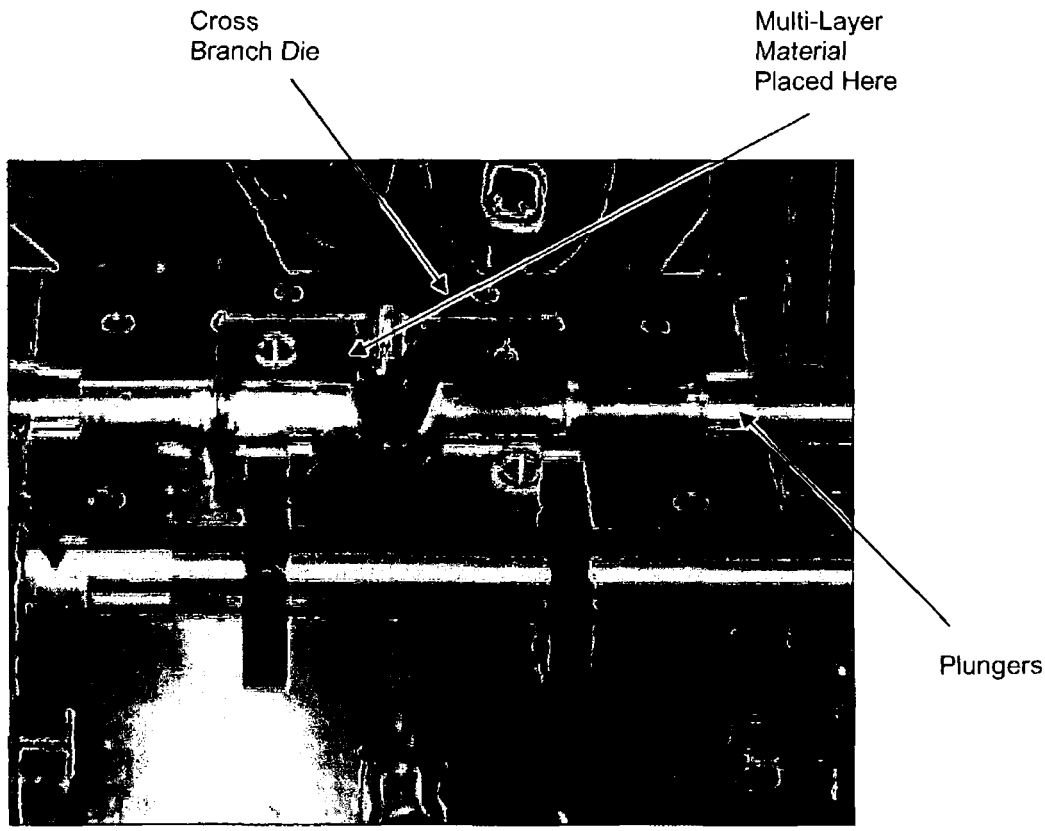

Figure 4.22.: The Hydroforming Machine

4.7.2 Experimental Test one; Internal Pressure 37.5 MPa, Axial Force 7 MPa

To verify the analytical results three experimental tests were carried out with different boundary condition. The results are presented in the following section. The first test that was carried out was done so with the highest possible internal pressure along with a low axial force. The maximum capacity of internal pressure in the bulge forming machine is 41.7 MPa. But when the experiment was caring out the machine was only capable of reaching a maximum internal pressure of 37.5 MPa internal pressure because of the limited capacity of the motor, thus all the experiment has been carried out for 37.5 MPa internal pressure. The internal pressure was adjusted using the appropriate valve at the back of the machine and the axial force was also adjusted using another valve on the

machine. The bulge forming machine was run using an appropriate Lab view program. Firstly the plungers came in contact with the multi layer tube; the hydraulic fluid was then passed into the specimen through the plungers. The internal pressure was allowed to build up slowly. Any air bubbles that were contained in the hydraulic fluid were released using a relief valve. Then the high internal pressure was applied to the multi layer material. Along with the high internal pressure the axial force was then applied to the ends of the multi layer tube. Figure 4.23 depicts the formed product by hydroforming machine for test one.

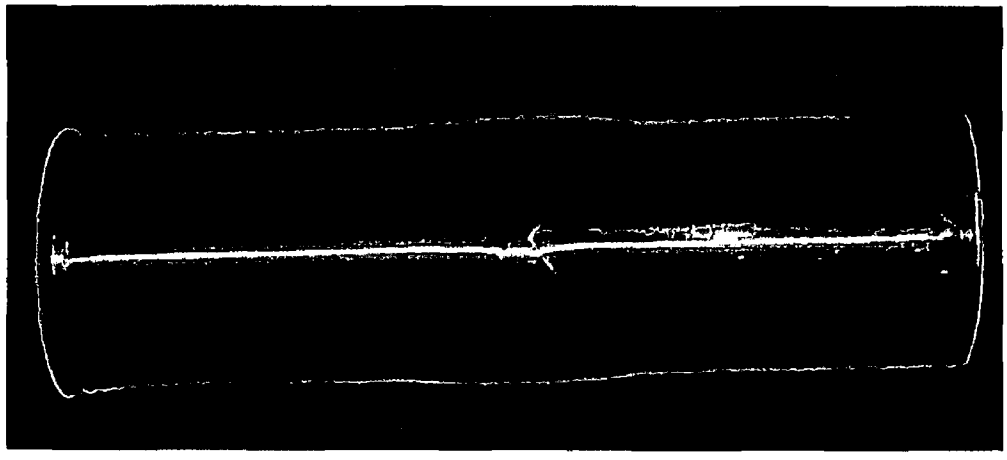

Figure 4.23.: Multi-layer Material Deformation at 37.5 MPa internal pressure and 7 MPa Axial Force

As it can be seen from Figure 4.23 that a little deformation occurred during the hydroforming process. This was due to two main factors, the wall thickness of the multi layer tube was too high (because commercial multi layered tube for the required thickness is not available in the market) and the internal pressure applied by the hydro forming machine wasn't high enough to cause a big deformation in the material. Figure 4.24 shows the loading pattern used on the hydro bulge forming machine. This loading pattern has been automated by LabView program with the bulge forming machine. The graph shows the increase of internal pressure and axial force with respect to time. The increase in displacement from 0 to 50 at the start of the process represents the plungers moving

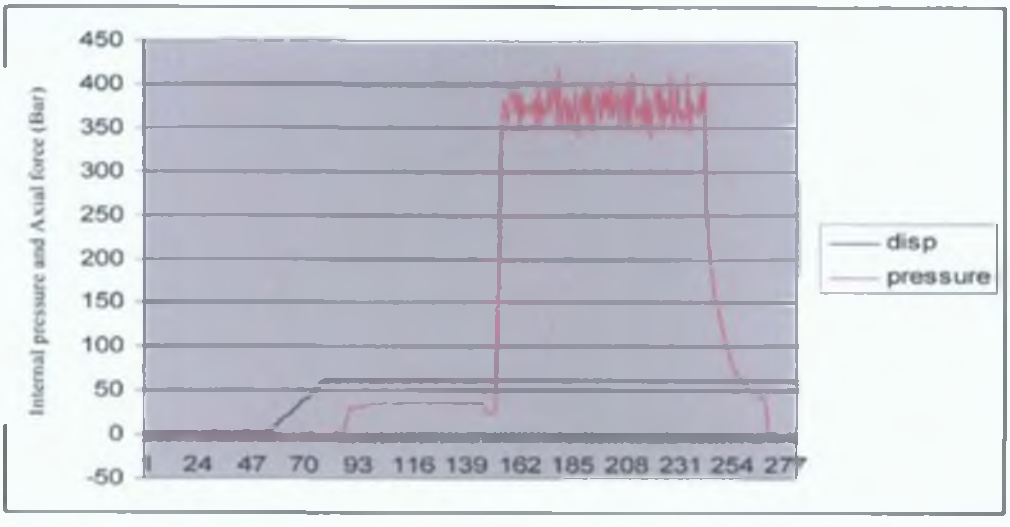

Figure 4.24.: Loading profile on the Hydro Bulge Forming Machine at 37.5 MPa internal Pressure and 7MPa axial Force

into make contact with the multi layer material. As the graph shows there is little displacement of the plungers after this point.

4.7.3 Experimental Test two; 37.5 MPa Internal Pressure, 12 MPa axial force

In this test the same procedure as test one was carried out. The axial force was increased to 120Bar or 12MPa. Figure 4.25 shows the deformation of the multi layer material after the hydro bulge forming process.

Figure 4.25.: Multi-layer Material Deformation at 37.5 MPa internal pressures and 12 MPa Axial Force

The axial force was increased to 120Bar (12 MPa). Figure 4.25 shows the deformation of the multi layer material after the hydro bulge forming process. From observing figure 4.25 it can be clearly seen that some more deformation occurs due to the increase in the axial force. Although the branch height is small, the presence of the bulge on the multi layer material proves that hydro bulge forming of the multi layer material is possible. The maximum bulge height was 5.36mm. The loading pattern used in this test can be seen in figure 4.26. The increase in displacement of the plungers can be clearly seen from the graph. The axial displacement was measured at 10mm in total.

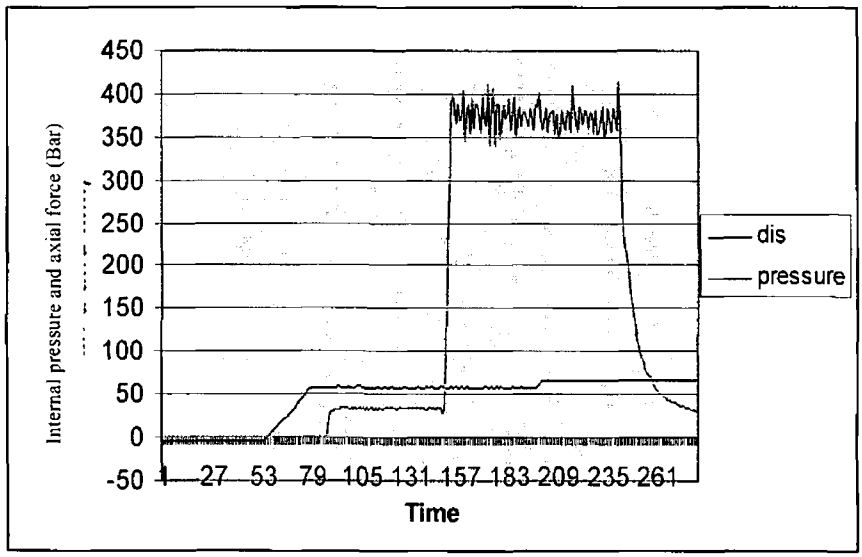

Figure 4.26.: Loading Pattern on the Hydro Bulge Forming Machine at 37.5MPa internal Pressure and axial Force of 12 MPa

4.7.4 Experimental Test three, 37.5 MPa internal Pressure, 15 MPa axial force

After the results obtained in test two it was assumed that an extra increase in the internal pressure might create a higher cross branch. The maximum axial force of 15 MPa was applied in test three along with the maximum internal pressure. The result of the higher axial force on the multi layer material can be seen in figure 4.27. It can be seen from

figure 4.27 that the multi layer material failed under a relatively high axial force. The multi layer material buckled under this condition, where the internal pressure was not high enough to force the material up into the deformation zone. The loading pattern for this test can be seen in figure 4.28. The point of failure is marked on the plot.

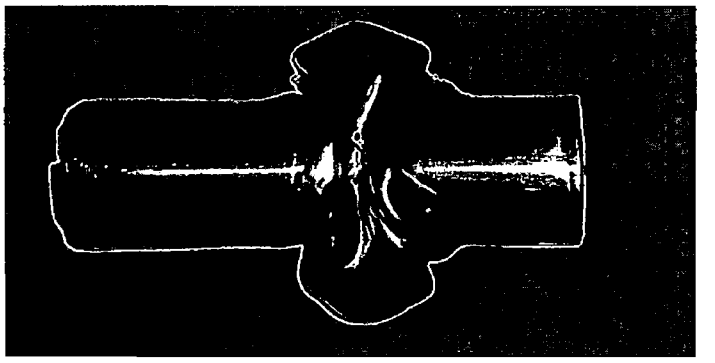

Figure 4.27: Multi-layer Material Deformation at 37.5 MPa internal pressure and 15 MPa Axial Force

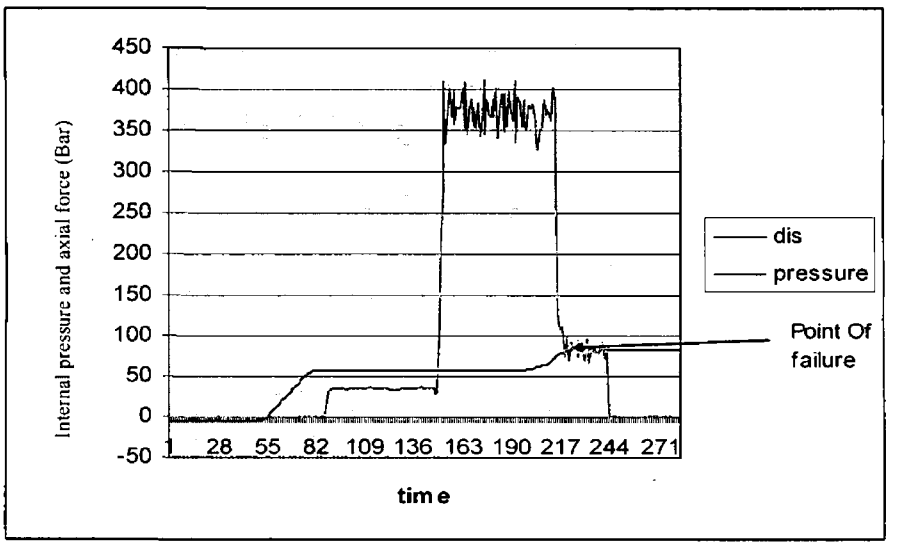

Figure 4.28.: Loading Pattern on the Hydro Bulge Forming Machine at 37.5 MPa internal Pressure and axial Force of 15 MPa

Failure occurred due to wrinkling, buckling and at the last stage folding of the multi layer tube due to a relatively low internal pressure. From these three experimental tests it can be concluded that application of sufficient internal pressure is the most important by hydroforming process in order to produce a successful component. These tests have been carried out according to the boundary condition and loading constraints that were applied in the simulation in the previous section. The obtained results from these experiments are very similar to the analytical results; on the other hand it is clear from these tests that the multi layered tube hydroforming is possible by applying the correct load path and boundary constraints. Validation and comparison between experimental and simulated results have been discussed in the next section of this chapter.

4.8 Comparison and Validation of the Simulation Results

4.8.1 Validation for test one

In order to validate the simulation of multilayered tube by hydro forming, several comparison has been made between the experimental and analytical results. The comparison between the simulation results and the practical results from first test can be observed in figure 4.29 below. The upper part of the figure represents the simulated result carried out by 1 mm axial feed and 37.5 MPa internal pressure. The lower part of the figure has been formed by applying the same axial feed and internal pressure in the hydroforming

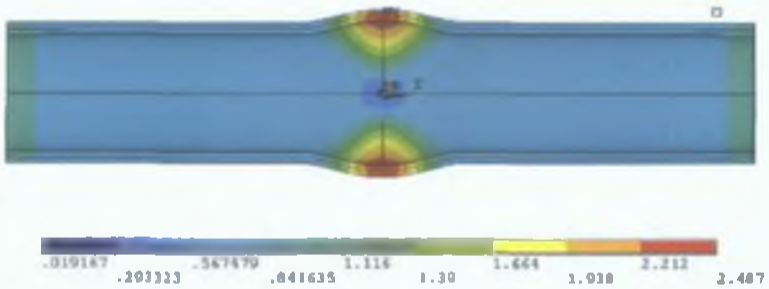

Figure 4.29.: Comparison between simulation and actual results from test one

machine. Figure 4.29 shows that both results have a very similar profile. The maximum branch height in the simulation was 2.487mm and the actual branch height formed using the bulge forming machine is approximately 1mm. This difference between the analytical and experimental test results could be the high friction between the die and the multi-layered tube, relatively low axial feed and insufficient internal pressure.

4.8.2 Validation for test two

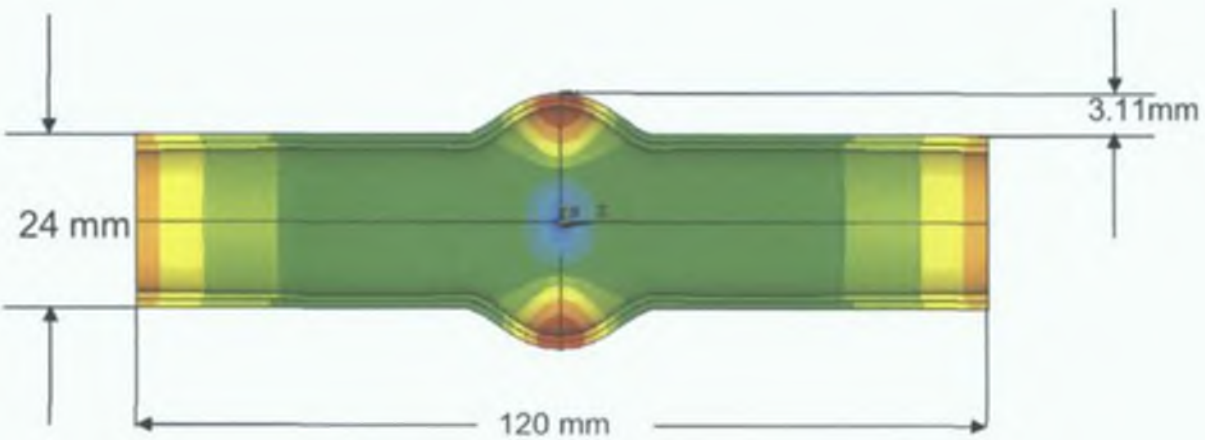

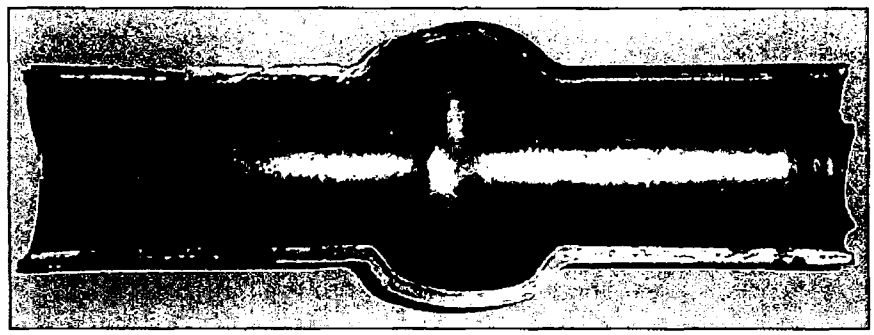

Figure 4.30.: Comparison between simulation and actual results from test two

A further simulation has been carried out in order to compare between the experimental and analytical results. This simulation also carried out for 37.5 MPa internal pressure and 10 mm axial displacement. The test in the hydro bulge forming machine was experimented by applying the same boundary conditions. Figure 4.30 presents the simulated and the experimented form branch. The upper part of the figure is the simulated branch and the lower one is experimented. Again figure 4.30 verifies that both the simulated results and the practical results are very similar apparently. The maximum branch height in the simulated result is 3.11 mm and the branch height obtained from the hydro bulge forming machine is 3.25 mm.

4.8.3 Validation for test three

The comparison between the simulation results and the practical results from the third test can be observed in figure 4.31. The results of this test was very hard to match as in the practical tests the multi layer material failed. To represent this failure in Ansys is difficult as if a failure of the material occurs in Ansys no results can be obtained for the specimen. The displacement of the branch, although it's much buckled was approximately 17mm. The actual displacement of the failed specimen was proximally 15 mm. Therefore it can be seen that both the practical and simulation results were in good agreement. It can be seen that a large amount of buckling occurs and both materials were under very high stress. The buckling occurred as there wasn't a high enough internal pressure to match the high axial displacement or axial force.

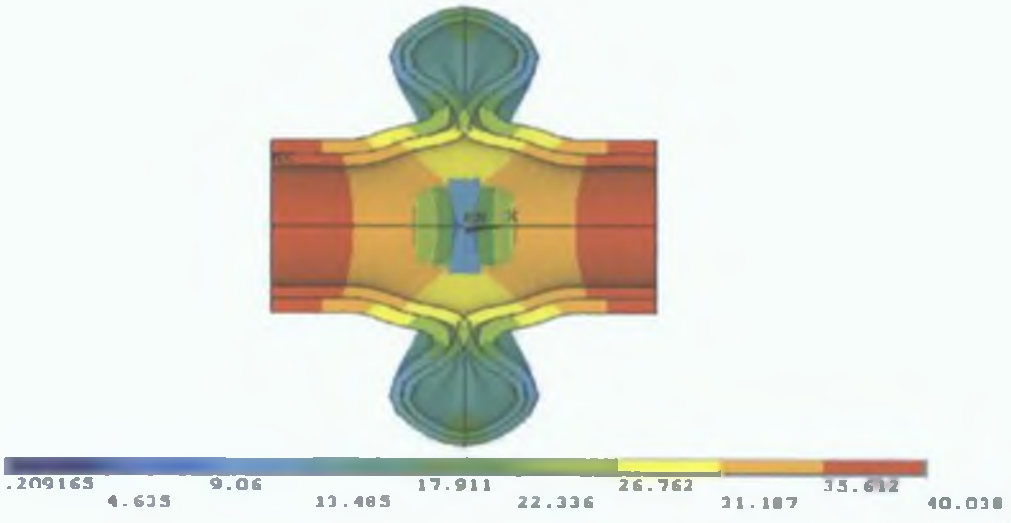

Figure 4.31.: Comparison between simulation and actual results from test three

4.9 Summary of the chapter

It can be concluded from this chapter that hydroforming process validates both experimental and analytical. The best result has been found in test two. Both simulation and experimental results are very close on the basis of deformation profile and the value of the branch height. The practical results obtained using the hydro bulge forming machine were quite good. It is evident from these results that the slight difference between the analytical and experimental results related to the initial forming, in other words experimentally the deformation was very low at the beginning, then this deformation would increased while in the analytical model the deformation would follow the analyzing algorithm without considering any difficulty for the initial deformation. As it can be noticed form [45] that the experimental and analytical results are in good agreement at the final stage of the deformation. A step by step FEA procedures have been discussed for the multi layered tube hydroforming process. Modelling, boundary condition and solution, all these steps have been analysed by using finite element package ANSYS. It is also possible and even easier to analyze by using LS-DYNA explicit finite element codes.

CHAPTER FIVE

Further Simulations of X and T branches by Different Loading

5.1 Introduction

This chapter presents a number of simulations both X and T branches in different loading condition and constraints by hydroforming process. Actually all the simulations have been carried out for combined axial feed and internal pressure. Von mises and hoop stress distributions have been presented for each case. The best condition has been selected and discussed. These simulated models aim to define the forming conditions to form the X and T branches with the proper height without any defect.

5.2 Cross (X) branch hydro forming at different loading conditions

5.2.1 10 mm axial feed and 50 MPa internal Pressure

The model has been built with the same element and materials as stated in chapter four with different dimensions. In this case the thickness of internal tube has been considered as half of the external tube thickness (0.5 mm internal tube thickness and 1.00 mm tube external). Both contact pair have been created as identified in the previous model. Load functions have been defined for 2 second and the length has been assigned as in centimeter. During analyzing one eight of the whole tube has been modeled due to considering the symmetry advantages. To complete the solution it took 14 sub steps in 2 seconds. But after 0.6275 second the von mises stress exceeded the material ultimate stress for that reason all results after this time have been ignored and up to this time 7 sub steps completed. Figure 5.1 shows the results at this stage, it is seen that the maximum von mises stress developed at this time 500 MPa which is well below the ultimate stress. This figure also demonstrates the location of the maximum stress is the bottom region of the formed branch. Over the area of the tube and branch the stress distribution is moderately uniform. Figure 5.2 presents the material displacement in Y

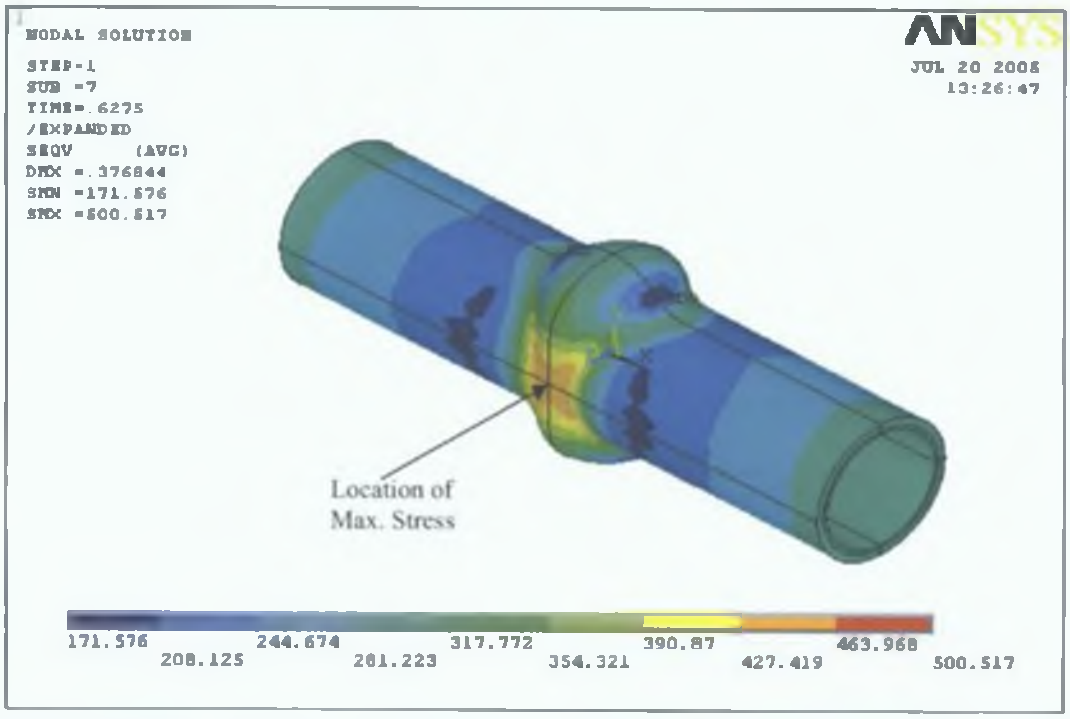

Figure 5.1.: Von-mises stress distribution over the simulated X branch by 10mm axial feed and 50 MPa internal pressure

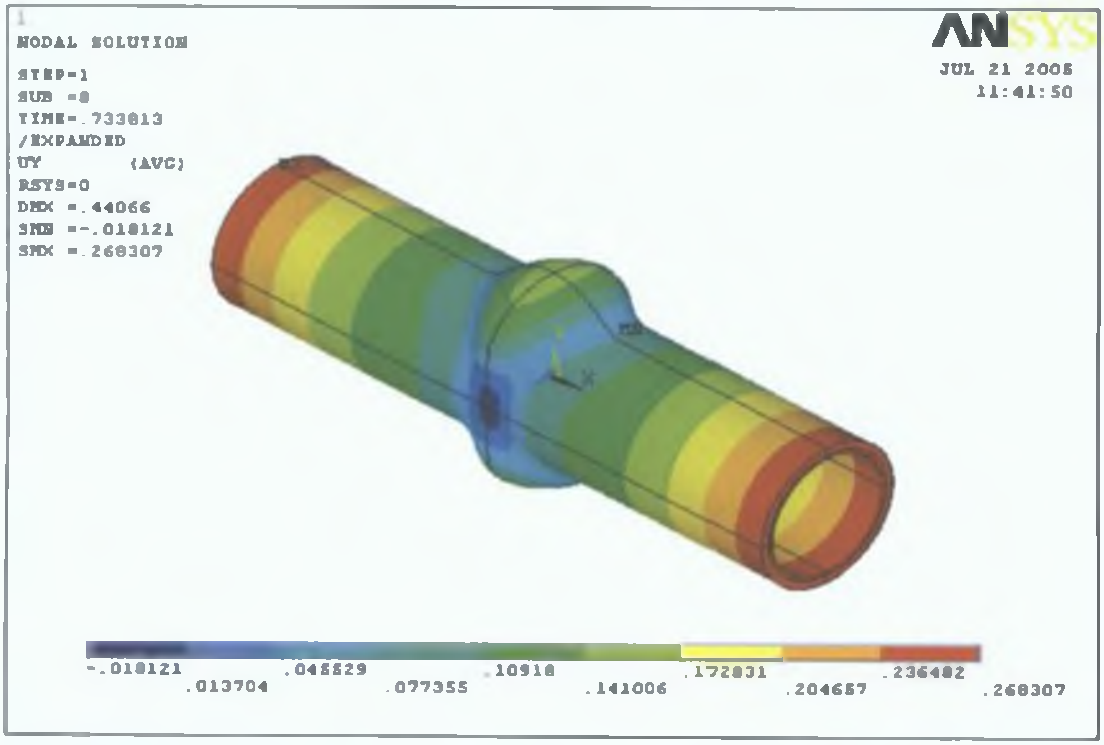

Figure 5.2.: Maximum branch height of the simulated X branch by 10 mm axial feed and 50 MPa internal pressure

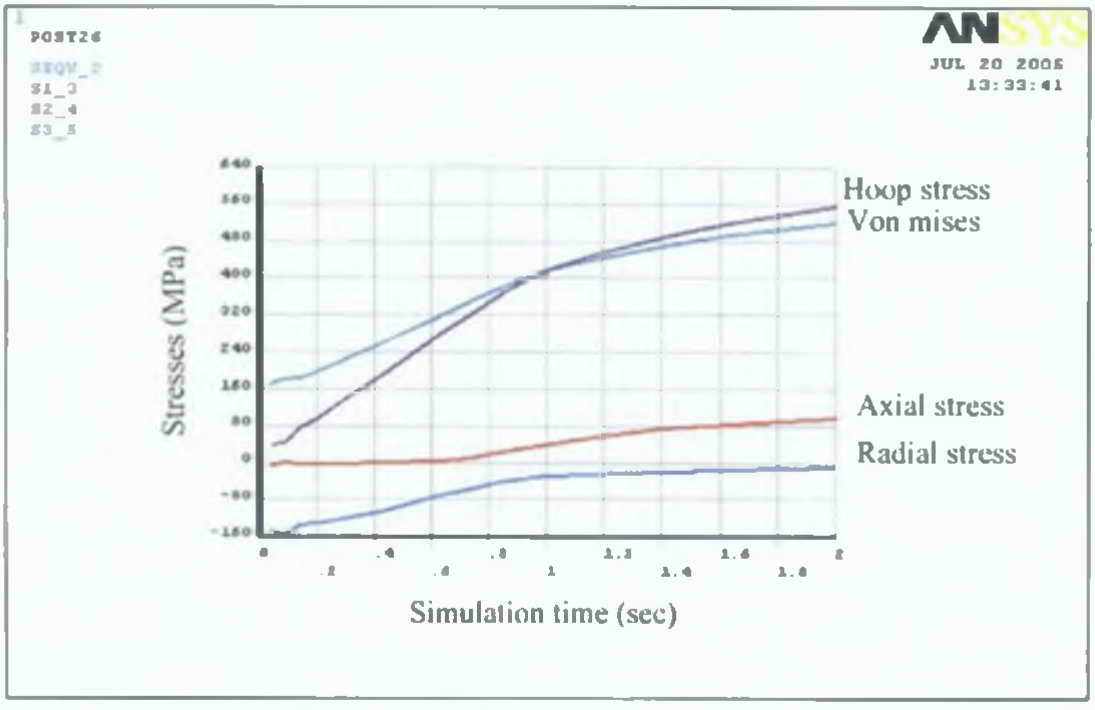

Figure 5.3.: Stresses distribution over the top central node on the external tube of the simulated X branch by 10 mm axial feed and 50 MPa internal pressure

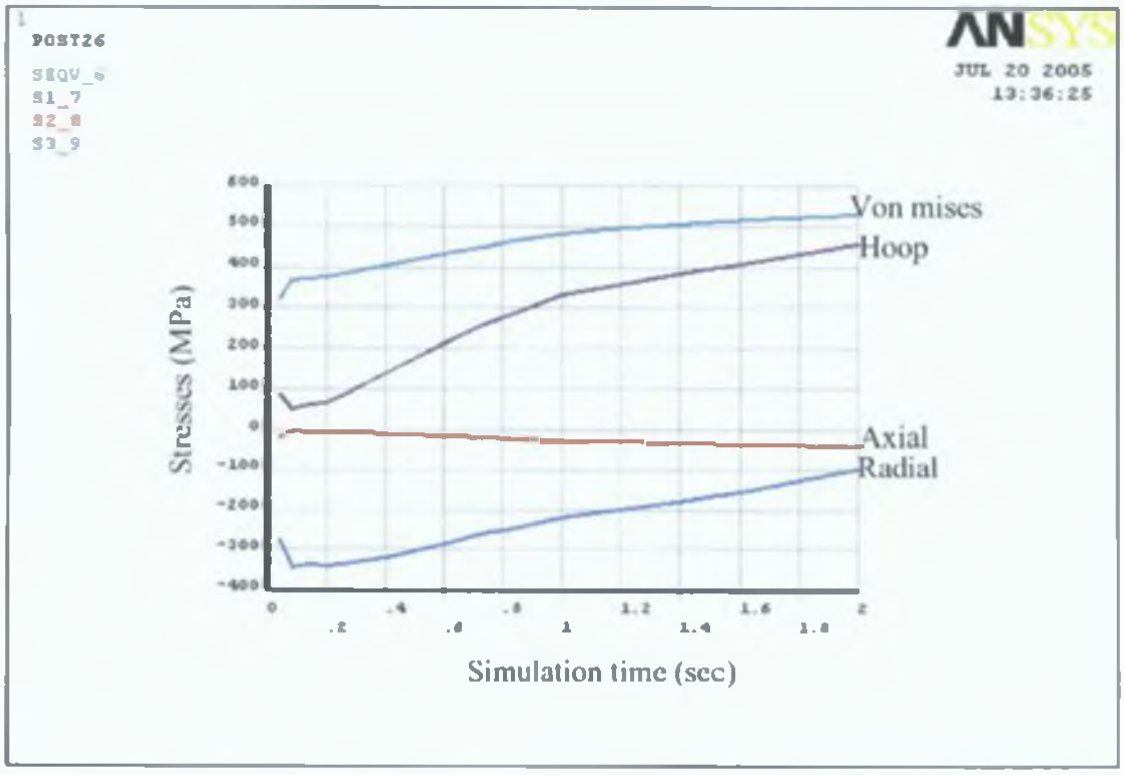

Figure 5.4.: Stresses distribution over the top central node on the internal tube of the simulated X branch by 10 mm axial feed and 50 MPa internal pressure

direction in the global co-ordinate system. It is obvious that the bulge height is about 0.26 cm. It can be noticed that the material flow was not uniform, there were some thinning and thickening exists over the form products. In this research the thinning and thickening of material has not been analyzed. Figure 5.3 depicts the stresses distribution over the top central node of the simulated X branch of the outer tube. At the top central region maximum von mises stress was 490 MPa which is well below the ultimate stress. Hoop stress is little bit higher than equivalent stress but below the ultimate stress radial stress is compressive over the simulation time. It is also clear from the graph that elastic region is very short. Figure 5.4 is describing the stress distribution over the top central node of the internal tube. It can be that in the internal tube equivalent stress is more dominant than the external tube during the course of simulation time. All other stresses are following usual convention.

5.2.2 10 mm axial feed and 60 MPa internal pressure

Simulation has been carried out for the previous model with different load constraint. In this case the axial feed was the same but the internal pressure was 60 MPa. The solution was completed after 14 sub steps in 2 seconds. In this case after a time of 0.6875 seconds the von mises stress developed in the tube exceeds the ultimate stress of the materials. Maximum von mises stress was between 501 to 543 MPa after a time of 0.6875 second. The maximum ultimate stress for the outer tube materials was 540 MPa, for this reason it has been considered that at this step the solution is within the safe limit just before the failure of the materials. Figure 5.5 depicts von mises stress distribution over the simulated X branch. The location of the maximum stress is at the same region as the previous solution. Figure 5.6 demonstrates the deformation condition of the X branch for this condition. Stress distribution can be seen in the figure 5.7 over the simulation time for the external tube of the simulated X branch. It is evident that hoop stress is more dominant after a certain time during the solution and at the end of the solution hoop stress exceeds the ultimate stress. Stress distribution for the internal tube can be seen in the figure 5.8, the von mises stress is more dominant over the simulation time up to the end of the solution.

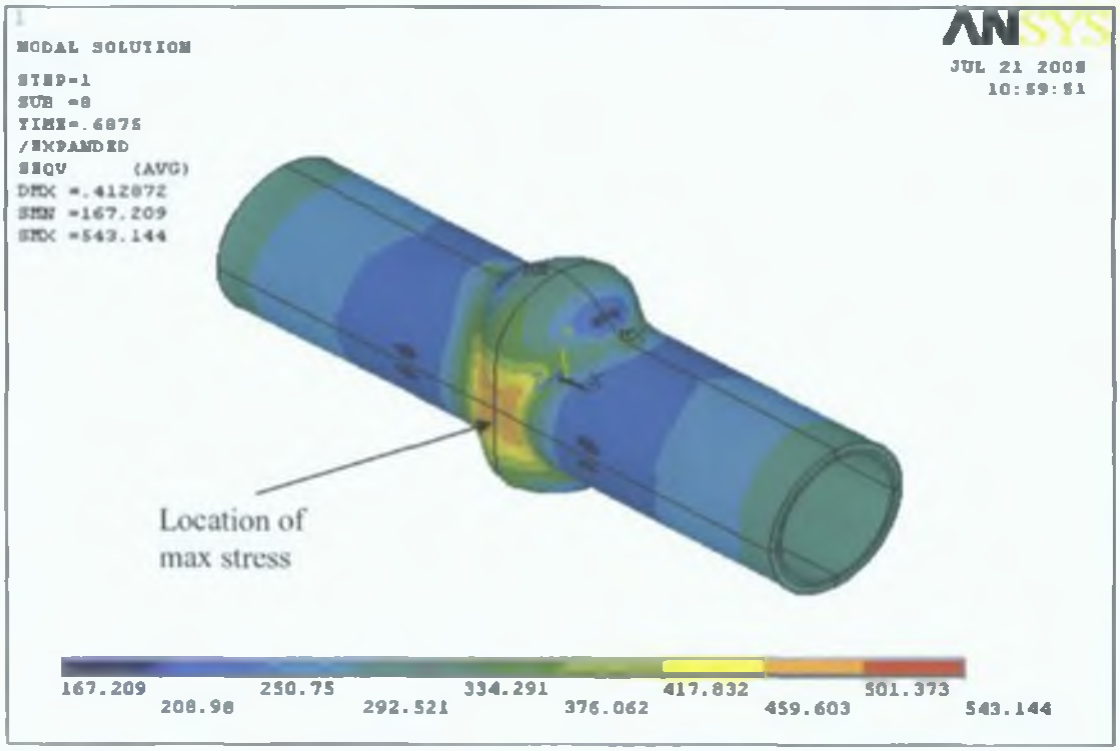

Figure 5.5.: Von-mises stress distribution over the simulated 'X' branch by 10mm axial feed and 60 MPa internal pressure

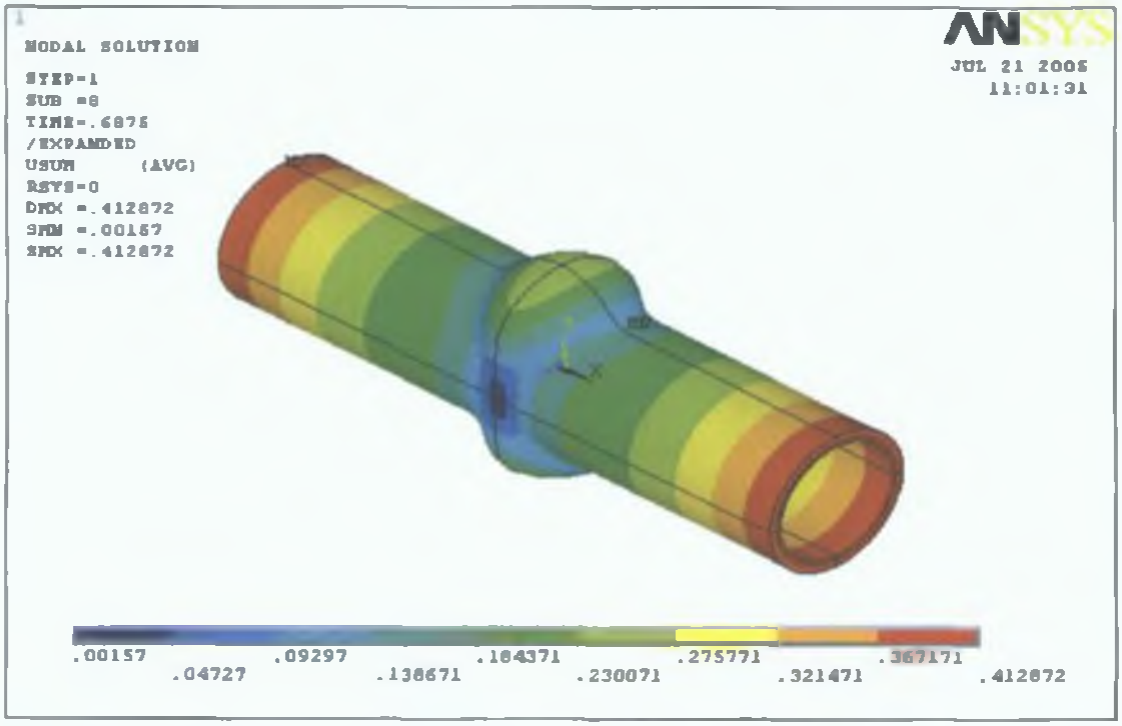

Figure 5.6.: Maximum branch height of the simulated X branch by 10 mm axial feed and 60 MPa internal pressure

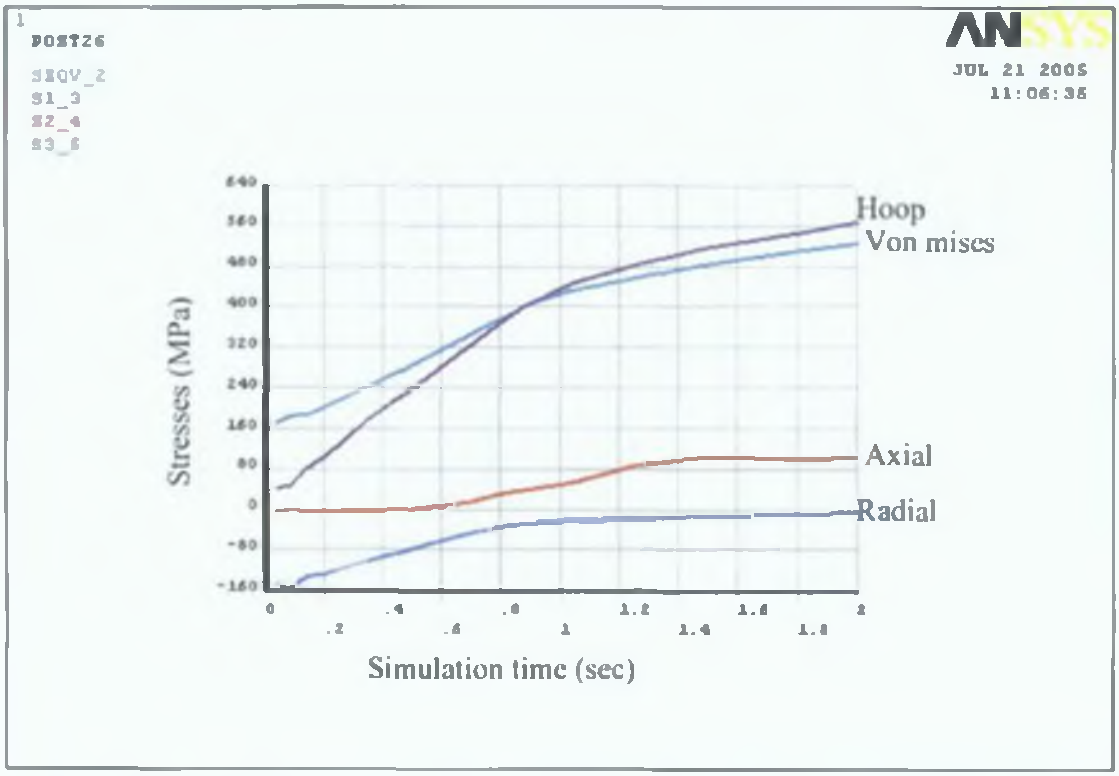

Figure 5.7.: Development of stresses on top central node of the external tube of the simulated X branch by 10 mm axial feed and 60 MPa pressure load

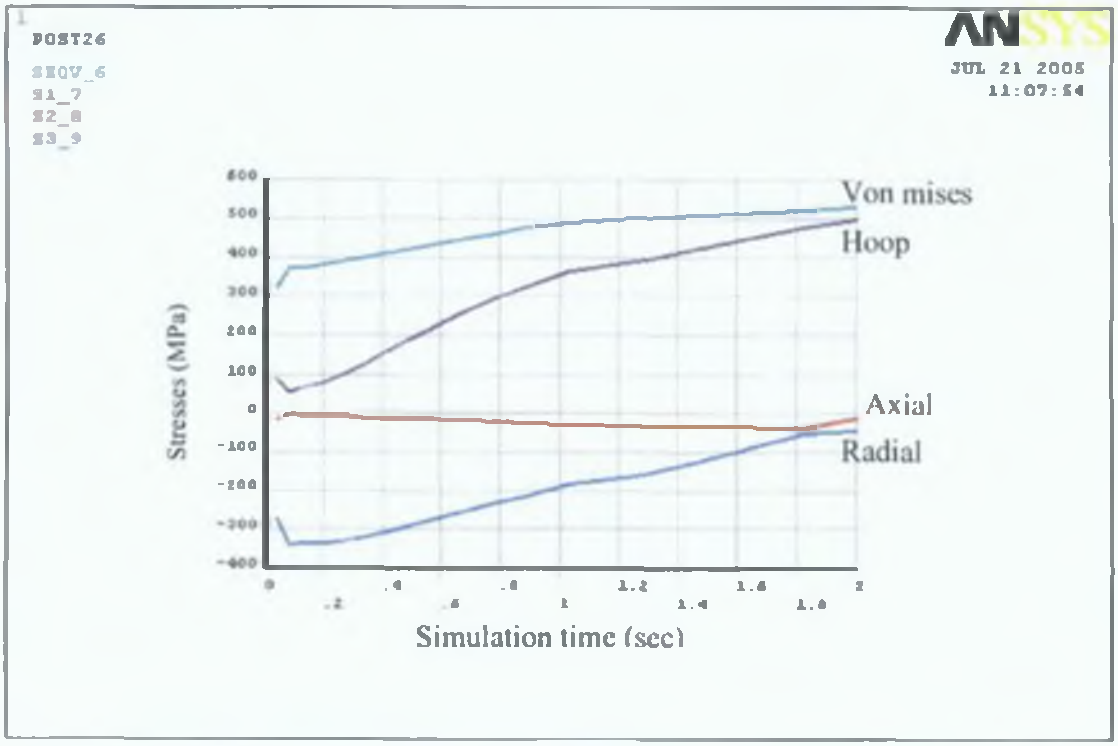

Figure 5.8.: Stresses distribution over the top central node on the internal tube of the simulated 'X' branch by 10 mm axial feed and 60 MPa internal pressure

5.2.3 10 mm axial feed and 70 MPa internal pressure

The same model was analyzed with different boundary conditions. In this case internal pressure has been increased to 70 MPa. The solution was completed within 15 total sub steps. But at a time of 0.717 seconds after 8 sub steps the solution has been assigned as completed because after this time the equivalent stress exceeds the ultimate stress of the materials. Figure 5.9 shows the von mises stress distribution of the simulated X branch at a time of 0.717 seconds. The maximum stress developed in this case is about 500 MPa and the location of the maximum stress is near the bottom of the simulated branch. Figure 5.10 describes the deformation situation of the simulated branch after 8 sub steps. The maximum deformation was about 0.4311 cm and maximum bulge height was found 3.11 cm. which is little less than the deformation.

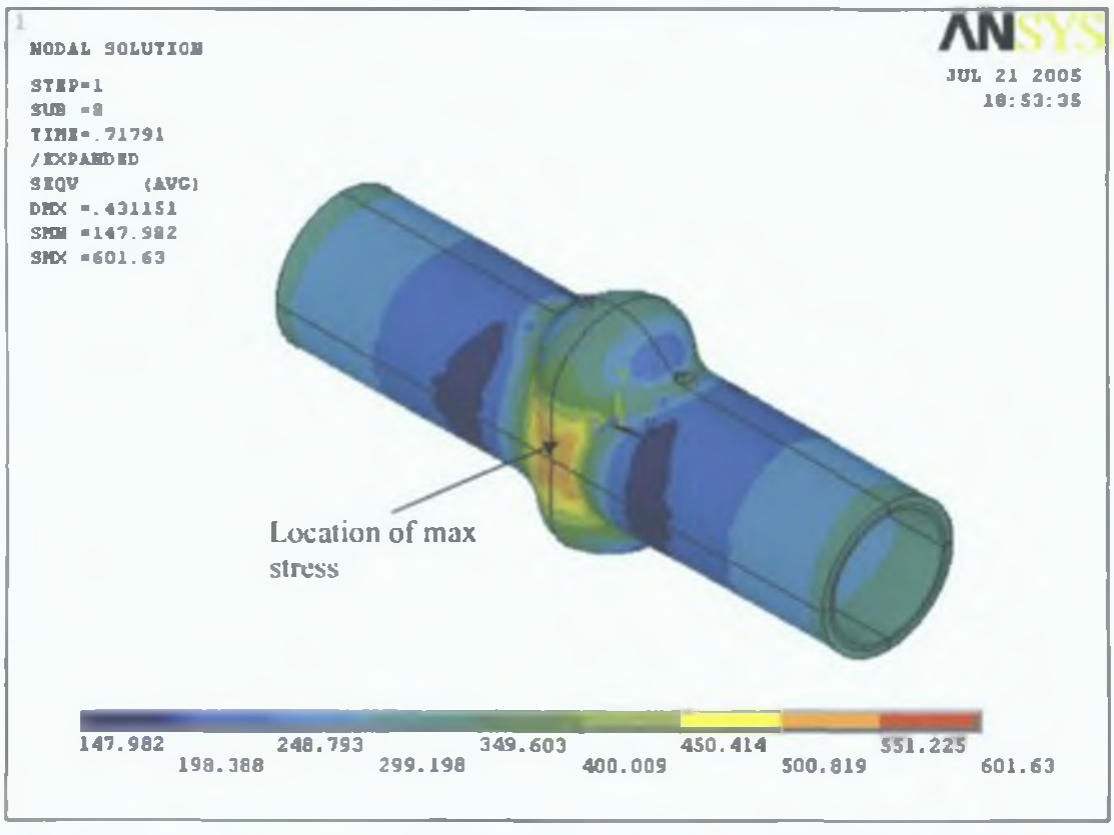

Figure 5.9.: Von-mises stress distribution over the simulated X branch by 10mm axial feed and 60 MPa internal pressure

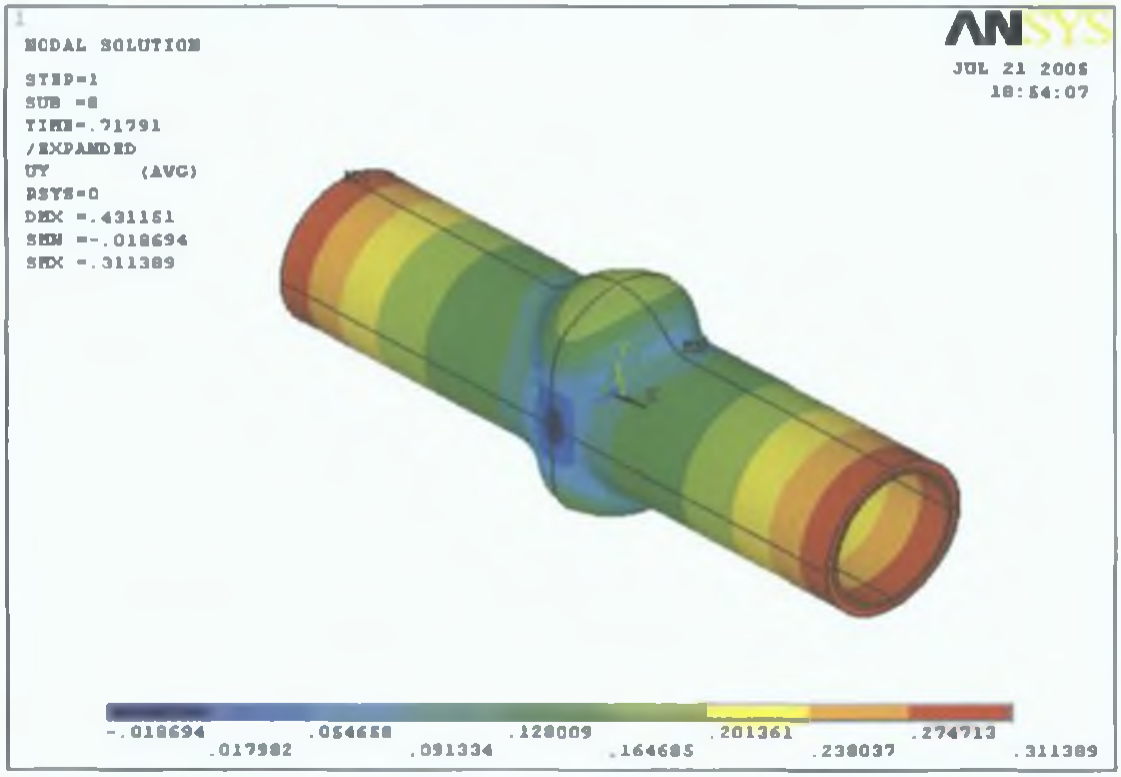

Figure 5.10.: Maximum branch height of the simulated X branch by 10 mm axial feed and 70MPa internal pressure

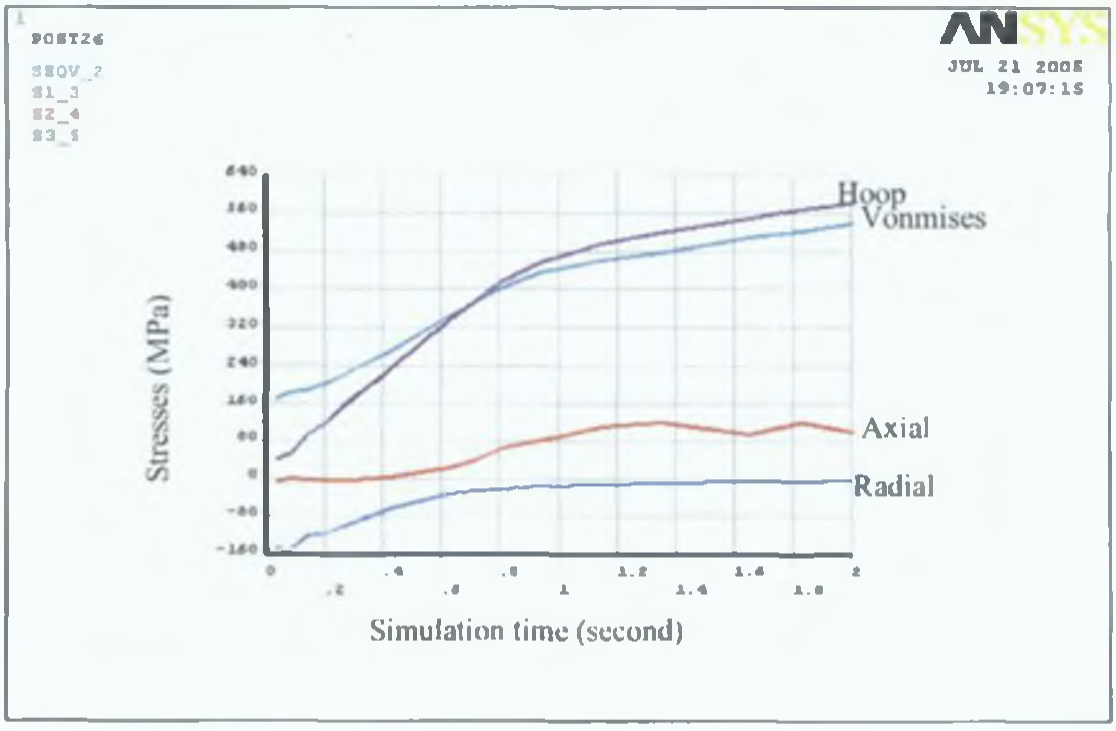

Figure 5.11.: Development of stresses on top central node of the external tube of the simulated X branch by 10 mm axial feed and 70 MPa pressure load

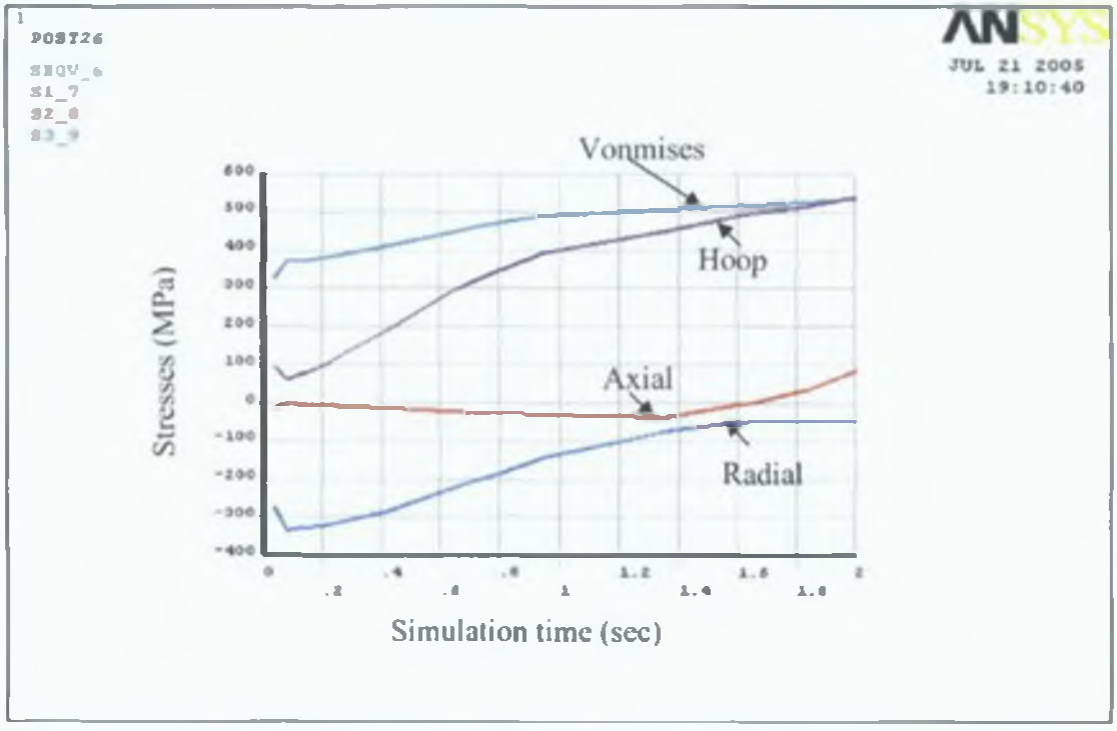

Figure 5.12.: Development of stresses on top central node of the external tube of the simulated X branch by 10 mm axial feed and 70 MPa internal pressure

It is because the materials did not flow uniformly and the existence some thinning and thickening for the forming process. Figure 5.11 depicts the stresses distribution on the top central node over the simulation time. It can be seen that the axial stress increases after a certain time. This abnormality was due to the expansion of the internal tube. Radial stress was compressive over the simulation time. Figure 5.12 shows the stresses developed on the top central node in the internal tube. It can be noticed that the equivalent stress was dominant and at the end both hoop stress and von mises stress intersect at a point but total stress remains well below the ultimate stress.

5.2.4 10 mm axial feed and 80 MPa internal pressure

The simulation has been carried out for the previous boundary conditions by only changing the load constraints. Axial feed was applied 10 mm for both side and internal pressure was 80 MPa. The solution has been completed by 19 total sub steps in two seconds. But the first 12 sub steps within 0.793 seconds were considered. In this time, the maximum stress developed in the tube was 475 MPa apparently which is well below the ultimate stress of the materials. Figure 5.13 presents the von mises stress distribution over the simulated X branch tube. Maximum stress has been located in the bottom region of the branch height. Due to compressing the material from both end and finding no other way to flow the materials around the bottom region of the branch hole, this leads to stress concentration in this area of the form products.

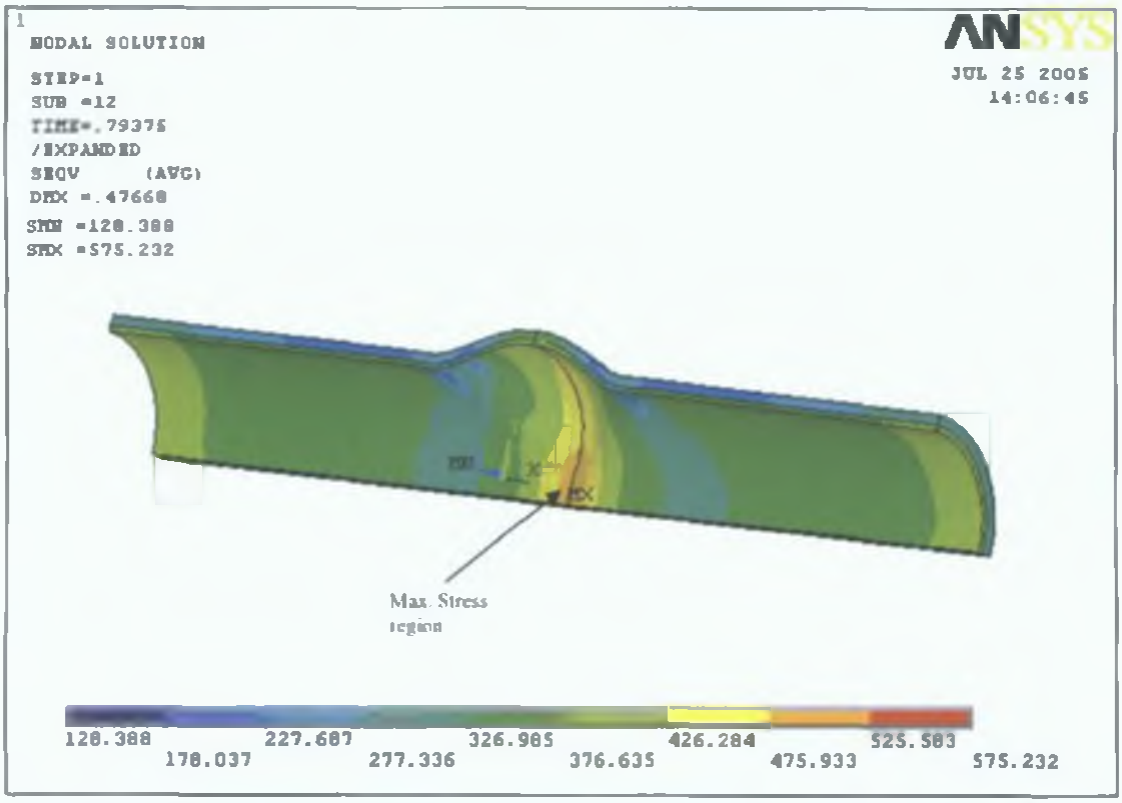

Figure 5.13.: Von-mises stress distribution for the simulation carrying out by 10mm axial feed and 80 MPa pressure

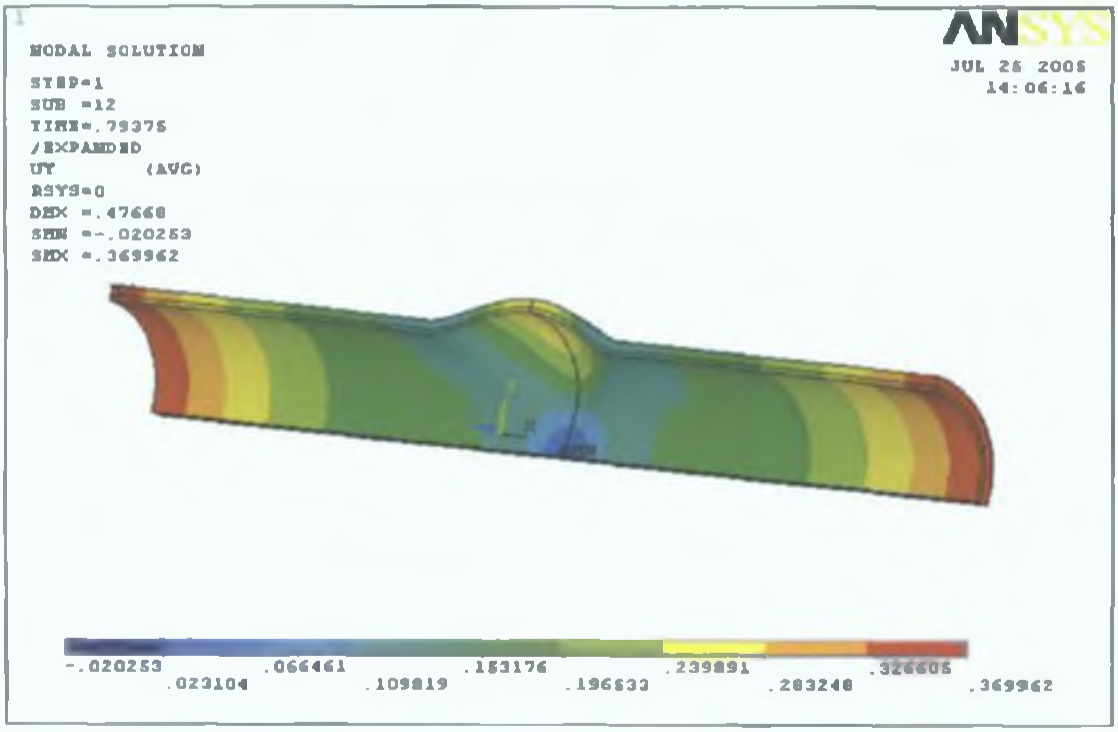

Figure 5.14.: Deformation and branch height of the simulated X branch by 10 mm axial feed and 80 MPa internal pressure

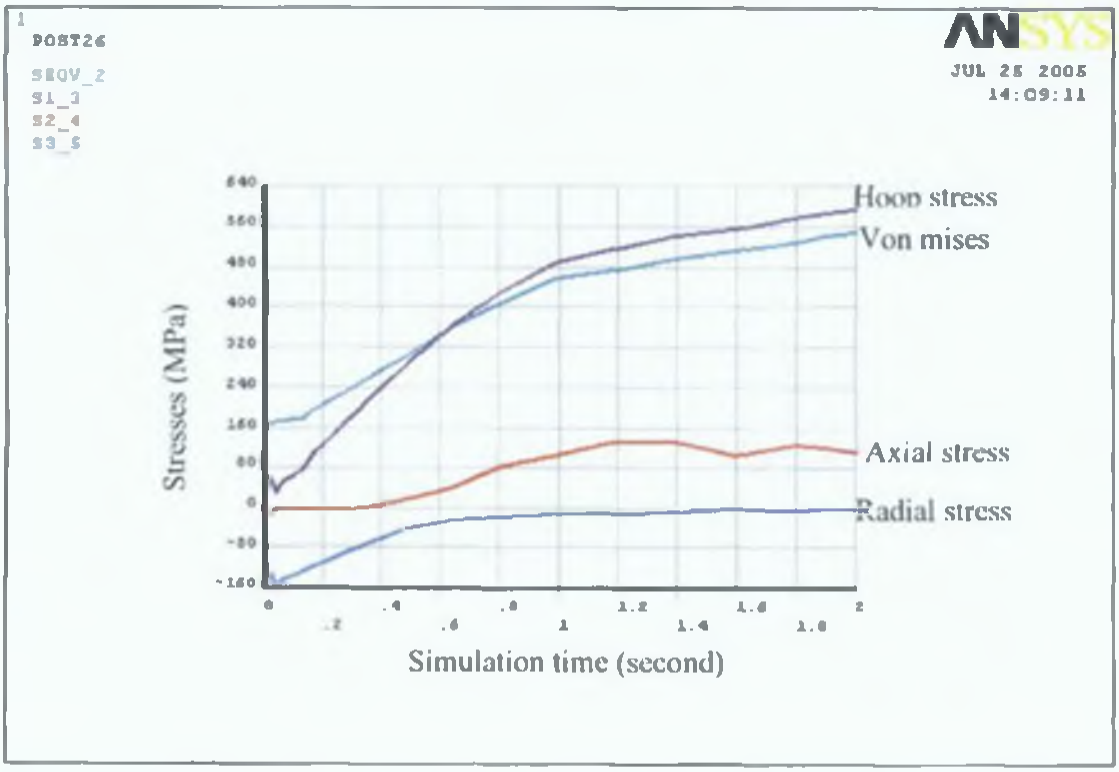

Figure 5.15.: Development of von mises and hoop stress on top central node by 10 mm axial feed and 80 MPa pressure load

To reduce the stress from this region a high internal pressure should be introduced. This will be discussed in the later section of this chapter. From figure 5.13 it is clear that stresses are well distributed over the branch and tube very uniformly. Figure 5.14 describes the deformation condition of the tube for this simulation after a time of 0.793 seconds. It can be summarized that after this time the maximum deformation was 0.4766 cm and the branch height was 0.3699 cm. Certainly it is little bit higher than the previous simulation which was carried out for 70 MPa internal pressure. Figure 5.15 depicts the stress distribution over the top central node of the outer layer tube. Hoop stress is more dominant after a certain time during the solution and radial compressive stress tends to zero at the end of the solutions.

5.2.5 10 mm axial feed and 100 MPa internal pressure

This solution has been conducted by 100 MPa internal pressure. It took 17 sub steps to complete the solution within 2 seconds but it reaches near the ultimate stress by shorter time in comparison with the previous solutions.

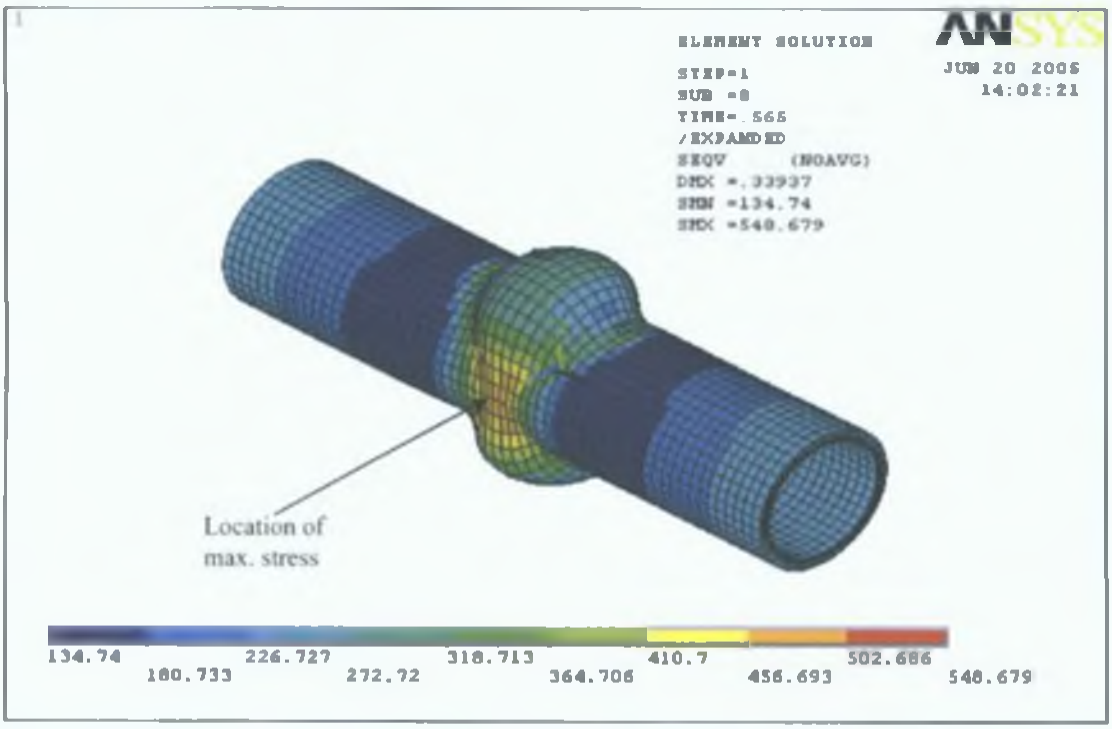

Figure 5.16.: Von-mises stress distribution over the simulated X branch by 10mm axial feed and 100 MPa pressure

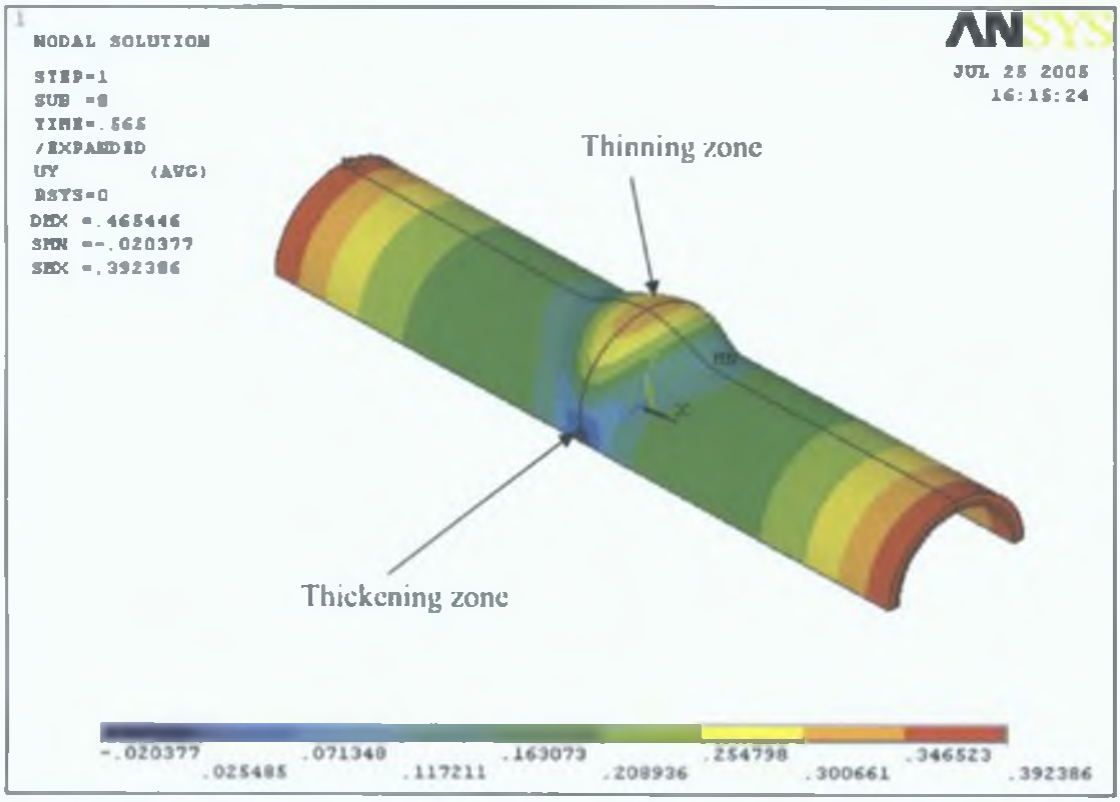

Figure 5.17.: Deformation and branch height of the simulated X branch by 10 mm axial feed and 100 MPa internal pressure

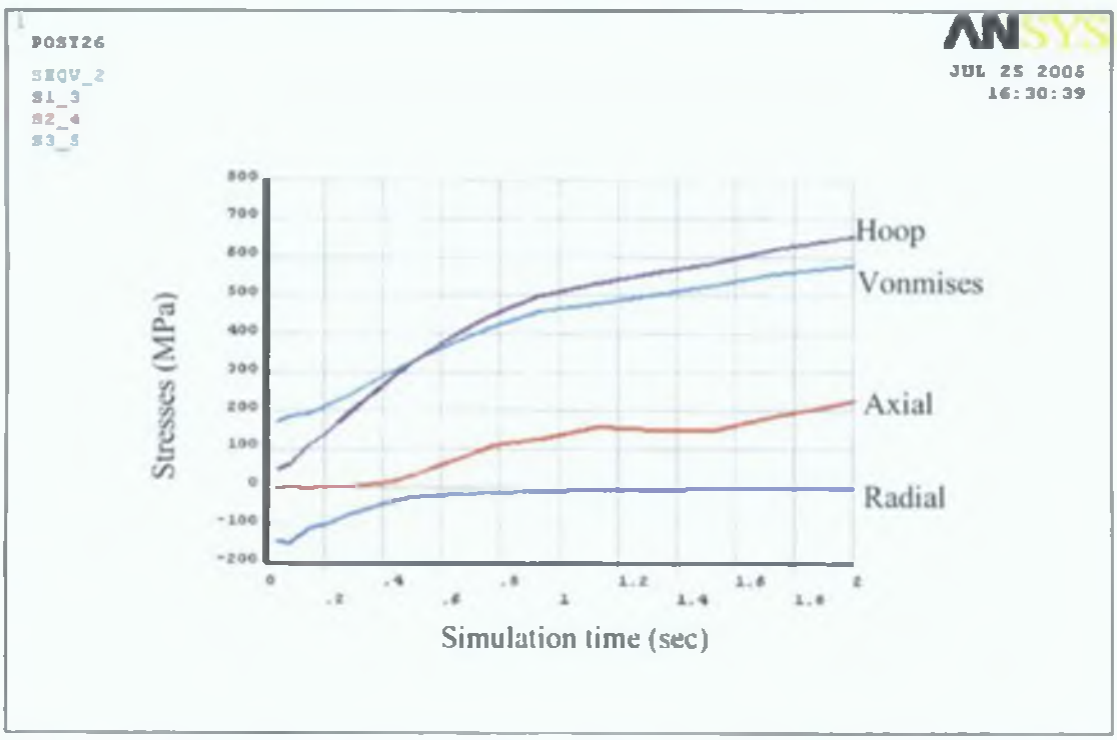

Figure 5.18.: Stress distribution on a top central node of the simulated X branch by 10 mm axial feed and 100 MPa pressure load

Due to the high internal pressure, the outer layered tube experiences more tensile stress during the deformation. Figure 5.16 describes the von mises stress distribution over the simulated X branch by 100 MPa internal pressure and 10 mm axial feed. It can be seen from the figure that over the branch area there is a higher tensile stress than the undeformed part of the tube. It is because of applying higher internal pressure compared to the axial feed. It is very important in the hydroforming process to balance the combination of internal pressure and the axial feed in order to get good products. Figure 5.17 shows the deformation of the simulated branch. It is clear that maximum deformation at a time of 0.565 second is 4.65 mm but the bulge height was 3.92 mm. Figure 5.18 shows the stress distribution over the simulation time on the top central node of the simulated X branch. Radial stress becomes nil after a time of 1 sec and it stays up to the end of the solution.

5.2.6 10 mm axial feed and 150 MPa internal pressure

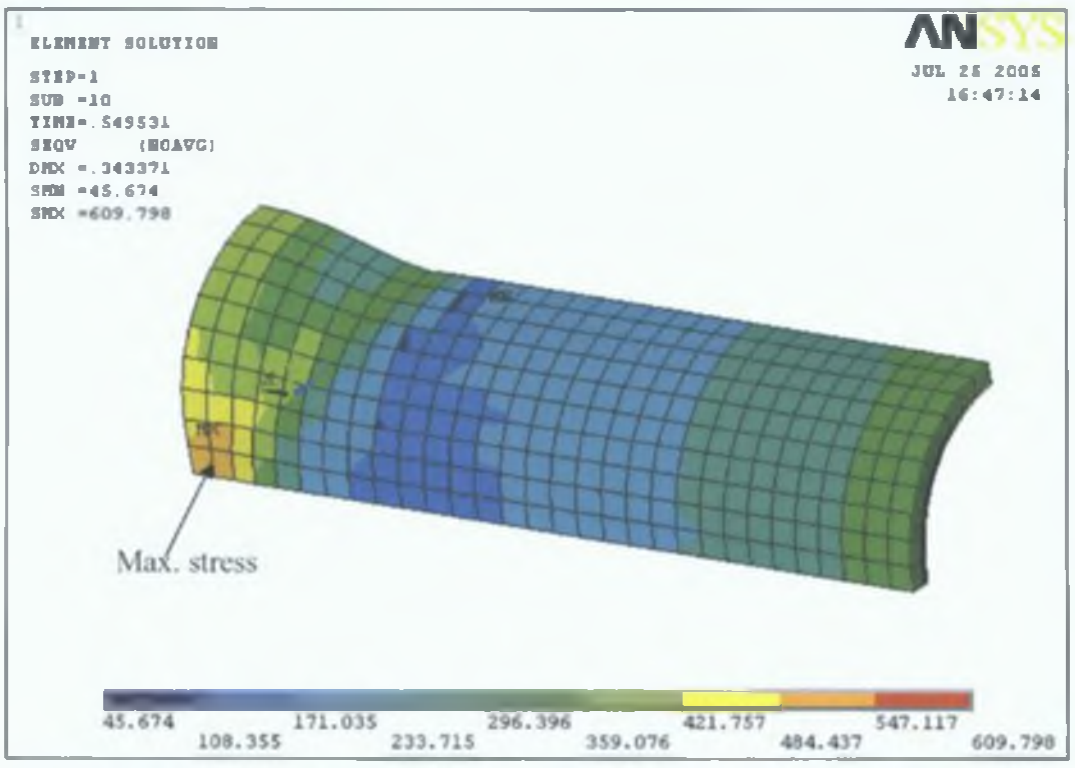

Figure 5.19.: Von-mises stress distribution for the simulation of X branch by 10mm axial feed and 150 MPa pressure

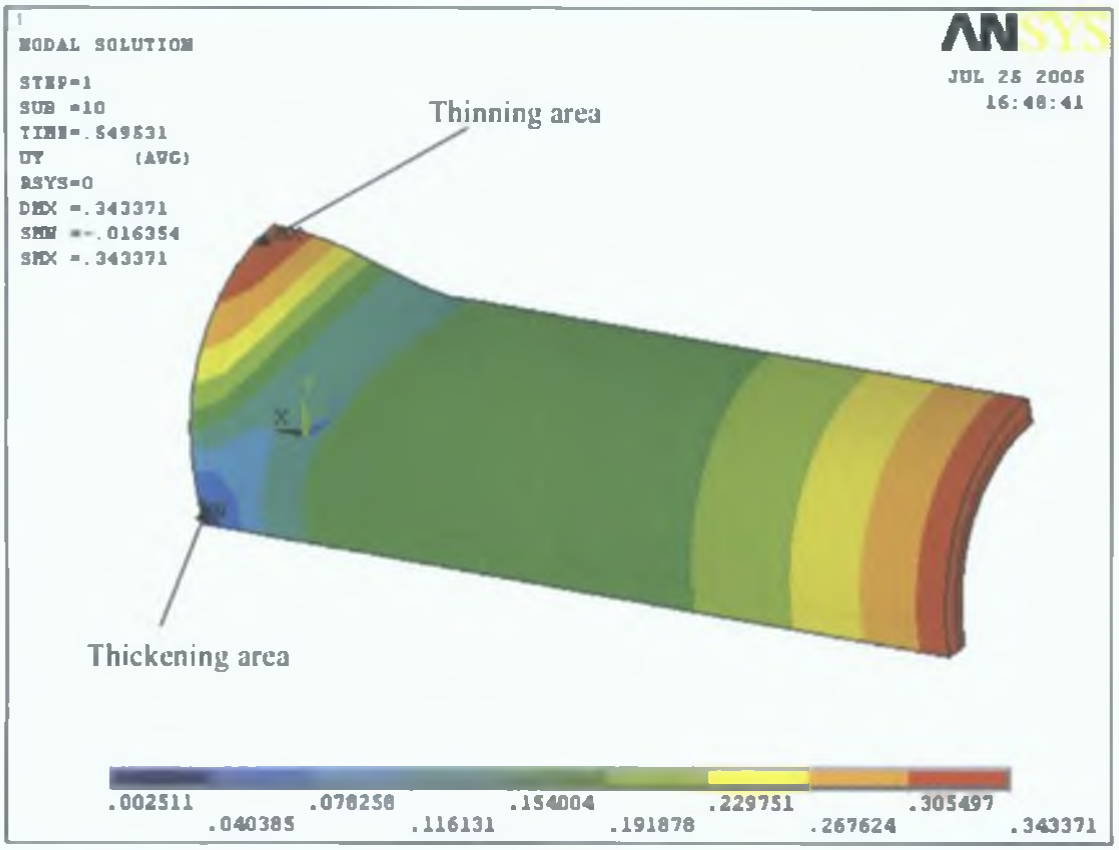

Figure 5.20.: Deformation and branch height of the simulated X branch by 10 mm axial feed and 150 MPa pressure

This solution has been run for 150 MPa internal pressures and keeping the axial feed the same as in the previous solution. The solution was completed by 25 sub steps in 2 seconds. A comparison among the previous simulated results in this chapter have been carried out for different loading conditions, it can be summarized that by fixing the model geometry, material properties and the solution time constant, the number of sub steps in the solution has been increased by increasing the load constraints. Figure 5.19 describes the von mises distribution over the simulation time. It can be concluded that at a time of 0.549 second the maximum von mises stress in the bi-layered tube was 484 MPa apparently. An average of 484 MPa of stress has been developed in the bulge area. Figure 5.20 presents the deformation condition of the tube after a time of 0.549 second. It can be noticed that the maximum deformation of the multi-layered tube was 3.433 mm in the axial direction which is exactly equal to the bulge height of this simulation. It can

be concluded that the material flow during the solution was very uniform. The most thinning area was the top of the bulge while the bottom region might be the most thickening region. The higher tensile stress distribution over the bulge area indicates that in the loading condition the internal pressure was relatively higher than the axial feed.

To define the effect of the axial feed while fixing the internal pressure, a further solution has been run by applying 150 MPa internal pressure and the axial feed was increased to 20 mm instead of 10 mm. The solution completed by 30 sub steps.
Figure 5.21 shows the von mises stress distribution over the branch area of the formed product. A comparison between figure 5.19 and 5.21 where the simulation were carried out for the same pressure but different axial load. It can be noticed from this result that the stress over the branch area is lower than the previous simulation (10 mm axial feed). Due to the higher axial feed, where the material was pushed inward with more compressive load than the previous case a fraction of the tensile stress releases over the branch area of the simulated tube. It is an optimum condition for forming without developing extra stress over the branch area. Some part of tensile stress neutralizes due to the action of more compressive axial feed. Looking at the figure 5.21 it is clear that the bulge top is flatter than all other solution in this chapter. It can be concluded that in this solution the material flow was more uniform than the previous solution stated in fig 5.19. It also can observed that thickness over the branch top is more uniform which is one of the most desirable feature of the forming condition in hydroforming process.
Maximum stress has been located on the bottom region of the bulge in the formed tube.
Figure 5.22 presents the deformation condition and bulge height for the simulation carried out by 20 mm axial feed and 150 MPa internal pressure. The thinner area is on the top of the bulge and the thicker are is located at the bottom of the branch. After completing 30 sub steps of the solution, maximum bulge was 12.9 mm and the maximum deformation occurred in the tube was 20.01 mm.

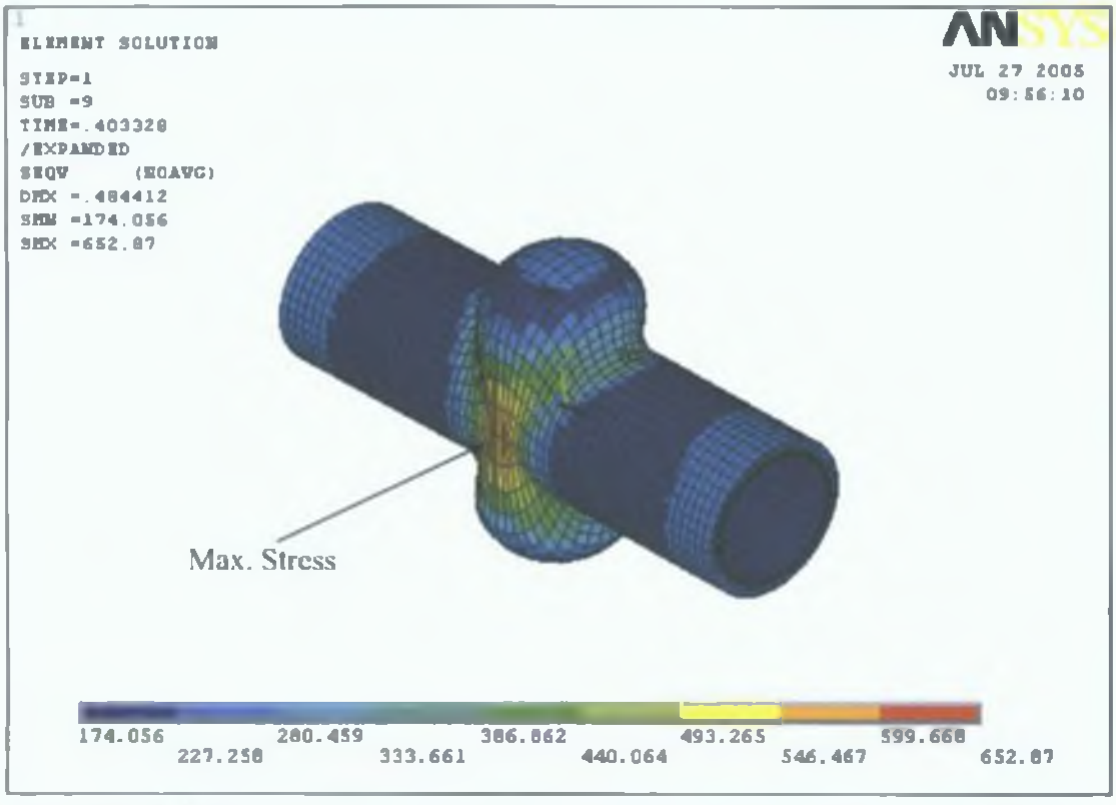

Figure 5.21.: Von-mises stress distribution for the simulation carrying out by 20mm axial feed and 150 MPa pressure

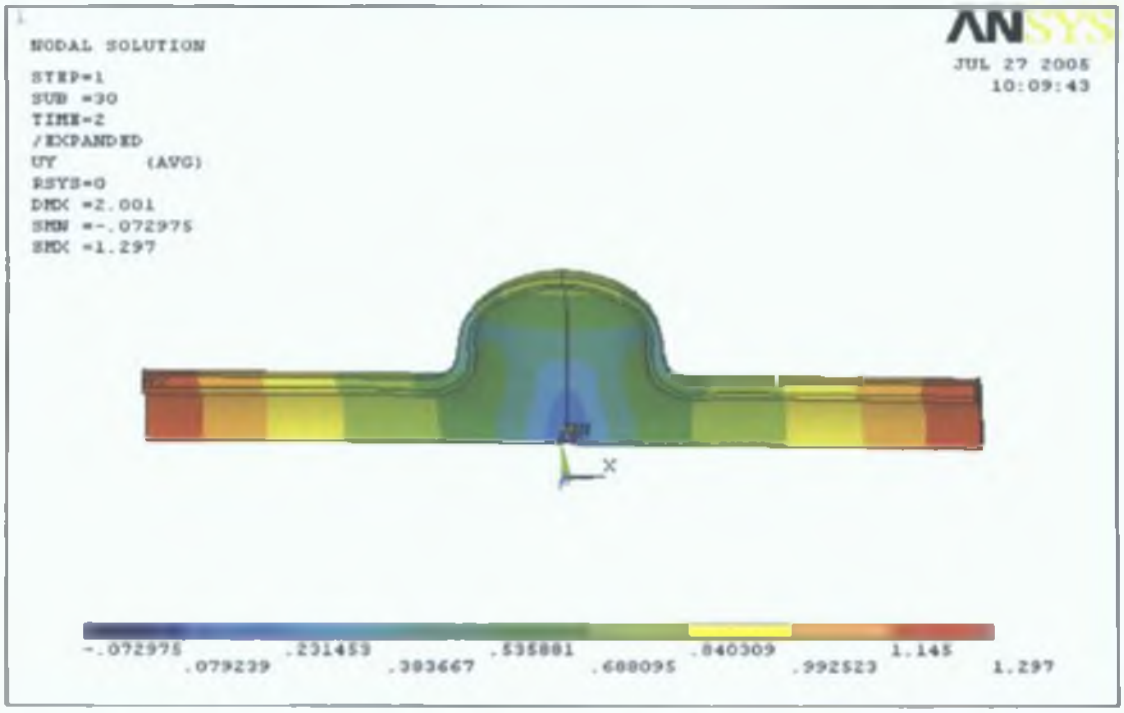

Figure 5.22.: Deformation condition for simulated X branch by 20 mm axial feed and 150 MPa internal pressure

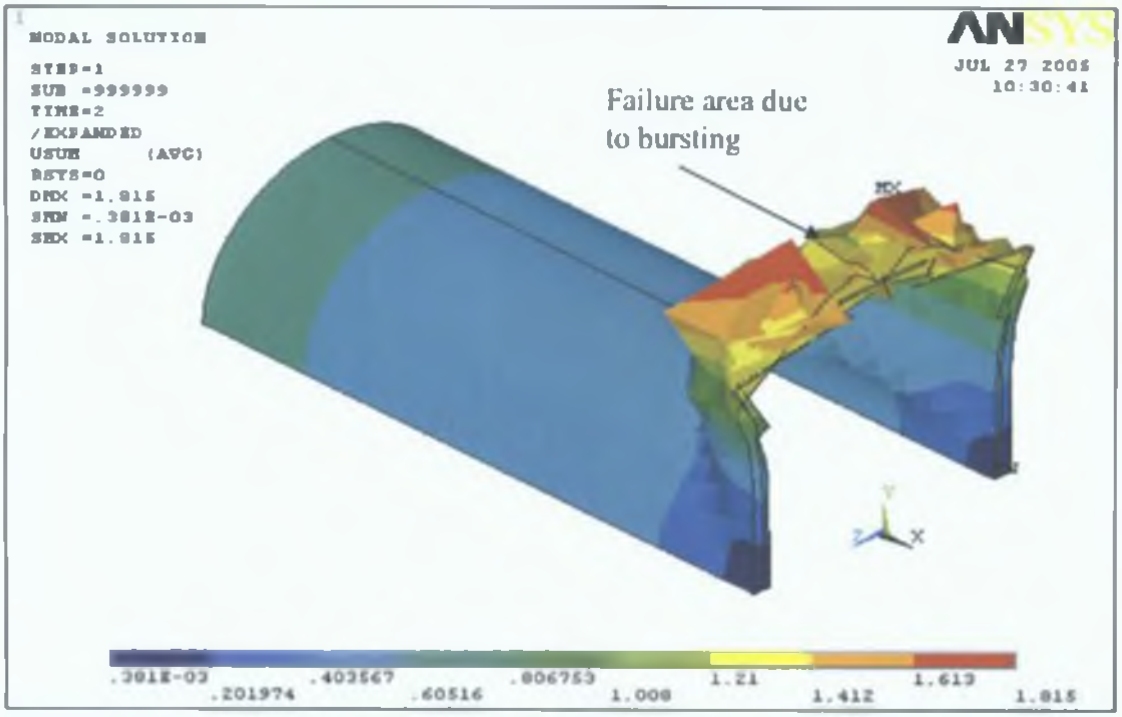

Figure 5.23.: Bursting failure of a simulated X branch due to high internal pressure, by 10 mm axial feed and 200 MPa internal pressure

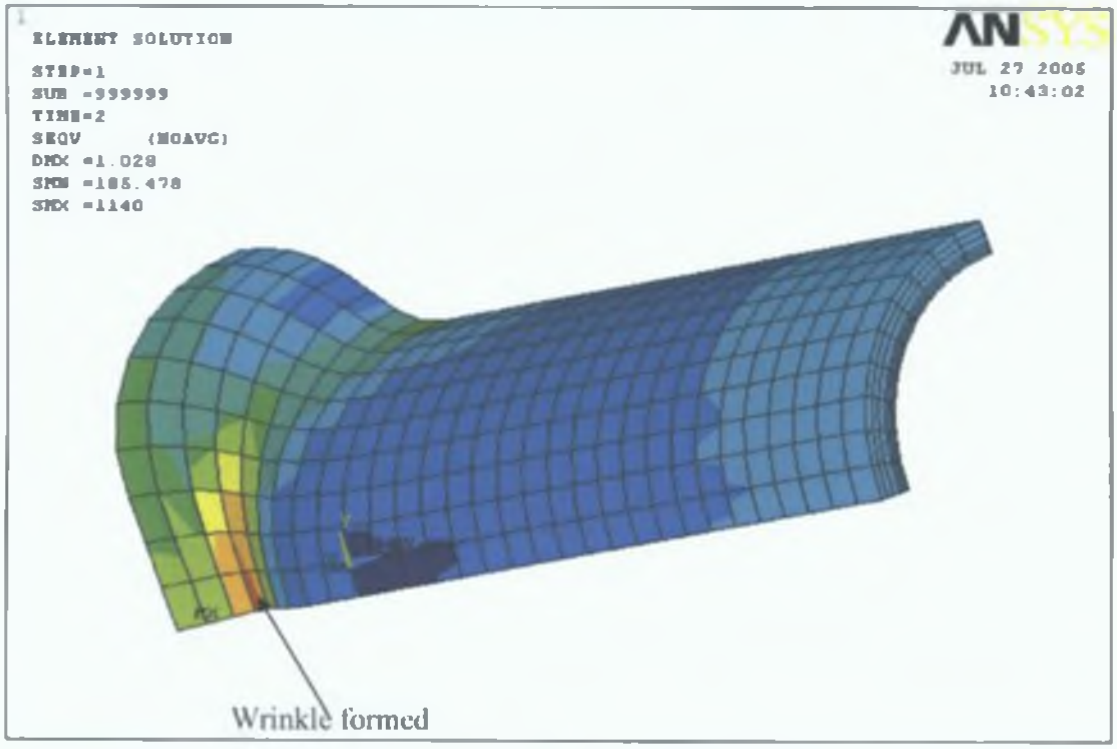

Figure 5.24.: wrinkling failure occurred by 30 mm axial displacement and 40 MPa internal pressure

The next simulation has been carried out for 200 MPa internal pressure and 10 mm axial displacement. At this pressure the tube burst due the excessive thinning in the top region of the branch. Figure 5.23 depicts the failure of the multi-layered tube by bursting due to high internal pressure. By applying a high internal pressure compared to the axial feed, the material does not flow uniformly over the length of the tube, because the internal pressure is neutralized by the reaction force of the rigid die surface in the tube except the die hole area. A high internal pressure can deform the tube near the hole of the die branch, as a result materials in this region experience more stretch than the other area of the tube. Due to the continuous action of the internal pressure the elongation increases continuously as long as the pressure exists at the internal surfaces of the tube. Because of the application of a relatively small axial feed the material supply is not sufficient towards the die hole, where the top area of the branch became thinner and at the end the tube burst.

Figure 5.24 shows a typical wrinkling failure of hydroforming process. This solution has been carried out in order to observe the wrinkling failure by applying 40 MPa internal pressure and 30 mm axial feed. In hydroforming process which involve end axial and internal pressure, it is desirable that the end axial feed over the process time should be as high as possible, to allow as much material as possible to be fed into the forming zone. This excess material pushed into the deformation zone helps in maintaining the wall thickness near the highly strained areas within the desired limits. However, the actual value of the axial feeding in the process is limited by the occurrence of wrinkles or buckling. Excess material pushed into the forming zone may result either buckling or excess wall thickening in certain zones. Figure 5.24 represents one of these ideal conditions. In this solution less internal pressure has been applied compared to the axial feed because the material could not flow along the die hole due to the low internal pressure this would result with tube wrinkled or buckled in the certain region.

5.3 Hydroforming of T branches at different loading conditions

5.3.1 10 mm axial feed and 50 MPa internal pressure

The model was built as with the X branch as described in the previous section of this chapter. Material properties and the contact element have been kept as described in section 5.2. Taking the symmetry advantages one quarter of the whole model has been analyzed. The same load patterns have been applied as have done for X branch simulation in the previous section. This simulation has been carried out for 10 mm axial feed and 50 MPa internal pressure. The solution completed within 2 seconds. The total solution has been completed in 15 total sub steps but after a time of 1.28 second in 10 sub steps the maximum equivalent von mises stress exceeded beyond the ultimate stress of the materials of the bi-layered tube. It can be stated that the solution completed safely by 10 sub steps. Figure 5.25 shows the branch height of the simulated T branch for this simulation and it is clear from the figure that maximum branch height after a time of 1.28 second and 10 sub steps was 2.06 mm. Figure 5.26 depicts the von mises stress distribution over the simulated T branch for this condition of solution. It is clear that maximum developed stress was 529 MPa which is well below the ultimate stress of the materials. It can be noticed from the figure that both ends of the tube experienced highly compressive stress and over the whole area of the branch stress distributed nicely uniform. Figure 5.27 describes the stresses distribution over the top central node of the simulated T branch. It can be summarized that hoop stress and equivalent stress increased linearly and at the same rate over the simulation time. No particular effect of axial stress on the solution and radial compressive stress remain almost constant up to the end of the solution.

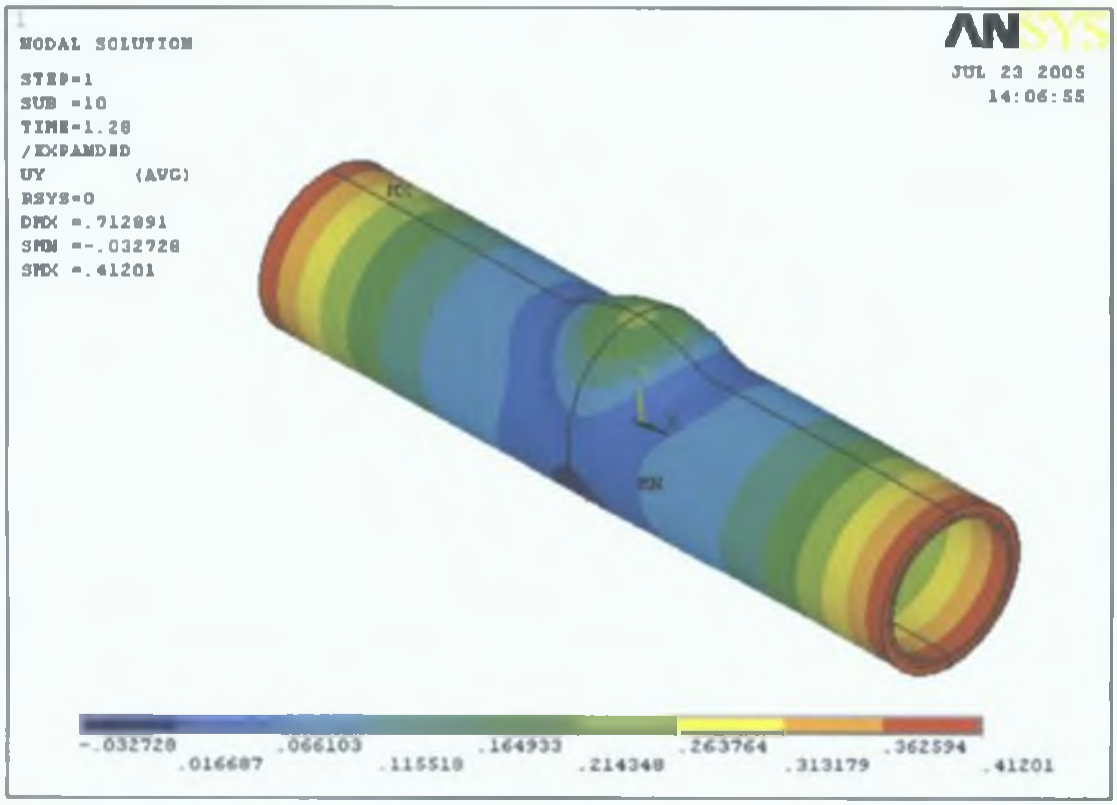

Figure 5.25.: Deformed simulated T branch by 10mm axial feed and 50 MPa

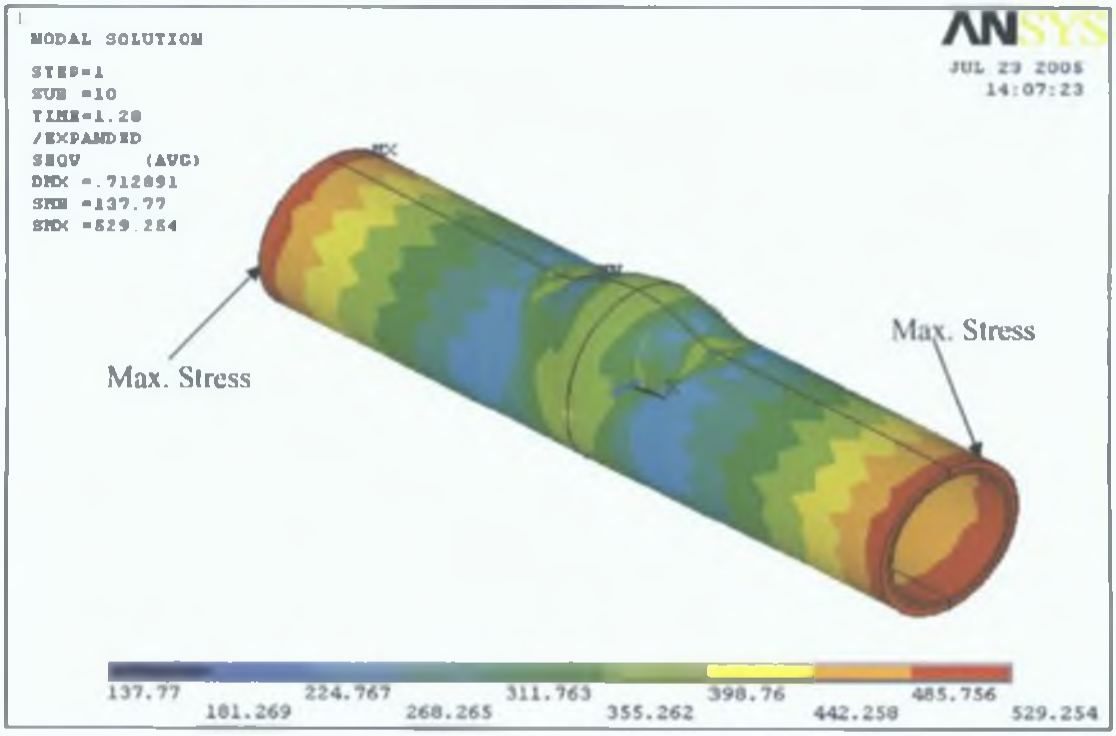

Figure 5.26.: von mises stress distribution over the simulated T branch by 10 mm axial feed and 50 MPa internal pressure

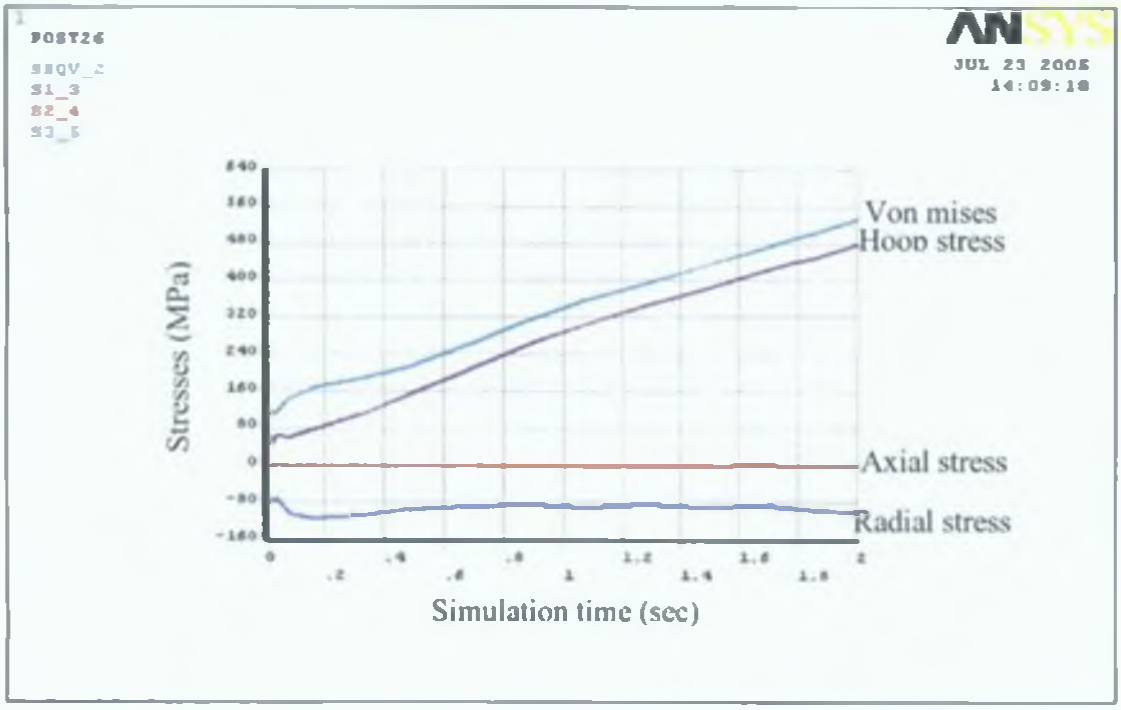

Figure 5.27.: Stress distribution over the top centre node of the formed T branch by 10mm axial feed and 50 MPa

5.3.2 Loading condition; 10 mm axial feed and 60 MPa internal pressure

This simulation has been carried out for the same model as described in section 5.3.1 only by changing the internal pressure, in this case 60 MPa internal pressure has been applied to carry out the solution. Load function has been defined for maximum of 2 second and the solution has been completed by 18 sub steps. But after 12 sub steps it reaches near the ultimate stress of the materials, as a result all solutions have been ignored after 12 sub steps. To complete this solution it took 0.9793 second. Figure 5.28 depicts von mises stress distribution at 12 sub steps of the solution and it is clear that the maximum von mises stress is a bit less than the previous case of simulation carried out. On the other hand compressive stress at the ends of the multi layered tube is a bit lower than the previous results stated in figure 5.26; it is because of increasing the internal pressure the material stretched with more tensile stress than compressive from the two ends of the tube due to action of more internal pressure and the material flowed more uniform which resulted with extra bulge height. Maximum branch

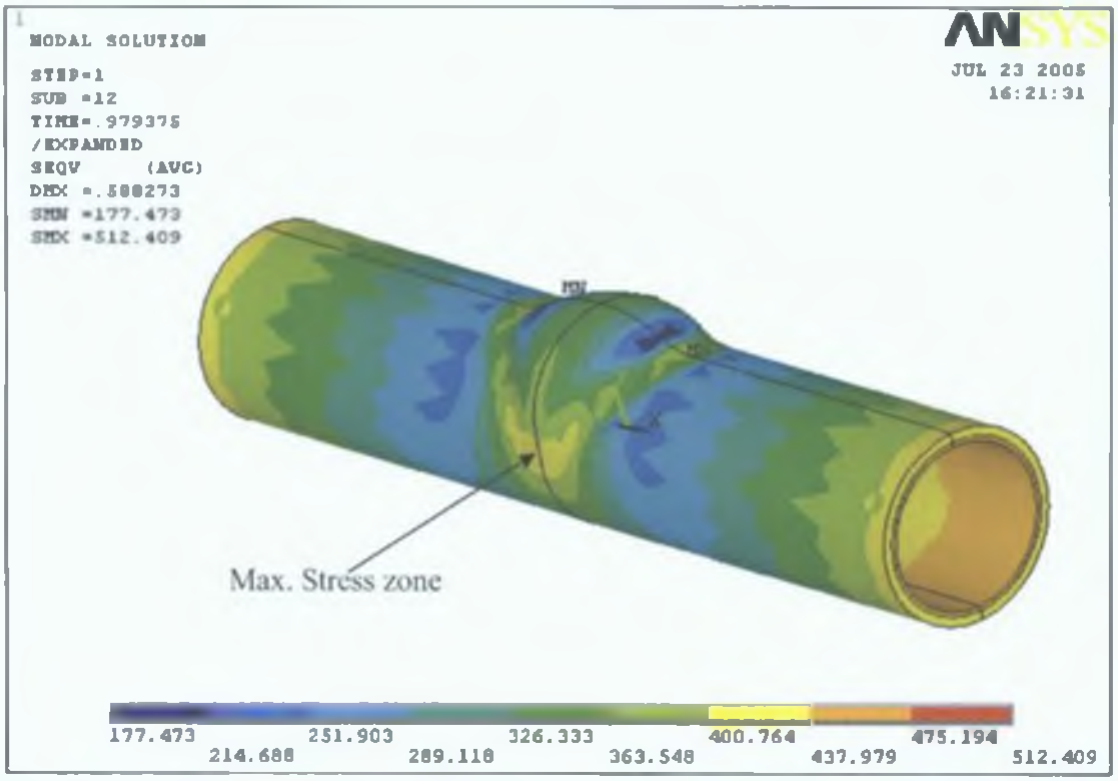

Figure 5.28.: Von mises stress distribution over the simulated T branch by 10mm axial feed and 60 MPa pressure

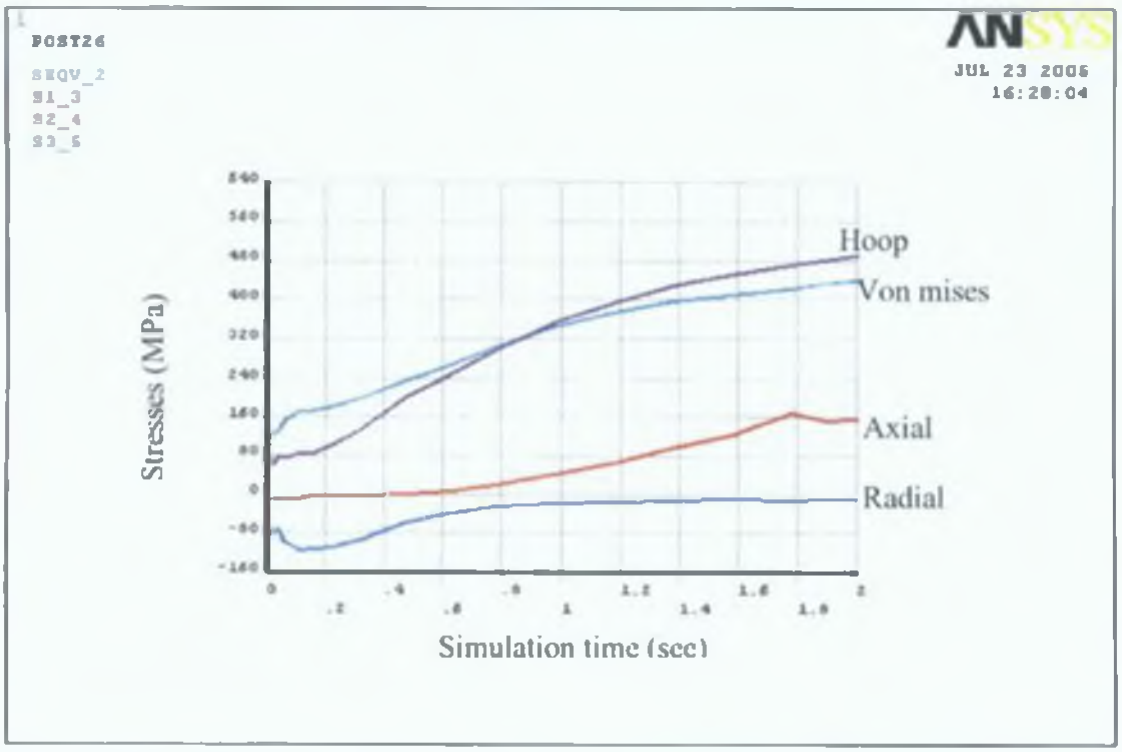

Figure 5.29.: Stress distribution over a top centre node of the formed T branch by 10mm axial feed and 60 MPa internal pressure

height was 2.9 mm in this case. Maximum stress was concentrated on the bottom region of the branch while over the branch area the stress distributed moderately uniform. Figure 5.29 shows stress distribution over the top central node of the hydro formed T branch. It is clear that elastic region is more visible in this case and in the plastic region, hoop stress is more dominant than other stresses after a certain time even though the equivalent stress remains well below the ultimate stress of the material over the complete simulation time. On the other hand radial stress and axial stress prevail according to the usual conventional way.

5.3.3 Loading condition; 10 mm axial feed and 70 MPa internal pressure

This solution has been performed by 10 mm axial feed and 70 MPa internal pressure and all other loading condition and constraints have been kept identical as have done for the previous simulation. This solution also solved in 2 second and 18 sub steps, after 12 sub steps all results have been ignored due to exceed the ultimate stress as happened in previous case. The bulge height has been found in this case 3.7 mm.

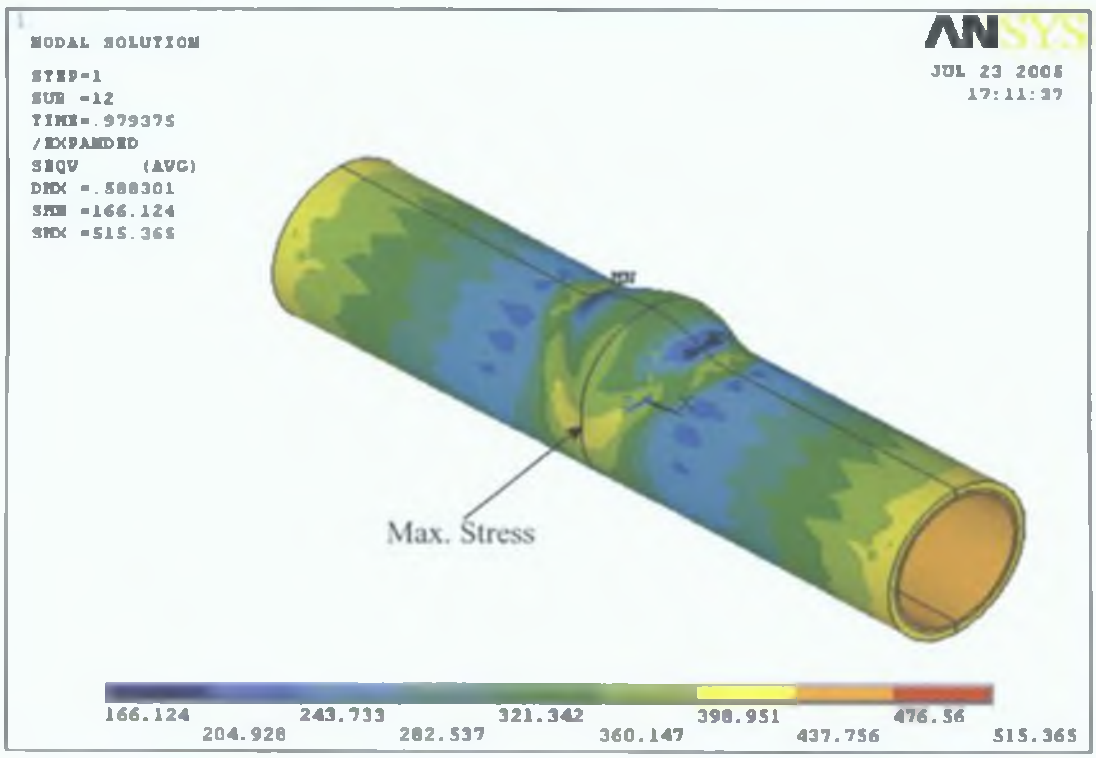

Figure 5.30.: Von mises stress distribution over the simulated T branch by 10mm axial feed and 70 MPa pressure

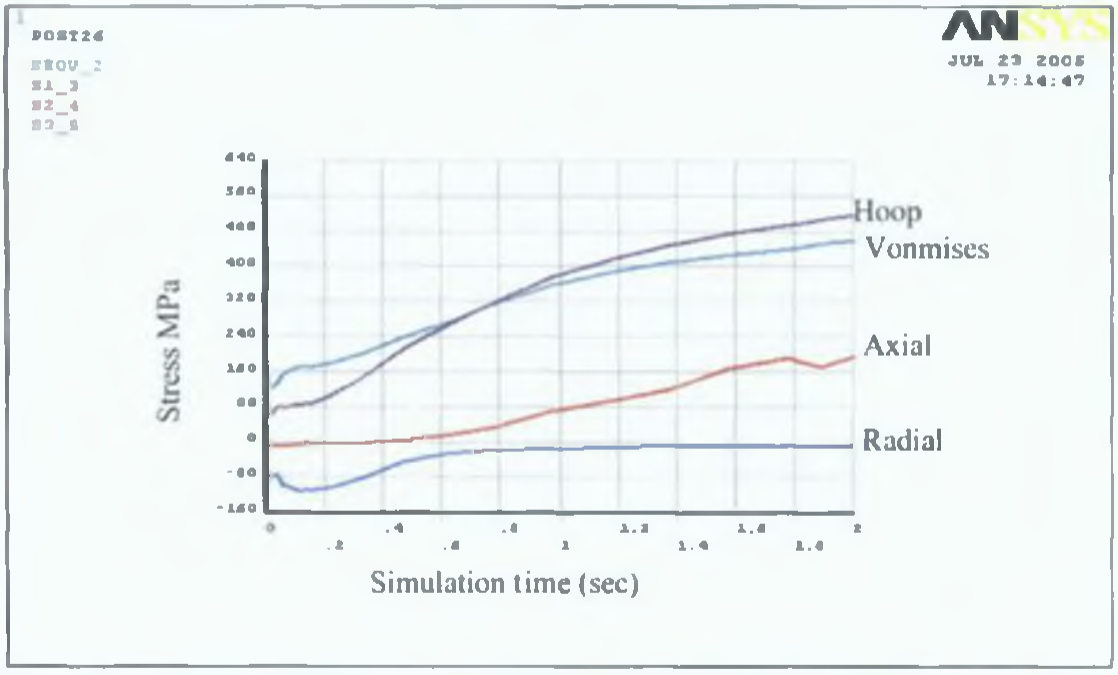

Figure 5.31.: Stress distribution over the simulated T branch by 10mm axial feed and 70 MPa pressure

Figure 5.30 shows the von mises stress distribution over the simulated T branch. Maximum stress developed in the bottom region of the bulge and the value is 398 MPa apparently. Figure 5.31 describes stresses distribution over the top central node of the hydro formed T branch. Axial stress becomes tensile after a short time and in increases up to end of the solution. Radial stress becomes zero and the end of simulation.

5.3.4 10 mm axial feed and 80 MPa internal pressure

The simulation has been carried out for the previous model by changing only the load constraints. Axial feed was10 mm for both side and internal pressure was 80 MPa. The solution has been completed by 24 total sub steps. After a time of 0.923 second in 18 sub steps the solution has been found in safe region and beyond this time solution other sub steps were ignored due to the materials failure. At this stage maximum deformation has been occurred 5.55 mm and the maximum bulge height was 3.84 mm. It can be concluded from this deformation and maximum bulge height that material flow during the simulation was not quite uniform.

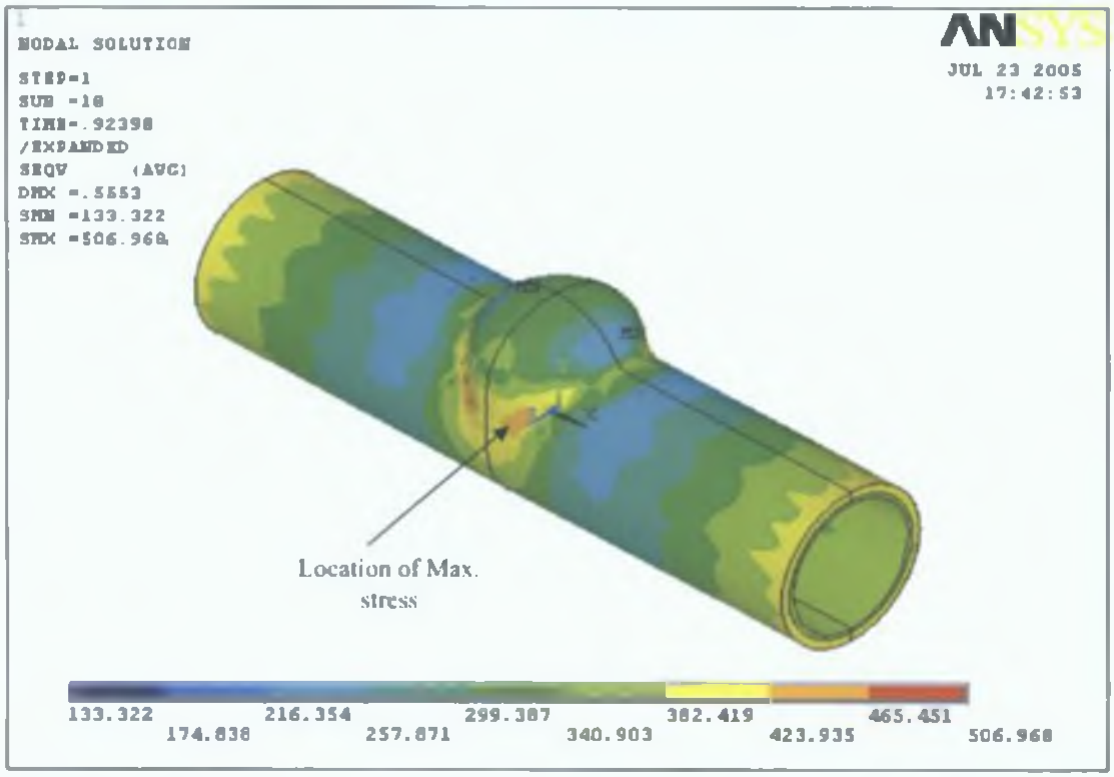

Figure 5.32.: Von-mises stress distribution for the simulation carrying out by 10mm axial feed and 80 MPa pressure

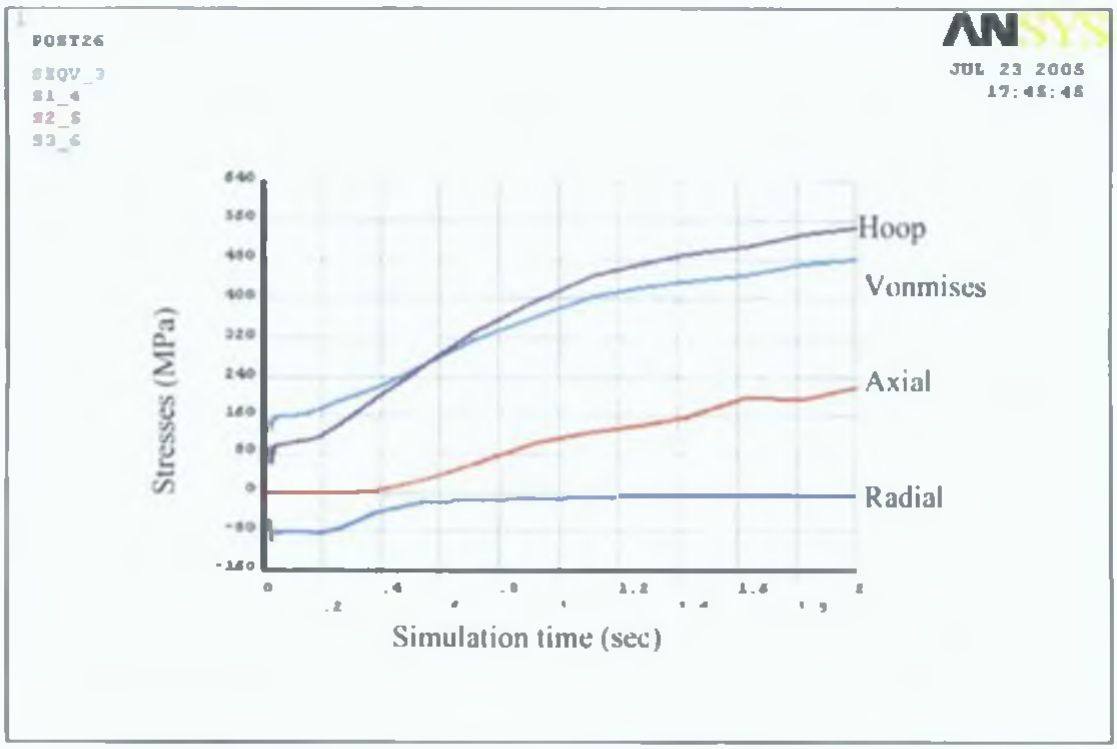

Figure 5.33.: Stress distribution on a top central node of the simulated T branch by 10mm axial feed and 80 MPa internal pressure

Figure 5.32 describes the von mises stress distribution over the simulated T branch. It is clear from the figure that the maximum stress has been concentrated on the bottom area of the formed branch. The maximum stress was 506 MPa which is well below the ultimate stress of the materials. Stresses over the area of the branch and tube were distributed more uniformly. Figure 5.33 depicts the stresses distribution of a top central node of the formed branch. It is clear that elastic region is very small and in the plastic region hoop stress exceeds the equivalent stress after a certain time during the simulation. A certain amount of tensile axial stress act on the outer tube during the plastic deformation it is due to the expansion of the internal tube. While in the internal tube axial stress remained almost constant over the simulation time. On the other hand compressive radial stress was almost zero after time 0.8 second to the end of the simulation. In the plastic region hoop stress is more dominant which is good condition for the forming products by applying internal pressure.

5.3.5, 10 mm axial feed and 100 MPa internal pressure

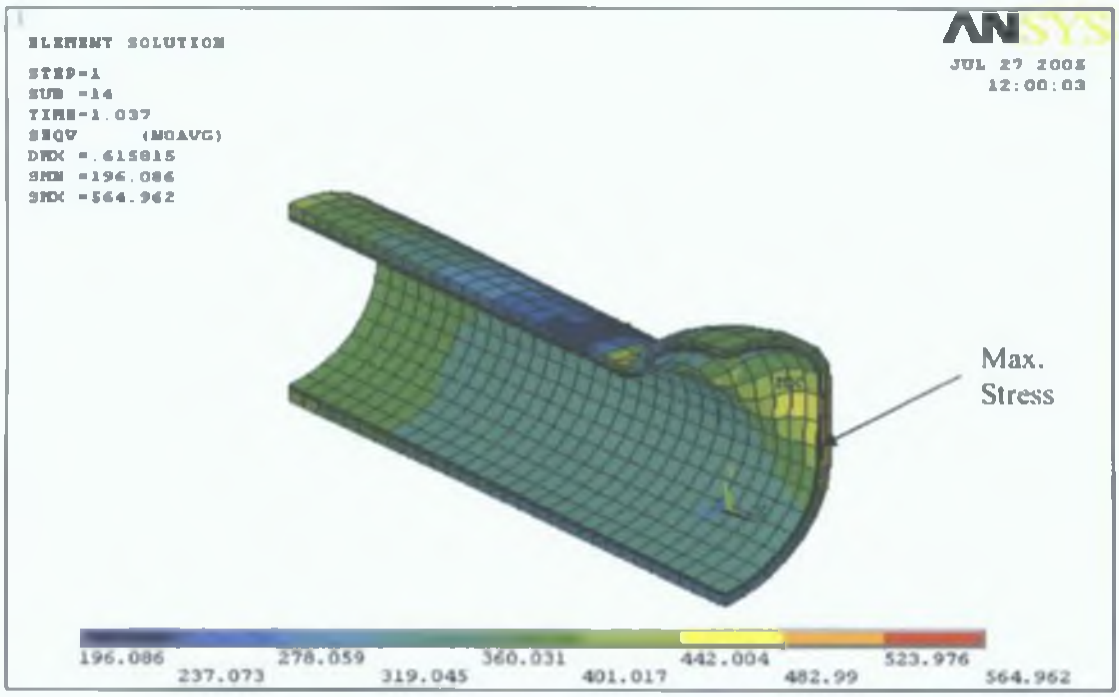

Figure 5.34.: Von mises stress distribution over the simulated T branch by 10mm axial feed and 100 MPa pressure

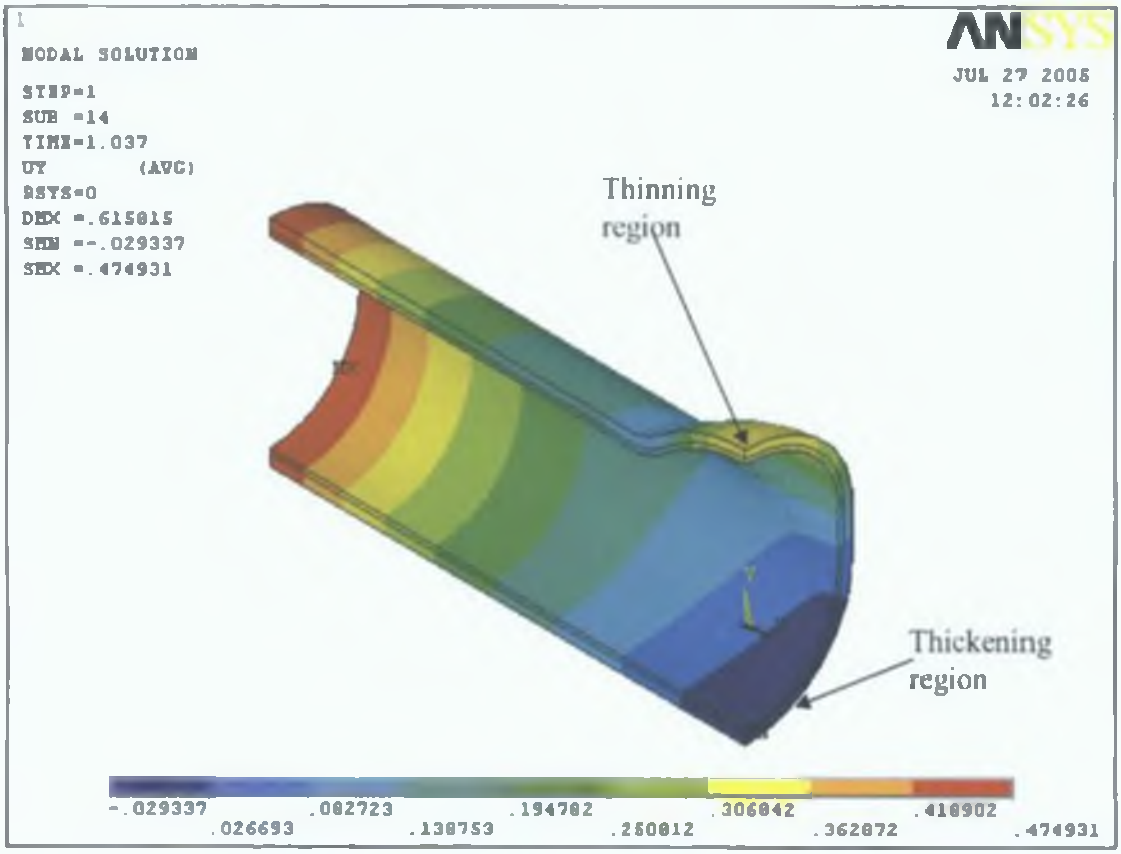

Figure 5.35.: Deformation of simulated T branch by 10mm axial displacement and 100 MPa pressure

This solution has been carried out for 100 MPa internal pressure loading condition. Solution completed by 23 sub steps in 2 second but at 1.037 second after14 sup steps equivalent stress reaches near the ultimate stress of the materials. Figure 5.34 depicts von mises stress distribution over the simulated T branch. Stress over the tube and the branch area distributed very uniformly with a bit concentrated in the bottom region where the stress was the maximum. By the time of 1.037 second during the simulation the maximum deformation was 6.158 mm and bulge length was 4.749 mm. Figure 5.35 shows the deformation condition for the solution by this time. Figure 5.36 describes the stress developed on a top central node of the simulated T branch. It can be seen that von mises stress slightly exceeds the ultimate stress. Radial stress becomes nil after a certain time during the solution and remained up to the end of the solution.

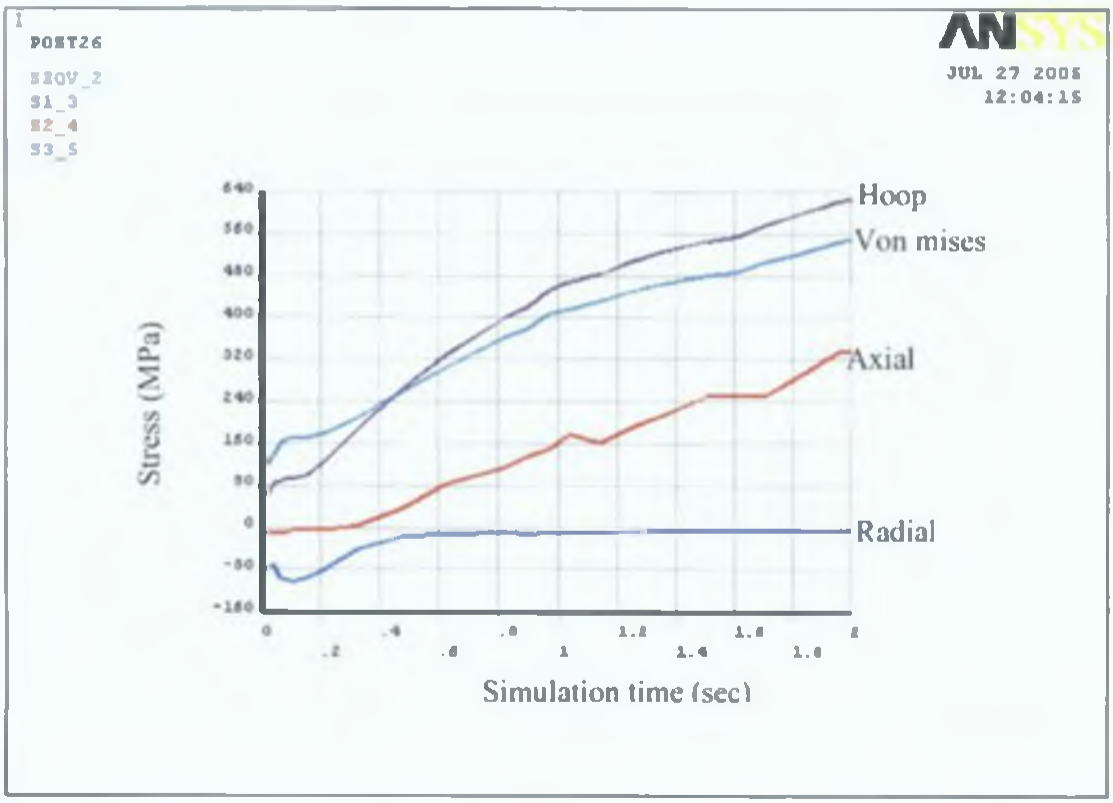

Figure 5.36.: Stress distribution over a top centre node of the formed T branch by 10mm axial feed and 100 MPa pressure

5.3.6 10 mm axial feed and 150 MPa internal pressure

This solution has been run for 10 mm axial feed and 150 MPa internal pressure. The solution has been completed by 26 sub steps in 2 seconds but at time 0.9976 seconds the equivalent stress reaches near the ultimate stress of the tube materials. By this time the solution runs to 13 sub steps. Figure 5.37 shows von mises stress distribution over the simulated T branch. The maximum stress was located at the bottom region with a value of 506 MPa. Stress over the tube area is moderately distributed. Figure 5.38 presents the deformation condition for this simulation. It is clear that the maximum deformation was 5.99 mm and the bulge height was found to be 5.89 cm which is very near to the total deformation. The material flow was relatively uniform. Also it can be noticed from this figure the thickening and thinning region of the simulated T branch.

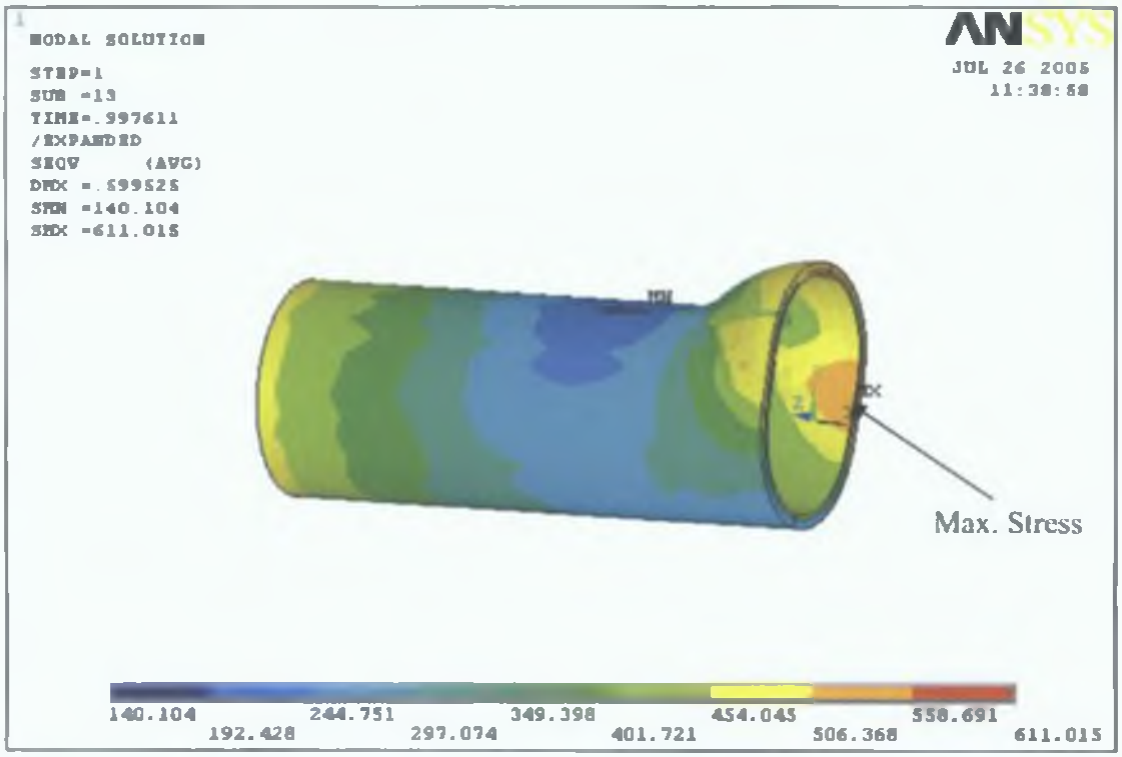

Figure 5.37.: Von mises stress distribution over the simulated T branch by 10mm axial feed and 150 MPa pressure

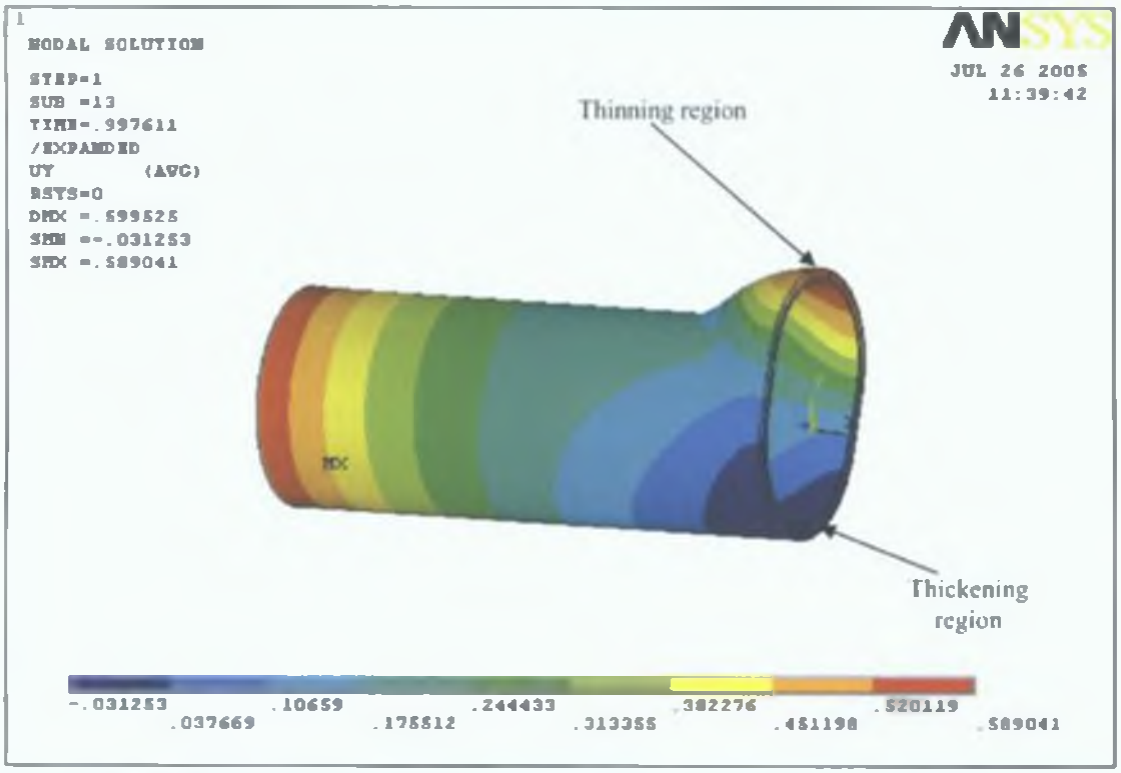

Figure 5.38.: Deform condition of the simulated T branch by 10 mm axial feed and 150 MPa internal pressure

Table 5.1 Summary of Results for X branch Simulations

Simulation Number	Coefficient of friction for contact pair-one	Coefficient of friction for contact pair-two	Axial Feed (mm)	Internal Pressure (MPa)	Max. Branch Height (mm)	Max. Von Mises Stress (MPa)
1	0.15	0.557	10	50	2.68	500
2	0.15	0.557	10	60	2.62	522
3	0.15	0.557	10	70	3.11	500
4	0.15	0.557	10	80	3.69	525
5	0.15	0.557	10	100	3.92	502
6	0.15	0.557	10	150	3.49	484
7	0.15	0.557	20	150	4.80	546

Table 5.2 Summary of Results for T branch Simulations

Simulation Number	Coefficient of friction for contact pair-one	Coefficient of friction for contact pair-two	Axial Feed (mm)	Internal Pressure (MPa)	Max. Branch Height (mm)	Max. Von Mises Stress (MPa)
1	0.15	0.557	10	50	2.06	529
2	0.15	0.557	10	60	2.90	476
3	0.15	0.557	10	70	3.70	437
4	0.15	0.557	10	80	3.84	506
5	0.15	0.557	10	100	4.74	442
6	0.15	0.557	10	150	5.89	506

5.4 Summary of the chapter

A number of simulations have been carried out in this chapter for both X branch and T branch model. For both models, the material properties and the dimension were kept constant. All the simulations have been run for different loading condition in order to observe the change of the stress, deformation, etc. A comparison between the simulated results of X and T branch have been made. Table 5.1 presents the results for the simulations carried out for X branch model by applying different loading condition. Table 5.2 depicts the results summary for the solution carried out by different loading condition for T branch model. These simulations have been carried out to observe the bursting pressure of the tube. A wrinkling failure due to the high axial feed has been defined for X branch model.

It can be concluded from the simulation results of this chapter that the optimum load path is 20 mm axial feed and 150 MPa internal pressure to from the X branch. In this case very low stress was distributed over the form component and the maximum bulge height was achieved. This chapter also depicts that the axial feed was kept almost constant for all simulations for both X and T branches. The results describes in table 5.1 that bulge height increase with increase the internal pressure while the equivalent von mises stress developed below the ultimate stress of the materials. The same results have been found in case of T branch simulation as well. Simulation has also been carried out in order to ascertain the bursting pressure of the tube material. A wrinkle occurrence has also been presented by applying a greater amount of axial displacement in compare to the internal pressure.

CHAPTER SIX

Conclusion and Recommendations

6.1 Conclusion

The following conclusions can be drawn from this research:

1. The feasibility of forming multi layered tubular components by the hydroforming process has been demonstrated experimentally as well as by finite element simulation.

2. Finite Element simulation results provided good prediction for the deformation of the multilayered tube in particular products, such as X and T branches.

3. The experimental and analytical results were in quite good agreement in term of deformation pattern under different loading conditions.

4. For certain combinations wrinkling will develop or bursting will occur. However, components can be formed successfully for a range of pressure and axial load combination.

5. The loading patterns were defined for the simulations of this research work were similar patterns used in ref. [45]. Simulations have been done for X and T- branches and experimental verification was carried out only for X-branch bi-layered tube. In the simulation results maximum developed von mises stress and the branch height for different loading conditions have been presented

6.2 Recommendations

From the knowledge acquired through this research work presented in the previous sections, the following may be suggested:

1. To build models for different materials and thickness and carry out experimental work.

2. Optimisation of the load path for multi-layered tube hydroforming is one of the important factors in order to form a successful component. This should be investigated further in a systematic way.

3. In the analysis, it was assumed that the die is rigid in nature; it was observed that there is some elastic deformation of the die during the process, which affects the forming process. Thus the die should be simulated and the stress development and elastic deformation analysed.

4. It has been observed in the simulation that the maximum von Mises stress developed in the simulated tube is beyond the prescribed ultimate stress of the material at the end of the solution. The exact computational stage at which the ultimate stress is reached was determined by manual intervention. A program should be written to stop the solution as soon as the von Mises stress reaches the ultimate stress of the material

CHAPTER SEVEN

References

[1] J.E. Grey, A.P.Deveraux and W.M. Parker, Apparatus for making wrought metal T's, U.S.A. Patents office, patent no 2, 203,868, June 1939

[2] Muammer Koc and Taylan Altan. Application of two dimensional (2D) FEA for the tube hydroforming process. International Journal of Machine Tools & Manufacture, 42,1285-1295, 2002.

[3] B.J. Mac Donald and Professor M.S.J. Hashmi. Three-dimensional finite element simulation of bulge forming using a solid bulging medium. Finite Elements in Analysis and Design, 37, 107-116, 2001.

[4] M. Ahmed and M.S.J.Hashmi. Three-dimensional finite-element simulation of bulge forming. Journal of Materials Processing Technology, Volume 119, Issues 1-3, Pages 387-392, December 2001.

[5] Y.M. Hwang and T. Altan. Finite element analysis of tube hydrofroming processes in a rectangular die, Finite Element in Analysis and Design, Vol. 39, Issue 11, , 1071-1082, August 2003.

[6] S.H. Zhang, Y.S. Zeng, and Z.R. Wang. Theoretical analysis and experimental research into the integral hydro-bulge forming of oblate shell. Journal of Material processing Technology, 62, 199-205, 1996.

[7] S.H. Zhng, K.B. Nielsen, J.Danckert, Z.R. Wang. Numerical Simulation of the integral hydro-bulge forming of non-clearance double-layer spherical vessel: deformation analysis. Computers and structures 70, 243-256, 1999.

[8] F.U. Enikeev and A. A. Kruglov, an analysis of the super plastic forming of a thin circular diaphragm. Int. J. Mech. Sci. Vol. 37, No 5,473-483, 1995

[9] S.H. Zhang, L. Jiang, B.L. Wang, & Z.R. Wang, established finite-element analysis of the integral hydro-bulge forming of double-layer gap spherical vessels. Int. J. Pres. Ves. & Piping 68, 161-167, 1996.

[10] M. Ahmed, M.S.J. Hashmi, Finite-element analysis of bulge forming applying pressure and in-plane compressive load, Journal of Material processing technology 77, 95-102, 1998.

[11] O.Kreis, P.Hein; Manufacturing system for the integrated hydroforming, trimming and welding of sheet metals pairs; Journal of Material Processing Technology; 115, 49-54, 2001.

[12] J.H. Lee, Y.J.Song, D.H. Shin, C.S Lee, microstructural evolution during superplastic bulge forming of Ti-6Al-4V alloy; Materials Science and Engineering, Vol.A243, Iss.1-2, pp.118-24, 15 March 1998.

[13] B.H. Lee, Y.T. Keum, R.H. Wagoner, Modeling of the friction caused by lubrication and surface roughness in sheet metal forming. Journal of Materials Processing Technology 130–131, 60–63, 2002.

[14] Jeong Kima, Yong-Wook Kima, Beom-Soo Kanga, Sang-Moon Hwangb, finite element analysis for bursting failure prediction in bulge forming of a seamed tube. Finite Elements in Analysis and Design 40, 953–966, 2004.

[15] Mac Donald, B.J.; Hashmi, M.S.J, Analysis of die behaviour during bulge forming operations using the finite element method, finite elements in Analysis and Design. Vol. no, Iss. 2, 137-51; Dec. 2002.

[16] Li Chunfeng; Zhao Zhiheng; Li Jianhui; Wang Yongzhi; Yang Yuying, Numerical simulation of the magnetic pressure in tube electromagnetic bulging, Journal of Materials Processing Technology. Vol. 123, Iss. 2, 225-8; 30 April 2002.

[17] El-Morsy, A.; Akkus, N.; Manabe, K.I.; Nishimura, Superplastic characteristics of Ti-alloy and Al-alloy sheets by multi-dome forming test, Materials Transactions. Vol. 42, Iss. 11, pp. 2332-8; Nov. 2001.

[18] Khraisheh, M.K.; Zbib, H.M, Optimum forming loading paths for Pb-Sn super plastic sheet materials, Transactions of the ASME. Journal of Engineering Materials and Technology. Vol. 121, Iss. 3, pp. 341-5; July 1999.

[19] Ninomiya, T.; Hira, H.; Kanetake, N.; Choh, T, High strain rate super plastic bulge forming of SiC particle reinforced 2124 aluminum alloy composite (Journal Paper).. Journal of Japan Institute of Light Metals. Vol. 48, Iss. 8, pp. 380-4; Aug. 1998.

[20] Xu Zuo, Yuanping Wei, Jun Chen, Lingshou Zeng, Xueyu Ruan; 3D FEM simulation of multi-stage forging process using solid modeling of forging tools; Journal of Materials Processing Technology 91, 191–195, 1999.

[21] F.H. Lin, A.A. Tseng; a finite element analysis of elasto-plastic contact problems in metal forming; Journal of Materials and Design; 19, 99-108, 1998.

[22] M. Hutchinson, R. Crampton, W. Ruston and M.S.J. Hashmi; The Hydraulic bulge forming of tubular components, The effect of altering the plungers applying compressive axial load, Proc. 6th Irish manufacturing committee conference, Dublin, 248-254, 1989.

[23] M.S.J. Hashmi, Radial thickness distribution around a hydraulically bulge formed annealed copper T-joint: experimental and theoretical predictions, 22nd Int. M.T.D.R Conference, 507-516, 1981.

[24] M.S.J. Hashmi, Forming of tubular components from straight tubing using combined axial load and internal pressure; theory and experiment, Proc. of Int. conf. on Dev. On drawing of metals Society, 146-155, 1983.

[25] F. Dohmann and F.Klass, Liquid Bulge Forming of Tubular Workpieces, Strips Sheets Tubes, Vol.4, Part1, 7-10, 1987.

[26] M. Imaninejad, G. Subhash, A. Loukus. Loading path optimization of tube hydroforming process. International Journal of Machine Tools & Manufacture 45, 1504–1514, 2005.

[27] D.M. Woo, Tube bulging under internal pressure and axial force, Journal of Engineering Materials and Technology, 421-425, 1978.

[28] S. Kandil, Hydrostatic metal tube bulging as a basic process, Metallurgy and Metal Forming, 152-155, 1976.

[29] F. Dohmann and C. Hartl, Liquid Bulge Forming as a Flexible Production Method, Journal of Materials and Processing Technology, vol. 45, 377-382, 1994.

[30] F. Dohmann and C. Hartl, Hydroforming – A Method of Manufacturing light weight Parts, Journal of Materials and processing Technology, Vol. 60, 669-676, 1996.

[31] L.A. M. Filho, J. Menzes and H. A. Al-Quereshi, Analysis of unconventional Tee forming on Metal Tubes, Journal of Materials and processing Technology, Vol. 45, 383-388, 1994.

[32] J. Tirosh, A. Neuberger and A. Shirizly, On Tube expansion by internal fluid pressure with additional compressive stress, Int. J. Mech. Sci., vol. 38, No. 8, 839-851, 1996.

[33] P. B. Mellor, Tensile instability in thin walled tubes, J. Mech. Eng. Sci., Vol. 4, No. 3, 251-256, 1962.

[34] B.H. Jones and P.B. Mellor, Plastic flow and instability behaviour of thin walled cylinders subjected to constant ratio tensile stress, J. Strain Analysis, Vol. 2, 62-72, 1967.

[35] R.P. Felgar, Plastic analysis of the instability of pressure vessels subjected to internal pressure and axial load, Trans. ASME, J. Basic Eng., Vol. 84, 62-72, 1962.

[36] N.A. Weil, Tensile instability of thin walled cylinders of finite length, Int. J.Mech. Sci., Vol. 5, 487-506, 1963.

[37] Sungatae Kim, Yonnhuk Kim, Analytical study for tube hydroforming, Journal of Material Processing Technology, 128, 232-239, 2002.

[38] Nader Asnafi, analytical modelling of tube hydroforming, Thin walled structures, 34, 395-330, 1999.

[39] Ken-ichi Manabe, Masaaki Amino, Effects of process parameters and material properties on deformation process in tube hydroforming , Journal of Material Processing Technology , 123, 285-291, 2002.

[40] W. Rimkus, H. Bauer, M.J. A Mihsein, Design of load curve for hydroforming applications. , Journal of Material Processing Technology, 108, 97-105, 2000.

[41] P. Ray, B.J. Mac Donald, Determination of the Optimal load path for tube hydroforming process using a fuzzy load control algorithm and finite element analysis. Finite Element in Analysis and Design, 41, 173-792, 2004.

[42] P.R. Adby and M.A.H. Dempster, Introduction to Optimization Method. Chapman and Hall, 1996

[43] P. Ray, B.J. Mac Donald, Determination of the load path for the tube hydro forming process using a fuzzy load control algorithm and finite element analysis. Finite Element in Analysis and Design 41, 173-192, 2004.

[44] M. Ahmed, Finite Element Modelling and Simulation of Metal Flow in Bulge Forming, Ph. D. thesis, School of Mechanical and Manufacturing Engineering, Dublin City University, Ireland, 1999.

[45] B.J Mac Donald, Non-linear finite element simulation of a complex bulge forming process, Ph. D. Thesis, School of Mechanical and Manufacturing Engineering, Dublin City University, Ireland, 2000.

[46] G.E. Dieter, Mechanical Metallurgy, Third edition, McGraw-Hill Publishing Company, 1996

[47] Materials Science and Metallurgy, Fourth Edition, Authors- Herman W.Pollack. A Reston Book, Prentice Hall, Englewood Cliffs, New Jersey 07632, 1994.

[48] ANSYS, Inc Theory References (8.1), Modelling and Solution

[49] MatWeb, materials properties data web site. 30-07-2005, at 14:30.

[50] www.superpipe.com, multi layered tube manufacturing company website, 21-07-2004, at 10.30 am.